Cold atoms in light fields:

From free-space optical lattices to multi-mode optical cavities

Arne Wickenbrock

A thesis submitted to the University of London
in partial fulfilment of the requirements for the
degree of Doctor of Philosophy

Department of Physics and Astronomy
University College London
March 2012

Arne Wickenbrock

30.03.2012

I, Arne Wickenbrock, confirm that the work presented in this thesis is my own. Where information has been derived from other sources, I confirm that this has been indicated in the thesis.

Signed ..... Date .....

Abstract

The electromagnetic mode density of the vacuum can be dramatically modified by the presence of an optical resonator. In the strong coupling regime, spontaneous emission in a cavity becomes a reversible process and the intracavity photon number undergoes Rabi oscillations. We load up to 200×10^3 ^{133}Cs atoms into a nearly confocal lossy cavity and reach the collective strong coupling regime. Normal mode splitting, the hallmark of this regime, is observed and cooperativities up to $C_{coll} = (186 \pm 5)$ are measured. In a second experiment we investigate for the first time the multi-mode character of the coupled cavity-atom system. In a confocal cavity the higher-order transverse cavity modes are degenerate in frequency and accessible to the spontaneous emission of the atomic ensemble. We observe an increase of the coupling constant measured via modal decomposed transmission analysis, which could be attributed to the presence of the higher-order modes. Normal mode splitting proportional to the square root of the atom number was visible for all of the different mode components. Furthermore, we observe a redistribution of the relative weights in the modal transmission composition, which scales with the atom number in the cavity mode.

In a second set of experiments, ^{87}Rb atoms were loaded into a dissipative lin $\perp$ lin lattice. By driving the lattice with a biharmonic force, transport can be observed when the systems symmetries are broken: the so called ratchet effect. Research in this area is concerned with the appearance of current reversals. We were able to identify dissipation related symmetry breaking as the underlying cause of an observed current reversal, which occurs as a function of the driving frequency. Furthermore, in a second experiment, we use the ratchet effect as a probe of the optical potential depths. We show that an oscillating force with a frequency far above any other system-inherent timescale, can be used to renormalize the optical potential. The ^{87}Rb atoms experience an average position-dependent force, which becomes controllable over the amplitude of the applied driving.

To my parents

Acknowledgements

I would like to thank my supervisor Prof. Ferruccio Renzoni for his support, his optimism and the opportunity to work on two experiments simultaneously. Thanks to Phil Jones for being my second supervisor and to Gordon Robb, David Cubero and Michal Hemmerling for theoretical support. I also thank my present and past colleagues and our visitors for being great people and nice to work with: Boeing, Cosimo, Martin, Meliz, Nihal, Peter, Philip, Ralf and Lyubo, who passed away far before his time.
Special thanks goes to Soliman for translating my script into reasonable English and all the other nice people I met during my stay at UCL.

I would not have been able to make it without the unconditional support of my parents; this thesis is dedicated to them. And I am deeply grateful to my girlfriend Laura for being the greatest person alive.

Contents

List of Figures

List of Tables

List of Abbreviations

AH	Anti-Helmholtz
AOM	Acousto-optic modulator
BEC	Bose Einstein condensate
BH	Bi-harmonic
c.c.	Complex conjugate
CCD	Charge-coupled device
CQED	Cavity quantum electrodynamic
CTE	Coefficient of thermal expansion
DF-DAVLL	Doppler-free dichroic atomic vapour laser lock
ECDL	Extended cavity diode laser
EGC	Error signal generating circuit
EOM	Electro-optic modulator
FM	Frequency modulation
FP	Fabry-Pérot cavity
FSR	Free spectral range
FWHM	Full width at half maximum
HF	High frequency
HWP	Half-wave plate

LVIS	Low-velocity intense source of atoms
MOT	Magneto-optical trap
NPBS	Non-polarizing beam splitter cube
Osc.	Oscilloscope
PBS	Polarizing beam splitter cube
PD	Photodiode
PDH	Pound-Drever-Hall stabilisation
QED	Quantum electrodynamic
QWP	Quarter-wave plate
TEM_{nm}	Transverse electromagnetic mode with indices n and m
UHV	Ultra-high vacuum

Chapter 1

Introduction

1.1 This thesis

This thesis is separated into two main parts. The first part describes experiments on the interaction of ^{133}Cs atoms and the light of an optical resonator. These experiments took most of my time and our initial motivation was to study a new cooling mechanism for particles called *cavity cooling*. To use the tailored vacuum mode density, or coloured vacua, in an optical resonator to extract kinetic energy from particles is an idea about 25 years old [56, 68]. Research on this cooling mechanism gained momentum in the late 1990s when the theory was developed [36, 107] and got extended in the early 2000s with several relevant publications (see [21] for a good review article). The idea is quite appealing: a polarizable particle acts as a position dependent refractive index in a standing wave resonator. It therefore changes the resonance condition depending on its position and, for a given set of parameters, the light intensity in the resonator. The light field in a resonator needs time to build up; when a moving atom goes through the potential minimum the light intensity reaches its maximum temporally delayed. This means that on average the polarizable particle sees a steeper potential hill when it goes up and a more shallow potential when it goes down. On average this leads to a decelaration, and the excess kinetic energy leaves the optical resonator as incoherent decay of the light field through the mirrors. What is exciting about this new laser cooling scheme is that it relies only on the dipole force, and therefore on the particle's polarizability,

and not on a favourable atomic energy structure. All particles, atoms and molecules, and even macroscopic objects became potential cooling candidates, while the final temperature and the cooling rate were externalized and accessible via the cavity and laser beam parameters. The same process could also be described in terms of the photon scattering rate [100, 101], which can be enhanced and suppressed by the presence of a cavity [43]. The first experimental results confirming the theoretical findings were achieved with a single atom in a high finesse cavity in Gerhard Rempes group in Munich in 2004 [60, 62] and even before then with a very similar setup to ours in 2003 [5, 14, 15]. Since the latter experiment implemented a large mode volume cavity with a relatively low finesse, capable of cooling several million particles at the same time, we considered it as a good starting point to investigate the collective cooling effects observed. But even though our experimental parameters were similar we couldn't reproduce the observed cooling. At this point we decided two things: firstly, to gain a deeper understanding of the dynamics we needed extensive numerical simulations of the system and, secondly, we needed to take a step back to investigate the collective cavity atom interaction in our experiment. The numerical simulations were conducted by Michal Hemmerling in the group of Professor Gordon Robb and are published in [39]. The experiments to quantify the atom-cavity interaction of our setup are presented in part 1 of this thesis.

Part 1 begins with an introduction to Cavity Quantum Electrodynamics, presents the apparatus and then the conducted experiments with ^{133}Cs atoms in a nearly confocal cavity. The part ends with an outlook on future experiments.

The second part presents experiments with ^{87}Rb atoms in dissipative optical lattices. While the numerical simulations by Michal Hemmerling lasted, the experimental effort on the ^{133}Cs experiment was reduced to a minimum; we were waiting for the theory to deliver us the right parameter regime to start again. This "free" time, an unused apparatus and our groups expertise in ratchet physics led to two successfully conducted experiments studying ^{87}Rb atoms in dissipative optical lattices and an upgraded ^{87}Rb machine for future work with ultra-cold atoms. Part 2 starts with an introduction to the broad area of ratchet physics, motivates and illustrates the upgrade of the experimental apparatus and

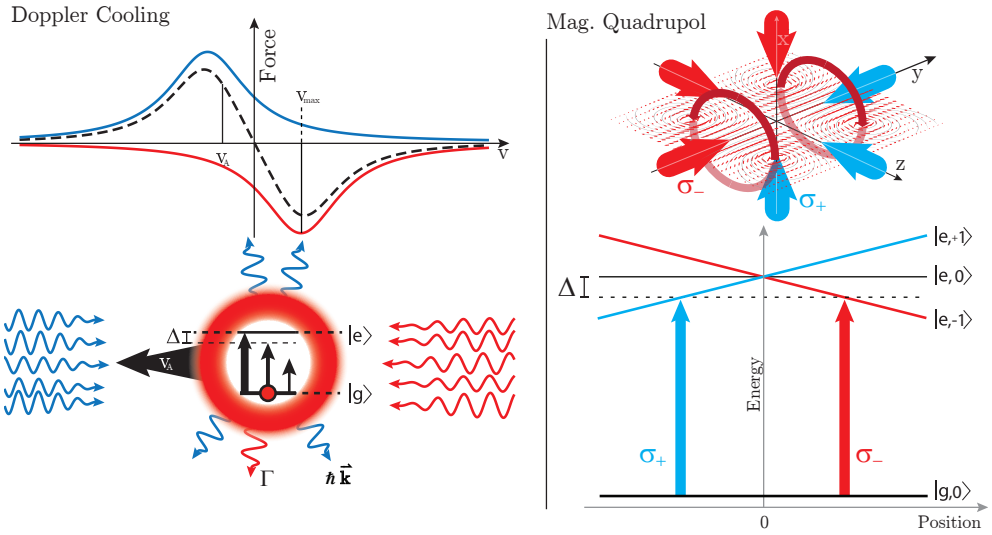

Figure 1.1: The two ingredients of a magneto-optical trap (MOT). **Left:** A velocity dependent force arises due to the different scattering rates of the Doppler-shifted counterpropagating beams.
Right: An additional magnetic quadrupole field provides a constant magnetic field gradient in all three dimensions with a zero in the centre and gives rise to a spatially dependent force. To address the correct excited state sublevel the counterpropagating beams have opposite circular polarizations.

describe the two experiments. The rest of this introduction is spent on a brief overview of the fundamentals of laser cooling and cavities.

1.2 Fundamentals

This section provides an introduction to the field of cold atoms. It will briefly describe the magneto-optical trap (MOT) as the starting point of all the experiments described in this thesis, then Sisyphus cooling as a strong sub-Doppler cooling mechanism at the heart of all the ^{87}Rb experiments in part 2, and finally the models and definitions for the treatment of an optical Fabry-Pérot cavity as the main ingredient of the experiments in part 1. There are plenty of well-written textbooks on these topics and this chapter relies on two of them [25, 65]. The historical remarks are based on [75].

1.2.1 Laser Cooling and Trapping

The Magneto-Optical Trap (MOT) has been the workhorse in modern atomic physics since 1987 [79] and the starting point for many experiments. Even though light pressure forces were already suggested by Maxwell [63] and experimentally studied by Lebedew in 1901 [53], their implementation for the cooling of atoms and its acknowledgment by the Nobel committee had to wait until 1997. The Nobel Prize was awarded for the experimental realization of the first cooling technique involving laser beams dubbed "optical molasses" by Steven Chu et al. in 1985 [16], the first breaking of the so-called Doppler limit by William D. Phillips [76], and the theoretical identification of the process by Claude Cohen-Tannoudji [18]. Today there are several hundred experiments using magneto-optical traps with various atomic species as a starting point of their research. So what makes them so powerful?
The first and most intuitive cooling mechanism involving laser beams, suggested by T.W. Hänsch and A.L. Schawlow in 1975, is Doppler cooling [40]. Electro-magnetic radiation coupling atomic energy levels gets absorbed when it is on resonance with an atomic transition. The photon momentum is then transferred to the absorbing atom. Compared to an alkali atom, such as ^{133}Cs, the photon momentum is tiny. One spontaneous emission event on the D2 line accelarates one atom by the recoil velocity $v_r = 3.5$mm/s [87]. In order to decelerate thermal atoms flying around with velocities of 300m/s, thousands of photon scattering events are necessary. The photon scattering rate of an atom is given by:

$$R_{scatt} = \frac{\Gamma}{2}\frac{s}{1+4\Delta^2+s}, \tag{1.1}$$

where Γ is the inverse of the excited state lifetime, Δ is the detuning of the laser field with respect to the atomic transition in units of Γ, and s is the saturation parameter given by the light intensity in units of the saturation intensity:

$$\begin{aligned} s = \frac{I}{I_{sat}} &= 2\left(\frac{\Omega}{\Gamma}\right)^2, \\ \text{where } \Omega &= -\frac{\vec{d}\cdot\vec{E_0}}{\hbar} \end{aligned} \tag{1.2}$$

is the on-resonant Rabi frequency as a measure of the coupling strength of the transition with dipole operator $\vec{d}$ between the ground state $|g\rangle$ and the excited state $|e\rangle$ of a two-level atom and $\vec{E_0}$ the electric field amplitude.
The force on the atom is the momentum transferred per unit time and therefore $F = \hbar k R_{scatt}$. For the maximum scattering rate of $\Gamma/2$ the corresponding maximum acceleration for a ^{133}Cs atom is:

$$a_{max} = \frac{v_r \Gamma}{2} \approx 58 \times 10^3 \frac{m}{s^2} \approx 6000g. \tag{1.3}$$

For the much lighter sodium atom the maximum acceleration reaches even up to 10^5 times the gravitational acceleration g. So even though the photon momentum is small, light forces acting on atoms can be huge due to the very high scattering rate. But this is also the reason why effective Doppler cooling is restricted to atoms with a simple level structure like the hydrogen-like alkali atoms. The small momentum transfer makes it necessary to cycle the same transition over and over again; if the excited state can decay into another level that is not coupled via the laser beam, the cooling ceases. All alkali atoms have two hyperfine split ground states and need a repumper laser to recycle lost atoms. Figure 1.1 depicts the working principle of Doppler cooling on the left and the idea behind the magneto-optical trap on the right. To implement the radiation pressure force to reduce the atomic velocity on average, Doppler cooling makes use of the Doppler effect: the frequency of the light depends on the reference frame; an atom moving towards a laser beam "sees" a higher frequency and an atom moving away from it a lower frequency than an atom at rest. A 2-level atom (red) moving with a velocity v towards a laser beam which is red detuned by $\Delta = \omega_p - \omega_A$ to the atomic transition in the laboratory reference frame experiences the beam Doppler-shifted by $\delta = \vec{k} \cdot \vec{v}$ (first order) to the blue and therefore closer to resonance: its scattering rate increases. The same beam coming from the other side will be scattered less since the Doppler shift has an opposite sign and the transition is further away from resonance. The net force on the atom equals the difference between the two scattering rates times the photon momentum $\hbar k$. It is velocity dependent but spatially isotropic. It can cool atoms very quickly to a very low temperature but it doesn't trap.

A configuration of three perpendicular pairs of counterpropagating laser beams red detuned to the atomic transition is called "optical molasses" since the atoms will experience a velocity-dependent force in all three dimensions. Atoms in an "optical molasses" will move due to random kicks of the spontaneously emitted photons with average velocity zero but with variance $\langle v^2 \rangle$ which can be expressed as a minimum Doppler cooling temperature $k_B T_D = \hbar\Gamma/2 = m \langle v^2 \rangle$, where k_B is the Boltzmann constant and m is the atomic mass. The Doppler limit for ^{133}Cs and ^{87}Rb is 125.61 μK and 145.57 μK respectively [87, 88]. To trap the atoms with radiation pressure the scattering rate needs to be spatially dependent. This can be done easily by implementing a quadrupole magnetic field. In order for the MOT to work the excited state needs to have an overall angular momentum of at least $F = 1$. In this case the magnetic field lifts the degeneracy of the Zeeman sublevels shown in figure 1.1 on the right, and the detuning depends linearly on the magnetic field which also varies linearly in space. To address the correct excited sublevel, counterpropagating circularly polarized laser beams are used depending on the configuration of the magnetic field. An atom moving away from the magnetic zero experiences an increasing radiation pressure from one of the beams and a decreasing radiation pressure from the other beams resulting in a net force towards the centre of the MOT. This way up to 10^{10} atoms can be trapped with densities of around 5×10^{10} atoms per cm^3; an ideal starting point for experiments with cold atoms.

1.2.2 Sub-Doppler Cooling

Since the first implementation of an optical molasses researchers were confronted with sub-Doppler temperatures. Also, the scaling of the final temperatures as a function of laser beam detuning and power were conflicting with the established 2-level Doppler cooling theory. The experimentally observed sensitivity on the background magnetic field suggested a connection to the magnetic sublevels. The theoretical interpretation by Jean Dalibard and Claude Cohen-Tannoudji was published in 1989 [18]. One of the mechanisms was termed *Sisyphus cooling*, since a moving atom is endlessly climbing potential hills and this is the mechanism relevant in part 2. It makes use of a second effect of a light field on an atom:

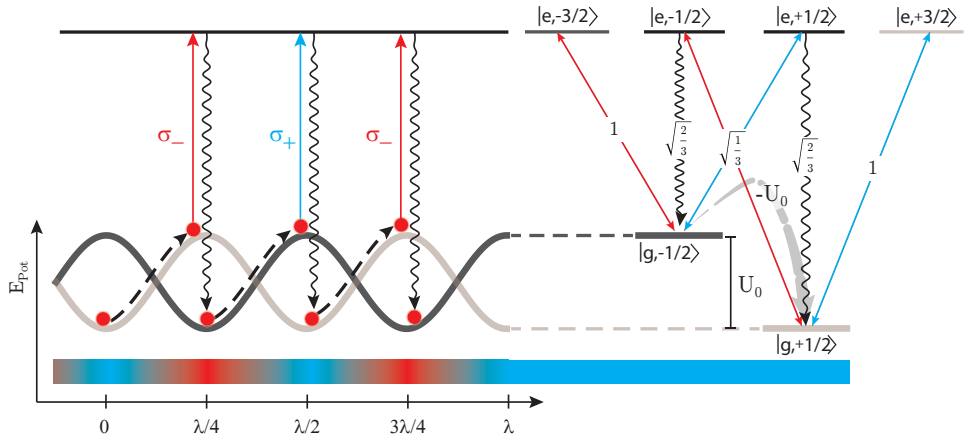

Figure 1.2: Sisyphus cooling in the lin ⊥ lin configuration as explained in the text.
Left: The resulting interference pattern can be described by a σ_- (red) and a σ_+ (blue) standing wave shifted by $\lambda/4$ with periodicity $\lambda/2$. The two ground states of a $J_g = 1/2 \rightarrow J_e = 3/2$ transition experience different light shifts accordingly.
Right: On the top of the potential hill, the circular polarization (σ_-) responsible for light shift of ground state $|g, -1/2\rangle$ vanishes. Instead σ_+ is at maximum intensity. But this couples $|g, -1/2\rangle$ to $|e, +1/2\rangle$, a state which is more likely to decay into $|g, +1/2\rangle$ due to a bigger Clebsch-Gordon coefficient.

oscillating electric fields deform the electronic shell of the atom, inducing an oscillating dipole moment. This induced dipole moment interacts with the driving field, which leads to a conservative force proportional to the gradient of the electro-magnetic field intensity: the so-called Dipole force. When the frequency of the field is above resonance, the induced dipole oscillates maximally out of phase and is pushed towards the intensity minima. Below resonance, the induced dipole oscillates in phase and is being pulled towards intensity maxima. The light field *dresses* the atomic energy states; the new diagonal states of the atom+photon system are shifted in energy depending on the strength of the radiation field. The *light shift* is proportional to the coupling strength, or the Rabi-frequency Ω, introduced by the light field. A laser beam therefore produces a spatially varying optical potential for the atomic energy states. For a red detuned laser, the optical intensity maximum is the potential energy well of the dipole force. *Sisyphus cooling* also needs a slightly more complex atomic level structure as shown in figure 1.2 on the right. The simplest transition to observe this sort of cooling is a

$J_g = 1/2 \rightarrow J_e = 3/2$ transition, where there are two different ground states and four excited states, differing by their magnetic quantum number. The coupling between the levels is given by polarization selection rules and the strength of the Clebsch-Gordon coefficients. An optical lattice resulting from the interference of two counterpropagating laser beams with orthogonal linear polarization can be decomposed into two superimposed optical standing waves with different circular polarizations (σ_+ and σ_-) shifted by $\lambda/2$. Since the light shift depends on the coupling strength, the optical potential for each ground state varies in space like the respective circular polarization optical lattice. This is sketched in figure 1.2 on the left. The potential $U_\pm(z)$ at position z for each ground state $|g, \pm 1/2\rangle$ follows:

$$U_\pm(z) = \frac{U_0}{2}[-2 \pm \cos(2kz)], \tag{1.4}$$

where the maximum potential depth is given by $U_0 \approx \hbar\Omega^2/(4\Delta)$ with Δ the detuning between atomic transition and laser beam and Ω the Rabi frequency as defined in equation (1.2). An atom moving in such a potential transfers continuously kinetic energy into potential energy when moving uphill and vice versa when moving down hill. For *Sisyphus cooling* to occur a second ingredient is needed: optical pumping. The laser beams have to be so close to resonance that there are still sufficient scattering events taking place. With the slightly more complex level structure of the $J_g = 1/2 \rightarrow J_e = 3/2$ transition, if a photon gets absorbed and transfers the atom into the excited state, the possiblity to decay into either of the ground states is given by the Clebsch-Gordon coefficients [87]. If a $|g, -1/2\rangle$ atom moves through the potential and reaches the top of the hill, the only light present is σ_+ polarized and the only transition possible is to the excited state $|e, +1/2\rangle$. If the atom gets transferred to this state it is more likely to relax back into the other ground state $|g, +1/2\rangle$, which is lower in potential energy by U_0. The atom gets *optically pumped* into the other ground state and the excess potential energy is taken away by the spontaneously emitted photon. This process continues until the atom's kinetic energy is not big enough to reach the top of a potential. The atom is trapped in the optical lattice. For this simplest level structure where *Sisyphus cooling* takes place, once the atom is

localized in the optical potential, the cooling stops and the atoms keeps oscillating in a single lattice site. Additional optical pumping events let the atom follow a diffusive random walk through the optical lattice, with a finite temperature of the order of the initial potential depth U_0.
But ^{87}Rb atoms have an even richer substructure; instead of just two ground states there are 5. The transition for the transport studies in part 2 is the $F_g = 2 \rightarrow F_e = 3$. In this case each ground state has its own optical potential and cooling continues even within one lattice site.

1.2.3 Fabry-Pérot cavities

A Fabry-Pérot cavity (see figure 1.3) is an optical resonator made of two mirrors separated by the distance L. Originally the term was used for the special case with two plane mirrors, but is today used for any linear cavity configuration. If a laser beam is incident onto a mirror, it gets partly reflected, partly transmitted and partly absorbed, according to the amplitude absorption, reflection and transmission coefficients of that surface. In a Fabry-Pérot cavity a part of the incident beam is transmitted through the first mirror and oscillates then between the two reflecting surfaces. After one roundtrip it interferes with itself and, in the case of constructive interference, a field builds up in the cavity which can exceed the incident intensity dramatically.
Here I am going to introduce some cavity formulae which I am going to use later on to characterize the cavities in this thesis.

Derivation of the finesse Figure 1.3 shows a schematic of a Fabry-Pérot cavity. It is made out of two surfaces separated by the distance L corresponding to a phase change δ for a roundtrip. For simplicity both surfaces have the same amplitude reflection and transmission coefficients r, t respectively, and no losses. In a steady-state, the circulating field in the cavity E_{circ}, is given by the interference of the incident light amplitude transmitted through the left mirror tE_{in} with the already circulating electric field after reflection from the right surface and from the left surface. Whether the interference is constructive or destructive depends on the acquired phase difference δ due to the optical path-length

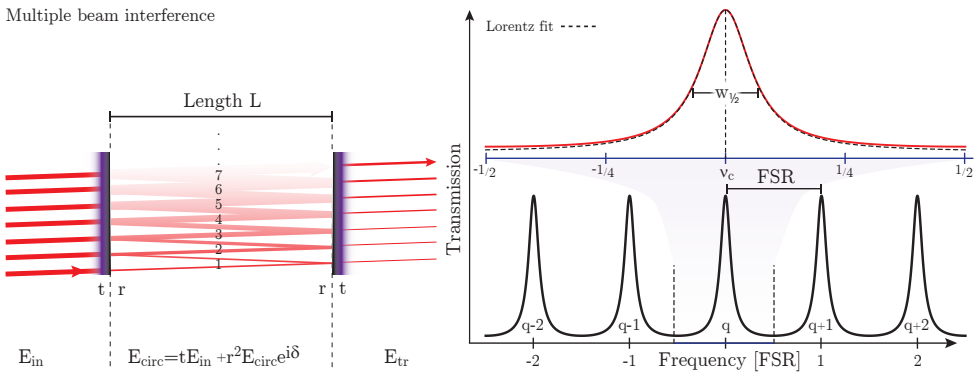

Figure 1.3: Fabry-Pérot schematic.
Left: Two plane parallel surfaces with amplitude reflection and transmission coefficients r and t experience the build up of constructive multiple beam interference when the phase δ acquired during one roundtrip of $2L$ equals 2π.
Right: The transmission spectrum shows characteristic spikes whenever an incoming laser is on resonance. The frequency difference between adjacent longitudinal modes is called the Free Spectral Range (FSR) and is related to the linewidth $w = \kappa/\pi$ via the Finesse like $F = \mathrm{FSR}/w$.

of one roundtrip. The field in the cavity is given by:

$$\begin{aligned} E_{circ} &= tE_{in} + r^2 E_{circ} e^{i\delta} \\ \Rightarrow E_{circ} &= \frac{E_{in} t}{1 - r^2 e^{i\delta}}. \end{aligned} \tag{1.5}$$

A commonly measured quantity is the transmitted intensity I_{tr}, which is then given by the circulating intensity I_{circ} multiplied by the amplitude transmission coefficient squared:

$$I_{tr} = t^2 E^*_{circ} E_{circ} = \frac{I_{in}}{1 + \frac{4r^2}{(1-r^2)^2} \sin^2(\delta/2)}. \tag{1.6}$$

When the accumulated phase δ during one roundtrip of length $2L$ is a multiple of 2π, the sine term becomes zero and the transmission is at a maximum. The time it takes for a roundtrip is $2L/c$; for the phase difference to be $n \cdot 2\pi$ the frequency needs to be a multiple of the inverse of this time, which is called the *Free Spectral Range* (FSR):

$$\mathrm{FSR} = \frac{c}{2L}. \tag{1.7}$$

This is the first important quantity to characterize a Fabry-Pérot cavity. The second is the characteristic width of the resonance peaks. For small values of the phase δ, the sine term in equation (2.11) can be replaced by its argument. The transmission around resonance then follows a Lorentzian curve, which, when expressed with the phase replaced by a frequency difference to resonance $(\nu - \nu_c)$, can be written like:

$$I_{tr}/I_{in} = \frac{1}{1 + \frac{4r^2}{(1-r^2)^2}\left(\pi\frac{\nu-\nu_c}{\mathrm{FSR}}\right)^2} = \frac{1}{1 + \left(\frac{2(\nu-\nu_c)}{w_{1/2}}\right)^2}, \tag{1.8}$$

with the Lorentzian *full width half maximum* in frequency:

$$w_{1/2} = \kappa/\pi = \mathrm{FSR}\frac{\sqrt{1-r^2}}{\pi r}. \tag{1.9}$$

The single mirror loss rate κ is more commonly used in cavity quantum electrodynamic (CQED) experiments. The ratio of free spectral range and linewidth is called the *Finesse*:

$$F = \frac{\mathrm{FSR}}{w_{1/2}} = \frac{\pi r}{\sqrt{1-r^2}}. \tag{1.10}$$

The finesse is a measure of the quality of the mirrors, since it is proportional to the ratio of amplitude reflection to transmission. High reflectivity means more interfering beams and therefore a narrower linewidth.

Stability diagram Not every configuration of mirrors is capable of forming a stable mode. Sometimes unstable resonators are even preferred. To get an idea how to make a statement of the stability of a cavity mode one has to recall some basics of geometrical optics which is very well done in [37] or [89]. In geometrical optics a beam of light is represented by a 2-dimensional vector. The first dimension is the axis offset, the distance of the beam with respect to the propagation axis and the second is the angle with respect to that axis. Optical elements, such as lenses or mirrors, free propagation, and surfaces can be represented as a matrix acting on the beam vector and several matrices can be multiplied to make more complex optical arrangements treatable.

The roundtrip of a light beam in a cavity can also be described by a matrix M:

$$M = \begin{pmatrix} A & B \\ C & D \end{pmatrix}.$$

A beam reflecting back and forth in a cavity is stable over time when all elements of matrix M' stay finite in the limit:

$$M' = \lim_{n\to\infty} \begin{pmatrix} A & B \\ C & D \end{pmatrix}^n. \tag{1.10}$$

It can be shown [89] that this is the case when:

$$\left|\frac{A+D}{2}\right| < 1. \tag{1.11}$$

For a linear cavity made of two mirrors with curvatures R_1 and R_2, separated by the optical path-length L, this means that the product of the mirror parameters $g_i = 1 - \frac{R_i}{L}$ is between 0 and 1 as shown in diagram 1.4:

$$0 < g_1 g_2 < 1. \tag{1.12}$$

So technically the confocal cavity is not a stable configuration since its g-factors equal zero. However, this is just valid for a single length of the given mirror curvatures and is therefore impossible to achieve. There will always be a deviation from confocality.

Gaussian Beams In a better approximation than representing a light beam by a ray with an angle and an axis offset, the wave equation derived from Maxwell's equations governing the behaviour of light is solved in the paraxial approximation [89]. The results are so-called *Gaussian beams*: they are a mixture of the trivial solution of a spherical wave and a plane wave. They combine a propagation direction with confinement in the transverse plane. From Maxwell's wave equation for the electro-magnetic field, the *Helmholtz equation* is derived by just considering a single frequency ω and separating a spatial envelope from the temporal dynamics. The envelope function of the electro-magnetic field $u(x, y, z)$

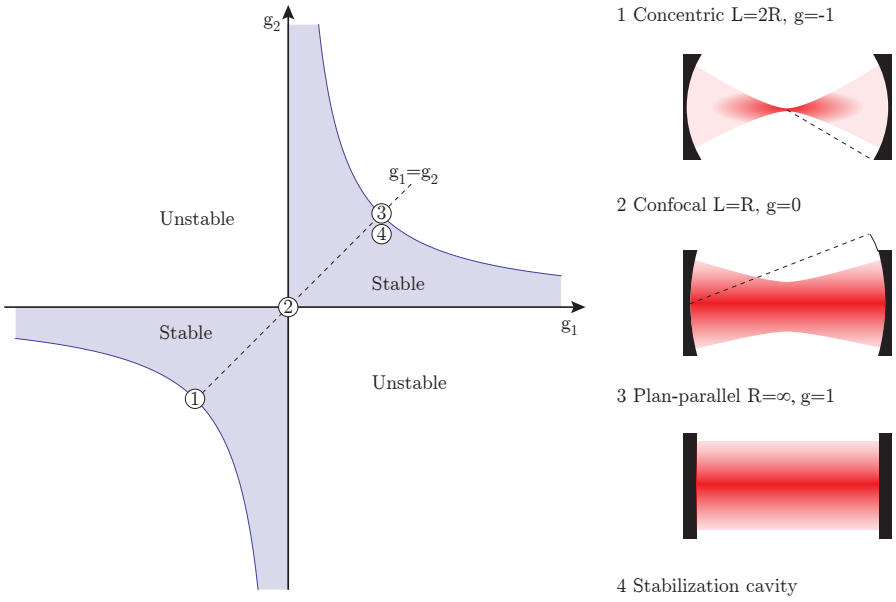

Figure 1.4: The stability diagram for a linear cavity. Resonators with g factors within the blue area on the left are stable. For guidance three limits of the stability diagram are shown in detail. First the concentric cavity (1), where the mirror separation equals twice the mirror curvature, then the confocal cavity (2) used in this thesis and (3) a cavity with two plane mirrors. For reference the stabilization cavity built and used in the laser setup of the part 1 experiments is shown as well (4).

solves the differential equation:

$$\nabla^2 u + k^2 u = 0. \tag{1.13}$$

Introducing a propagation direction z via the ansatz $u(x,y,z) = \psi(x,y,z) \cdot e^{-ikz}$ with $k = \frac{2\pi}{\lambda}$ and applying the *paraxial approximation*:

$$\left|\frac{\partial^2\psi}{\partial z^2}\right| \ll \left|2k\frac{\partial\psi}{\partial z}\right|, \left|\frac{\partial^2\psi}{\partial x^2}\right|, \left|\frac{\partial^2\Psi}{\partial y^2}\right|, \tag{1.14}$$

leaves the *paraxial wave equation* for the spatial envelope of the EM-field as:

$$\frac{\partial^2\psi}{\partial x^2} + \frac{\partial^2\psi}{\partial y^2} - i2k\frac{\partial\psi}{\partial z} = 0, \tag{1.15}$$

which is solved by the fundamental Gaussian beam mode function:

$$u(x,y,z) = \psi(x,y,z)\, e^{-ikz} = e^{-i\frac{k}{2q(z)}\left(x^2+y^2\right)} e^{-ip(z)}, \tag{1.16}$$

with the *complex beam parameter* q and z-dependent phase factor p. The beam parameter q can be written as:

$$q(z) = z + iz_R \text{ or } \frac{1}{q(z)} = \frac{1}{R(z)} + \frac{i\lambda}{\pi w^2(z)}, \tag{1.17}$$

with in the propagation direction varying beam waist $w(z)$ and beam front curvature $R(z)$. The *Rayleigh range* relates the expansion of the beam along z to the beam waist in the focus ($z = 0$) of the beam w_0 via $z_R = \pi w_0^2/\lambda$. A Gaussian beam is spatially completely determined by z_R. The beam waist $w(z)$ and phase front curvature radius $R(z)$ follow:

$$\begin{aligned} w(z) &= w_0\sqrt{1 + z^2/z_R^2}, \\ R(z) &= z\left[1 + z_R^2/z^2\right]. \end{aligned} \tag{1.18}$$

The complex phase factor $p(z)$ can be written like:

$$e^{-ip(z)} = \frac{1}{\sqrt{1 + z^2/z_R^2}} e^{i\tan^{-1}(z/z_R)}. \tag{1.19}$$

The prefactor is responsible for a diminishing amplitude of the electric field for increasing z, to compensate for the expansion of the beam-waist. The second effect is an additional phase factor called the *Gouy-phase*. For the fundamental solution in (1.16) the *Gouy-phase* varies from $-\pi/2$ for $z \to -\infty$ to $\pi/2$ for $z \to +\infty$ with a zero crossing at the beam waist position. It is essentially the phase difference between a plane travelling wave and a Gaussian beam, and can be attributed to the curved wavefronts of the beam.
The complete solution normalized to a maximum of 1, and with $r^2 = x^2 + y^2$ reads:

$$u(x, y, z) = \underbrace{\frac{1}{\sqrt{1 + z^2/z_R^2}}}_{\text{Amplitude}} \underbrace{e^{-\frac{r^2}{w^2(z)}}}_{\text{Profile}} \underbrace{e^{-i\frac{kr^2}{2R(z)}}}_{\text{Curvature}} \underbrace{e^{-i\left(kz - \tan^{-1}(z/z_R)\right)}}_{\text{Plane wave + } \textit{Gouy}}. \tag{1.20}$$

It turns out that the matrices used in geometric optics can still be used in this better approximation to the behaviour of radiation beams. A matrix M transforms the q-parameter of a Gaussian beam according to:

$$\begin{pmatrix} A & B \\ C & D \end{pmatrix} \cdot q \equiv \frac{Aq + B}{Cq + D}. \tag{1.21}$$

For a given mirror configuration, the fundamental resonator mode is defined by the two mirror surfaces; the radius of curvature of the mode has to match the mirror curvatures. This also means that the beam waist w_0 of the fundamental Gaussian mode is defined by the selection of mirrors and there distance. For a confocal resonator of length L, the waist for a beam with a wavenumber of $k = 2\pi/\lambda$ is given by:

$$w_0 = \sqrt{\frac{L}{k}}. \tag{1.22}$$

Higher order transverse Modes Of course there are more solutions to the paraxial Helmholtz equation than just the single mode function in equation (1.20). In fact, for a given basis there are infinite higher order solutions. Expressed in the rectangular *Hermite-Polynomial* basis with a later defined normalization factor c_0, the mode function of a higher order transverse mode TEM_{nm} reads:

$$\begin{aligned} u_{nm}(x, y, z) = & \frac{c_0 w_0}{w(z)} H_n\left(\frac{\sqrt{2}x}{w(z)}\right) H_m\left(\frac{\sqrt{2}y}{w(z)}\right) \\ & \times e^{-\frac{r^2}{w^2(z)}} e^{-i\frac{kr^2}{2R(z)}} \\ & \times e^{-i\left(kz - (n+m+1)\tan^{-1}(z/z_R)\right)}. \end{aligned} \tag{1.23}$$

The beam profile is modulated according to the Hermite-Gaussian function of order nm, zero crossings are introduced and the beam width increases. But also the *Gouy-phase* increases proportional to the mode indices. Figure 1.5 shows illustrations for two different higher order modes and the fundamental TEM_{00} mode. Since the phase of the laser beam incorporates a factor proportional to the higher order mode index, the resonance condition for a roundtrip differs for different higher order modes. The following expression gives the eigen frequency of the higher order transverse modes (q-th longitudinal, n,m-th transverse mode) in a

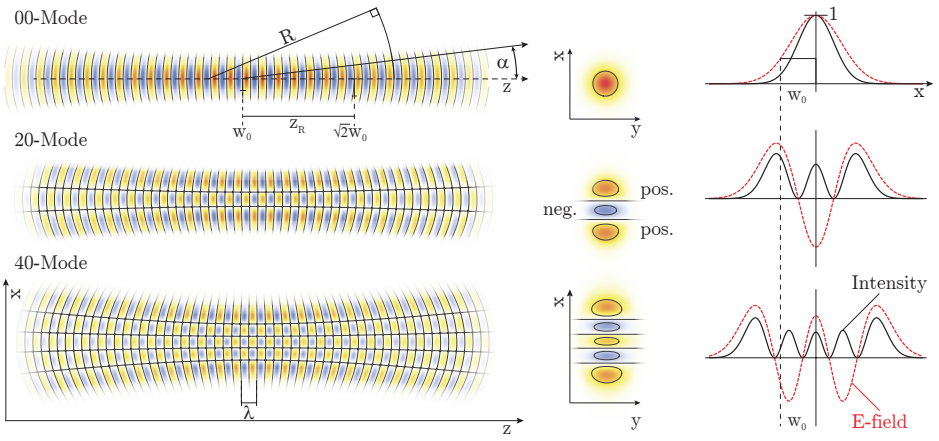

Figure 1.5: Gaussian beam illustration
Left: Cross-section through different transverse electromagnetic (TEM) modes along the propagation direction.
Middle: Transverse profile of the different TEM modes.
Right: Electric field strength and according intensities along the x-axis. Since the effective beam waist of the higher order TEM modes increases, the maximum electric field strength is reduced.

cavity, as a function of the geometrical parameter of the cavity g:

$$\nu_{qmn} = \frac{c}{2L}\left[q + \frac{1+l+m}{\pi}\arccos\left(g\right)\right]. \tag{1.24}$$

For the special cases of the concentric, the plane and the confocal resonator the frequency difference per transverse mode index is $(1, 0, 0.5)$ FSR respectively. The case we are interested in is the confocal one. When the length of the cavity L equals the curvature of the mirrors R, the cavity is confocal and the frequency difference for different higher order modes reduces to:

$$\nu_{qmn} = \frac{c}{2L}\left[q + \frac{1+l+m}{2}\right]. \tag{1.25}$$

As a result, the transmission spectrum of the cavity reduces to two peaks. The first peak at the frequency $\nu_{q00} = (q + 1/2)\,\mathrm{FSR}$ of the TEM_{q00}, and the second peak 1/2FSR further at $\nu_{q10} = (q + 1)\,\mathrm{FSR}$. Degenerate with the first peak with longitudinal mode q_0 are all modes with the same value of the mode indices sum $(2q + n + m) = 2q_0$. All modes with $(2q + n + m) = 2q_0 + 1$ are degenerate with the second peak of the spectrum and therefore with the first transverse mode with longitudinal mode

index q_0. For example the $(q-1, 2, 0)$ mode is at the same frequency as the $(q, 0, 0)$ mode. The two degenerate peaks are fundamentally different, while modes degenerate with the fundamental TEM_{q00} can have a central intensity component, all modes degenerate with the first transverse mode have an intensity node in the profile centre.

Part I

Cavity quantum electrodynamic in a lossy optical resonator

Cavity Quantum Electrodynamics (CQED) is an important field in modern atomic physics [66]. It started with Purcell's famous observation in 1946 [1] that the spontaneous emission rate can be dramatically modified by the presence of a cavity. He recognized the importance of the electro-magnetic mode density for the emission process and how to alter it with a resonator. Groundbreaking experimental work on the interaction of atoms and light in confined spaces started in the microwave regime with experiments on Rydberg-atoms. By removing available vacuum modes which could welcome the spontaneously emitted photon with a microwave cavity, spontaneous emission could be "turned off" [43]. Several other experiments observed this phenomenon with higher transition frequencies: in the infrared [45] and finally in the optical regime [38].
A theoretical model to treat the interaction of light and atoms within a resonator is the Jaynes-Cummings model [44]. It has been particularly powerful in proving fundamental physical phenomena, such as the collapse and revival of Rabi-oscillations due to interference of the different Rabi-frequencies associated to different photon numbers [11]. It is a single-atom, single-mode interaction picture (which can be easily extended to contain N atoms [92]). The mode and the atomic polarization are coupled via the exchange of a photon. A hallmark of these dynamics, as of any other coupled system, is the accompanying normal-mode splitting of the energy level structure. The inhibition and enhancement of spontaneous emission happens in the so called "bad cavity" limit, where the coupling of the particle to the resonator is weak in comparison to the environmental coupling parameters. If the influence of the resonator can be made dominant in the dynamics, the splitting of the excited state level structure becomes observable; an indication of the "good cavity" regime. The excitation undergoes Rabi-oscillations between atom(s) and the resonator mode.
Normal-mode splitting in the optical regime was first observed in 1989 [80] for several atoms and then in 1992 [93] for just a single atom. Nowadays there are several experiments investigating coupled atom-cavity systems for a broad range of applications and fundamental research. High-finesse cavities strongly coupled to single atoms [61, 106] and Bose-Einstein Condensates [9, 49] have been realized. The optical resonators in most experiments can effectively be modelled by a single-mode interac-

tion constant, since the higher order-transverse modes available in most cavities have different frequencies. In our case, the implemented close to confocal cavity was used to investigate the collective coupling of atoms to a multi-mode cavity field, with potential benefits to the coupling strength [85], as the prerequisite for a *cavity cooling* experiment [55] and possible applications in quantum computing.

This part is organized as follows: firstly, the Jaynes-Cummings model is presented since it is necessary for the understanding of the experiments. Then the experimental apparatus is described and characterized, and the science cavity's linewidth, free spectral range and its deviation from confocality are determined. With the working machine we conducted two experiments. First, it is shown that the cavity-atom system is in the collective strong coupling regime, we show the $\sqrt{N}$ dependence of the later derived coupling constant g, which we measured via the extent of the observed normal mode splitting. In the following chapter, we look in detail into the mode decomposition of the transmitted light field. Since the cavity is close to confocal, the single-mode approach of the Jaynes-Cummings model has to be extended. Via normal mode splitting measurements we show that the ^{133}Cs atoms in the apparatus are simultaneously strongly coupled to multiple transverse modes of the optical resonator. This is a situation which could be interesting for quantum computing and the build up of multi-mode entanglement, since different transverse modes interact with each other coherently via the atomic sample. And different transverse modes can be addressed with spatially separated laser beams.

Chapter 2

Jaynes-Cummings model

The Jaynes-Cummings Hamiltonian [44, 86] describes the interaction of a single two-level atom represented by Pauli spin matrices $\vec{\sigma}$ with the electro-magnetic field of a single mode resonator with coupling constant g. The Hamiltonian without zero point energy of the EM-field and after rotating wave approximation reads:

$$\begin{aligned} H &= H_{atom} + H_{mode} + H_{int}, \\ &= \hbar\omega_A \sigma^z + \hbar\omega_C a^+ a + i\hbar \left(g\sigma^+ a + g^* \sigma^- a^+ \right), \end{aligned} \tag{2.1}$$

with the atomic transition frequency ω_A and cavity resonance frequency ω_C. The coupling constant g defined by:

$$g = \frac{\mu E_1}{\hbar}, \tag{2.2}$$

is proportional to the *dipole matrix element* of the atomic transition:

$$\mu = \langle g \left| \hat{\mu} \right| e \rangle, \tag{2.3}$$

and to the *electric field per photon*:

$$E_1 = \sqrt{\frac{\hbar\omega_C}{2\epsilon_0 V}}. \tag{2.4}$$

The bigger the cavity volume V, defined by the integral

$$V = \int_{-\infty}^{\infty} \int_{-\infty}^{\infty} \int_{-L/2}^{L/2} \left| u_{00}(x, y, z) \right|^2 dxdydz, \tag{2.5}$$

the smaller the effect of a single photon onto the atom. u_{00} is here the mode function of the fundamental gaussian TEM_{00} mode defined in equation (1.23). Later we use this approach to generalize the coupling constant to higher order transversal modes. If the frequency of the cavity resonance equals the atomic transition frequency (that is $\Delta = \omega_C - \omega_A = 0$), an initially excited atom will undergo Rabi oscillations with frequency g in the bare state basis $|g,1\rangle$ and $|e,0\rangle$. The Hamiltonian can be diagonalized and the new dressed states are now superpositions of the initial states given by:

$$\begin{aligned} |+\rangle &= \cos\phi\,|g,1\rangle + \sin\phi\,|e,0\rangle\,, \\ |-\rangle &= -\sin\phi\,|g,1\rangle + \cos\phi\,|e,0\rangle\,, \end{aligned} \tag{2.6}$$

where the mixing angle ϕ is defined by $\tan 2\phi = \frac{2g}{\Delta}$. The new eigen energies can be written as:

$$E_\pm = \hbar\frac{\omega_A + \omega_C}{2} \pm \hbar\sqrt{\left(\frac{\Delta}{2}\right)^2 + g^2}. \tag{2.7}$$

When the frequency of the cavity mode equals the frequency of the atomic transition the energies are symmetrically shifted around the bare excited state by $\pm g$. The frequency difference of the splitting $2g$ is called the *Vacuum-Rabi splitting* because it would even occur for an empty cavity mode with just a single excited atom. Spontaneous emission or the incoherent transition from the excited state to the ground state by emitting a photon would be completley suppressed and the dynamics became reversible. The excitation oscillates between mode and atom coherently. Since nobody would be able to observe this it would be of little scientific interest. The dynamics in any real atom-cavity system are accompanied by decoherence processes. The mirror loss rate κ as an incoherent cavity mode decay through each of the cavity mirrors and the spontaneous emission rate γ into residual vacuum modes. The coupled systems density matrix evolves according to the master equation [21, 86]:

$$\dot{\rho} = -\frac{i}{h}\,[H,\rho] + \mathcal{L}\rho, \tag{2.8}$$

with the dissipation manifested in the Liouville term:

$$\mathcal{L}\rho = \kappa\left(2a\rho a^\dagger - a^\dagger a\rho - \rho a^\dagger a\right) + \gamma\left(2\sigma_-\rho\sigma_+ - \sigma_+\sigma_-\rho - \rho\sigma_+\sigma_-\right). \quad (2.9)$$

With the system coupled like this to the environment, the vacuum Rabi splitting becomes observable in the case that $g > \kappa, \gamma$. This marks the so called strong coupling regime. If the Hamiltonian (2.1) gets extended by a coherent pumping term with amplitude η:

$$H_p = -i\hbar\eta\left(a - a^\dagger\right), \quad (2.10)$$

it can be seen either by fluorescence into non-cavity modes with a camera for example or with a photodiode in the cavity transmission. If the cavity resonance ω_C is carefully positioned at the atomic transition frequency ω_A so that $\omega_C = \omega_A \equiv \omega_0$ then the cavity transmission as a function of the pump frequency ω_P in the limit of a weak probe can be written as [3, 61]:

$$T\left(\omega_P\right) = T_0\left|\frac{\kappa\left[\gamma + i\left(\omega_0 - \omega_P\right)\right]}{\left(\omega_P - \lambda_+\right)\left(\omega_P - \lambda_-\right)}\right|^2, \quad (2.11)$$

with T_0 the maximum empty cavity transmission and $\lambda_\pm$ marking the new normal mode eigenfrequencies of the coupled system.

$$\lambda_\pm = \left(\omega_0 \pm \Omega_0\right) - i\left(\gamma + \kappa\right)/2, \quad (2.12)$$

with the frequency shift Ω_0 proportional to the coupling constant:

$$\Omega_0 = \sqrt{g^2 - \left(\frac{\gamma - \kappa}{2}\right)^2}. \quad (2.13)$$

As we will show later, the single-atom single-mode coupling constant for the experiment in this thesis is tiny. It is much smaller than the cavity loss rate κ or the polarization decay rate γ which in our case hardly differs from the free space decay rate, since the cavity is so big that the modes inhibited by the resonator are negligible.

Collective Coupling In 1954 Dicke [20] considered the radiative properties of particles close to each other quantum mechanically. His theoretical findings were that the emission properties of atoms confined in

a small space can hardly be seen as independent. On the contrary, if several atoms are within a wavelength from each other they have to be treated as a combined quantum system. The extension of the Jaynes-Cummings model to contain several atoms is called the *Tavis-Cummings model* and was published 5 years later to the single atom model in 1968 [92]. The polarization vector of each atom within the cavity adds up and the new system can be seen as a single atom with collectively enhanced coupling constant $g_{eff} = g\sqrt{N}$ where N is the effective number of atoms coupled to the cavity according to the weighted sum over all the atoms with position r_i:

$$N = \sum_{i=1}^{atoms} |u(x_i)|^2 . \tag{2.14}$$

Atoms within the mode count while atoms not in the mode have no effect. In the case where we know the density function of for example the MOT ρ_{MOT} the effective coupling g_{eff} is given by the integral:

$$g_{eff} = g\sqrt{\int |u_{00}(x)|^2 \rho_{MOT}(x)\, dV}. \tag{2.15}$$

The new coupling constant can be orders of magnitude bigger than the initial single atom g just by adding more and more particles. The transmission of the cavity is still given by equation (2.11), except that the coupling constant g has to be exchanged with its collective counterpart g_{eff}. The characteristic $\sqrt{N}$ behaviour of the mode splitting is a hallmark of the collective strong coupling regime.

Chapter 3

Experimental Setup

This chapter will present the experimental setup designed, built and used for this part of the thesis. It will concentrate on the main components important for the experiment and skips, or deals very briefly with, more technical components such as current drivers, laser designs, magnetic coil switches and stabilization electronics, in an attempt to limit the scope of this work. It starts with a summary of the experimental control and briefly explains the MOT laser system. Then the vacuum chamber, as the main part of the experiment is described as well as its components and the chosen design criteria. Following this is a description of its interior parts, mainly the magnetic coil construction, its cooling and then finally the science cavity. After a brief characterization of the cavity's parameters and its stabilization system, the chapter ends with a description of the cavity probe laser locking schematic and a small summary. Where necessary, measurements to characterize the system are explained and presented.

3.1 Experimental Control

To run an experiment with cold atoms, lasers need to be controlled in both frequency and intensity. Currents through coils have to be changed and switched, and images of the atomic sample or the cavity mode must be acquired with high temporal accuracy and good reproducibility. It also needs to be easy to switch between different experiments, to change times and intensities, and to add or delete experimental steps. For this

experiment we use a LabVIEW 8.2 environment to control a Viewpoint DIO-64 digital in/out card, and two National Instruments PCI-6713 analog in/out cards. Those cards provide precision control of 64 digital, and 16 analog, channels (from -10 V to +10 V output) with a 2 μs resolution, and form the core of each experimental cycle. At the beginning of an experiment, the required values are written into the card's memory with an according time-stamp and executed repeatedly until further notice. For quick data acquisition, as well as for triggering other LabVIEW subroutines, the computer control was extended by a NI-USB-6009 card with an additional 8 analog inputs and 2 analog outputs. The computer also controls the frequencies of a Rohde & Schwartz SMF 100A 1-20 GHz function generator over a LAN connection, a Rohde & Schwartz SMT 02 5 khz-1.5 GHz via the COM port, and an AVT Guppy F038B camera via FireWire. The camera is used for fluorescence imaging of the MOT to measure the temperature, position, size of the cloud and the number of atoms. The images are acquired, background subtracted and immediately analyzed in terms of a 2D Gaussian fit in MATLAB. The values are written into a file, but also immediately displayed to be able to check the experiment in real-time. For triggered data acquisition, a digital oscilloscope[1] is connected over another USB port. Driven by LabVIEW it acquires and stores data when temporal information is required. The cavity transmission for chapter 5 is recorded with an intensified[2] camera from Hamamatsu[3]. Since it is originally from a different experiment in our group [77], it came with its own control computer, which receives a trigger signal from the main experimental control and uses WASABI as the camera control and image analysis program.

3.2 Magneto-optical trap laser system

Three lasers are used to generate the light necessary to run the MOT. The repumper, the master and the slave. The repumper and master are Extended Cavity Diode Lasers (ECDL), home built for this experiment according to a design published in Optics Communications 1995 [82].

[1] Tektronix DPO 2014
[2] Image Intensifier Unit C9016-24, Hamamatsu
[3] IEEE1394 Digital CCD Camera C4742-80-12AG, Hamamatsu

Laser in the Littrow Configuration The laser systems contain commercially available laser diodes[4] in the so-called Littrow configuration. In this configuration a holographic grating is used to control the frequency of the laser emission by feeding back one of the first-order grating refractions into the diode. A welcome side-effect is the corresponding linewidth reduction of the laser since the newly formed extended cavity is much longer (1.5-2 cm) than the initial laser cavity ($150 - 400\,\mu$m). The frequency of the laser becomes controllable by changing the angle of the grating. This can be done very quickly with a piezo ceramic[5]. Changing the angle not only changes the wavelength of the refracted light but also, since it is done over a pivot point, the length of the cavity. Both effects alter the emission frequency, but not necessarily in the same way and the optimimum scanning range can be achieved when both effects happen synchronously [19]. The whole ECDL is actively temperature stabilized and sits in a rigid aluminium body. With commercially available laser diodes, the output power after the grating is around 30 mW for 852 nm.

The other type of laser, the slave, is just a laser diode injected by light from the master laser. Even tiny amounts of light (just a few μW) are enough to dominate its frequency. The diodes[6] used here are more powerful; at a current of 150 mA the laser delivers about 70 mW. Figure 3.1 shows a schematic of the laser system to operate the MOT. The master laser, providing the cooling light, is locked via a so called Doppler-Free Dichroic Atomic Vapour Laser Lock (DF-DAVLL) [91].

Dichroic Atomic Vapour Laser Lock This lock combines a Doppler-free spectroscropy with a small magnetic field to generate an error signal which is an electronic feature linear in frequency through the atomic transitions [67]. In the external magnetic field the atomic magnetic sublevels are slightly shifted in energy due to the Zeeman effect. The optical frequency of the Doppler-free feature depends now on the polarization of the observed light. A Polarizing Beam Splitter cube (PBS) in combination

[4] Hitachi HL8342-MG
[5] PiezoMechanik, PSt 150/4/5
[6] SDL Inc., SDL-5422-H1

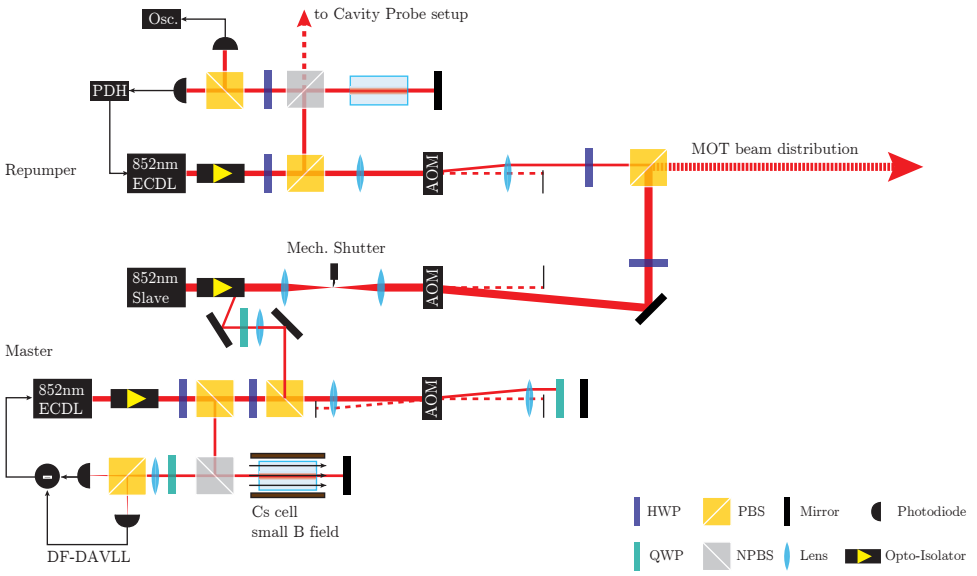

Figure 3.1: A schematic of the laser system for the magneto-optical trap as explained in the text.

with a Quarter Wave Plate (QWP) splits the two circular polarizations and guides them onto different photodiodes. An integrated circuit subtracts one signal from the other, leaving a nice slope around resonance. This error signal is then fed back to the piezo of the laser, keeping the frequency where it is supposed to be. As a standard on this experiment, the error signal is also fed back to the modulation input of the current driver. This improves the stability of the lock in the worst case and provides also some linewidth narrowing in the best case. We experimented quite substantially with different DAVLL configurations and abandoned it in most setups in favour of Frequency Modulation (FM) locks [6]. Their biggest disadvantage was the susceptibility to temperature fluctuations in the lab, which affected the lock point. Their biggest advantage, however, is the lack of modulation side bands, especially for the master laser and its required detuning range to the cycling transition. If the detuning equals the modulation frequency, the single resonant side-band would heat the atomic sample. This is the reason why the master laser is still using the DF-DAVLL.

The locking point of the master laser is the $6^2S_{1/2}F = 4 \Rightarrow 6^2P_{3/2}F = 4, 5$ cross-over line. Most of the light then goes through an Acousto-Optical

Modulator[7] (AOM) in a double-pass configuration, which shifts its frequency up by about $150-210\,\mathrm{MHz}$, so that it is above the atomic cycling transition. Over the applied radio frequency the light can now be tuned in frequency by means of the experimental control computer. After the AOM, the light gets injected into the slave laser. After a mechanical shutter, the laser beam is passed through another AOM, which shifts the frequency down by 80 MHz. This AOM is mainly used to switch or alter the beam intensity by changing the radio frequency amplitude applied to the AOM. After the AOM the power of the beam is $(29.3 \pm 0.1)\,\mathrm{mW}$. Before overlapping it with the repumping light, the beam goes through a couple of telescopes to become $(1.28 \pm 0.01)\,\mathrm{cm}$ in diameter. The peak intensity of the MOT beam is $(45.7 \pm 0.6)\ \mathrm{mW/cm^2}$ corresponding to $(16.9 \pm 0.2)\ \mathrm{I}_{Sat}$.
The repumping laser does not need to be detuned and keeps a fixed frequency during the whole experimental cycle. Side-bands do not matter, since it is lasing all the time on-resonance. Therefore it can be locked using a Frequency-Modulation spectroscopy lock.

Frequency Modulation, or Pound-Drever-Hall, Lock In Frequency Modulation locking systems the light source in question is equipped with side-bands in frequency. In our case we modulate the diode current with a 40 MHz sine signal directly. The electronics are self built at UCL and follow the design in [70]. The modulation produces side-bands in the laser frequency at $\pm 40\,\mathrm{MHz}$ with respect to the carrier frequency. Its index is small and the power in the side-bands is about 1%. If this laser source now probes any kind of resonance feature, one side band will be below resonance and the other will be above resonance, when the carrier is on resonance. The phase difference will be imprinted on the relative phase of the 40 MHz signal, which can be read out with a photodiode and compared to the initial phase of the modulation signal. This phase difference is used as the error signal in the feedback loop.

The repumper is locked to the Cs $6^2S_{1/2}F = 3 \Rightarrow 6^2P_{3/2}F = 3, 4$ cross-over feature. It then gets shifted up by 125 MHz using the first refracted order of an AOM onto the $6^2S_{1/2}F = 3 \Rightarrow 6^2P_{3/2}F = 4$ repumping tran-

[7] Crystal Technology, 3110-140

sition. A fraction of the light before the AOM gets split off and sent to the Cavity Pumping laser system as an atomic reference signal.

3.3 Vacuum system

The vacuum chamber is the main part of the experimental hardware. It is necessary to keep environmental influence to a minimum. Producing a cloud of 10^7 Caesium atoms at some tenth of μK above absolute zero obviously needs good thermal insulation. Collision with hot background atoms is a significant loss mechanism and heating source. To load the MOT, the chamber is filled with a low pressure gas of Caesium atoms. The MOT then cools and traps the cold fraction of the Boltzman distribution, while hot atoms are mostly unaffected by the cooling process due to its limited capture range. The Caesium is produced by heating up dispensers[8] in the appendix part of the vacuum chamber. They are separated from the main body by a UHV valve, in order to be able to change them when necessary without having to pump and bake the whole vacuum system again.

The chamber can be separated into three parts: the experimental part, the pumping section and the ^{133}Cs source. The experimental chamber is an Extended Spherical Octagon[9], and it was chosen due to its high port density, huge optical access and rigid design. Optical access for the three orthogonal MOT beams, a camera, the cavity probe laser and the cavity access was needed. Additional mounting capacity was also needed for the cavity spacer, the magnetic coil construction and its cooling system and also for the electrical feed throughs to drive the piezo and the coils. The two 8" viewports, and all the other viewports for the MOT beams, were coated for lower reflectivity.
The pumping section (on the right in figure 3.2) is equipped with a 20l/s Ion pump[10], a viewport to probe or pump the MOT and a valve to provide access for a turbopump. The pressure in the chamber can be deduced from the ion-pump current. It is at the lower end of the measuring range

[8]SAES Getter, Cs AMD Cs/NF/10.8/25/FT 10
[9]Kimball Physics, MCF800-ExtOct-G2C8A16
[10]Varian Inc.,Vaclon Plus 20 StarCell

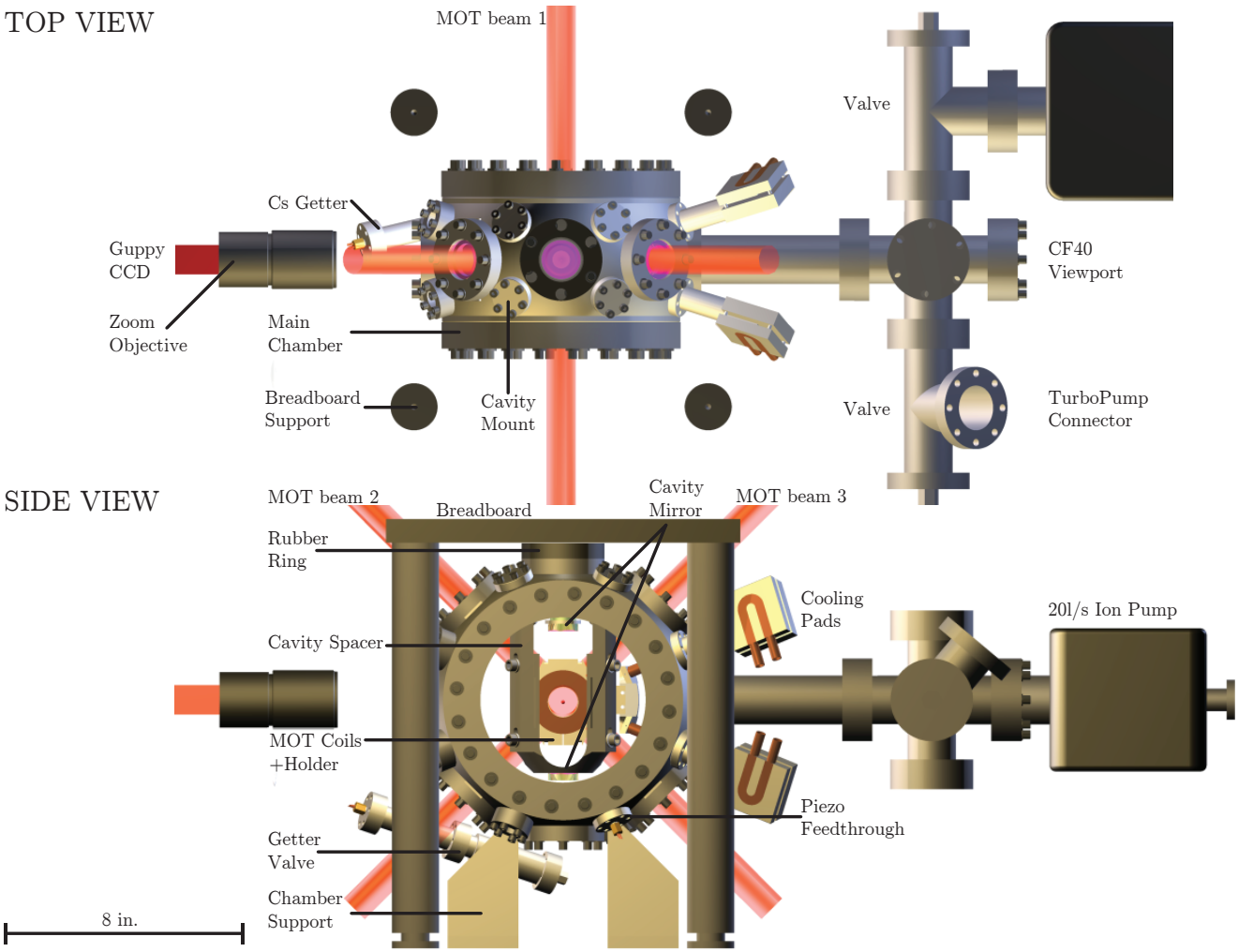

Figure 3.2: The vacuum setup. It shows a view from the top and a view from the side of the main experimental components. Apart from the vacuum chamber, the sketch shows also the imaging system and the orientation of the three mutually perpendicular MOT laser beams, as well as the mounting construction of the main chamber. It is clamped between two aluminium mounts and the breadboard containing the optics for two MOT beams and the cavity probe beam (not visible). For mechanical isolation, all the supports are covered with soft rubber.

and therefore below 10^{-9} mbar. Figure 3.2 shows a schematic of the vacuum chamber; first a picture from the top and then a picture from the side.

Magnetic Field The first coils to produce the gradient for the MOT were mounted outside of the vacuum chamber. They were about 20 cm in diameter with 200 windings of 1 mm copper wire each. They needed

water-cooling and they were slow to switch due to their high electromagnetic induction and the voltages available. Eddy currents induced in the cavity spacer caused mechanical vibrations for higher magnetic fields, so another set of coils was designed, built and put into the chamber. The

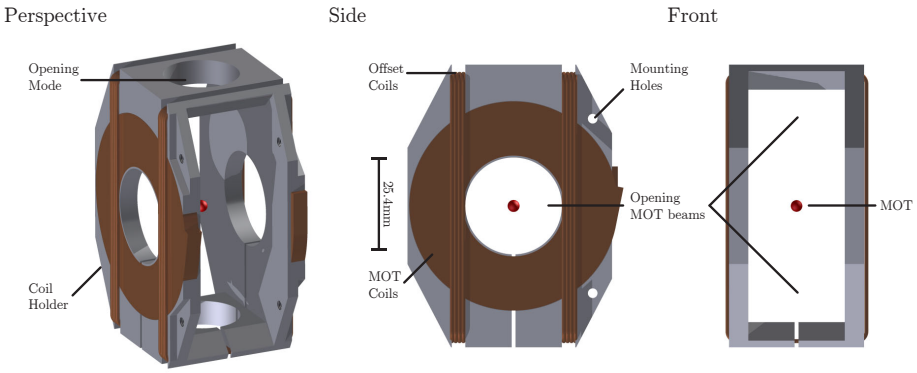

Figure 3.3: The magnetic coil mount in the vacuum chamber. Two pairs of coils provide a magnetic quadrupole field for the MOT with a moveable magnetic zero within the cavity mode.

new coils are much smaller, switch much quicker and the dissipation during MOT operation is negligible. Also the field at the position of the cavity spacer is much smaller so that the induced currents cause much less mechanical response.

Figure 3.3 shows the spacer of the magnetic coils. It contains the two anti-Helmholtz (round) coils used for the MOT gradient. To have the ability to move the magnetic field zero, both coils can be supplied by differing currents. For movements of the magnetic zero in the direction perpendicular to the connection of the two AH coils, another pair of coils is mounted on the spacer. It is used in a Helmholtz-configuration but could also be used to generate the MOT gradient, for example to get a more elongated MOT in the cavity. Both pairs of coils do not need any cooling during normal MOT operation. Since we wanted to have the possibility to provide higher magnetic field gradients for a quadrupole trap however, the dimensions and the materials of the mounting construction were chosen in a way to provide enough cooling, and to avoid melting the wire's Kapton insulation. It turned out that cooling the construction during MOT operation improves the vacuum as well, so that for most experiments the cooling was on. It also showed that with cooling the magnetic coil cage, the cavity spacer got cooled as well so that it

changed its length by some μm. The wire for the coils is fixed to the spacer with a low vapour pressure resin[11]. In order to keep the expected pressure increase due to the higher outgassing in the chamber as small as possible, the use of the glue was kept to a minimum. An increase in overall pressure after baking the system again and pumping it down was not measurable.

The AH coils produce a magnetic gradient of $(13.75 \pm 0.08)\,\frac{\mathrm{G}}{\mathrm{cm\,A}}$. The

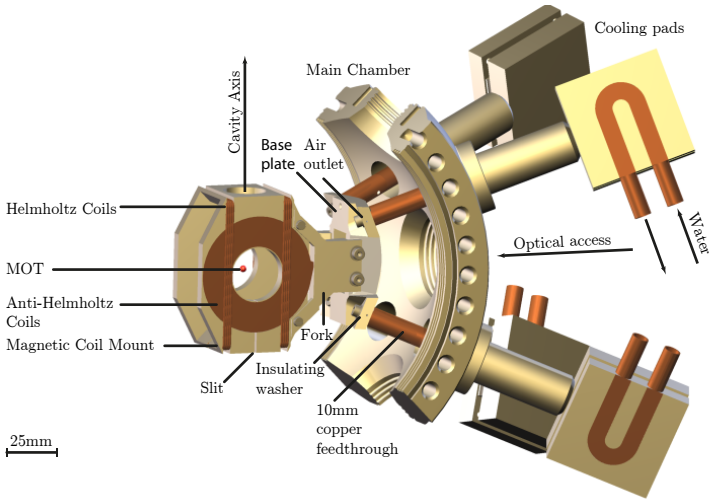

Figure 3.4: The magnetic coil cooling apparatus. The magnetic coil cage is mounted to a base-plate in the vacuum chamber. This base plate is screwed to four 10 mm diameter copper feed throughs. The electrical contact is interupted by ceramic washers on both sides of the base-plate. The other side of the feed throughs is cooled with water cooled Peltier elements as explained in the text.

dissipation is well below 1 W for an axial gradient of $10\,\frac{\mathrm{G}}{\mathrm{cm}}$ usual for MOT operation. This does not increase the temperature of the copper wire measurably. Pulsed currents of up to 15 A can be used to provide magnetic trapping, which has been tried but was not necessary for experiments in this thesis. The cooling system is shown in figure 3.4. The magnetic coil mount is connected over two forks to a base-plate, which acts as a heat reservoir for the coils. Its heat is extracted over four 10 mm diameter copper feed throughs, which also act as the mechanical mount for the magnetic coil cage. All other parts are manufactured from aluminium and are connected via brass screws. To avoid induced currents all components are slit. The copper rods are electrically insulated

[11] Torr Seal from Varian

via ceramic washers. Outside of the vacuum the copper rods are fitted into aluminium plates. These plates are cooled via Peltier elements[12] sandwiched between the plates and a water-cooled aluminium element[13]. The temperature of the magnetic coil cage was measured indirectly by observing the resistance change of the copper wire. According to the measurement, the temperature dropped by about 40 °C to about −20 °C with a cooling power of 120 W applied to all four Peltier elements together.

3.4 Science cavity

The science cavity is the crucial part of the experiment. The aim was to design the cavity as long as possible to increase the interaction volume, so that as many particles as possible could be loaded into the mode. Hence some theoretical publications [21, 85, 100] suggest that the cooperativity scales with the transverse mode density another aim was to be as confocal as possible. Then the transverse modes overlap in frequency and the active volume where atom-cavity interaction occurs, as well as its strength, increase dramatically.
To be able to compare results with previous work the cavity parameters were chosen to be similiar to an experiment conducted in Vladan Vuletic's group in 2003 [15]. Temperature fluctuations and vibrations alter the cavity length and therefore the resonance frequency. Those changes during an experimental run should be below a cavity linewidth. To establish this we implement a computer controlled active stabilization of the resonance frequency. This section consists of three parts: First an overview of the cavity construction is given, then the length stabilization is explained, and finally, the procedure and the results of the confocal alignment are displayed.

3.4.1 Cavity construction

The cavity consists of two mirrors with a curvature of 12 cm and a broadband reflectivity of 99.9 % peaked around 852 nm. They are 25.4 mm in

[12] Farnell, Peltier Cooler MCPE-127-10-13
[13] Aavid Thermalloy Hi-Contact^{TM}liquid cold plates, 2 pass model

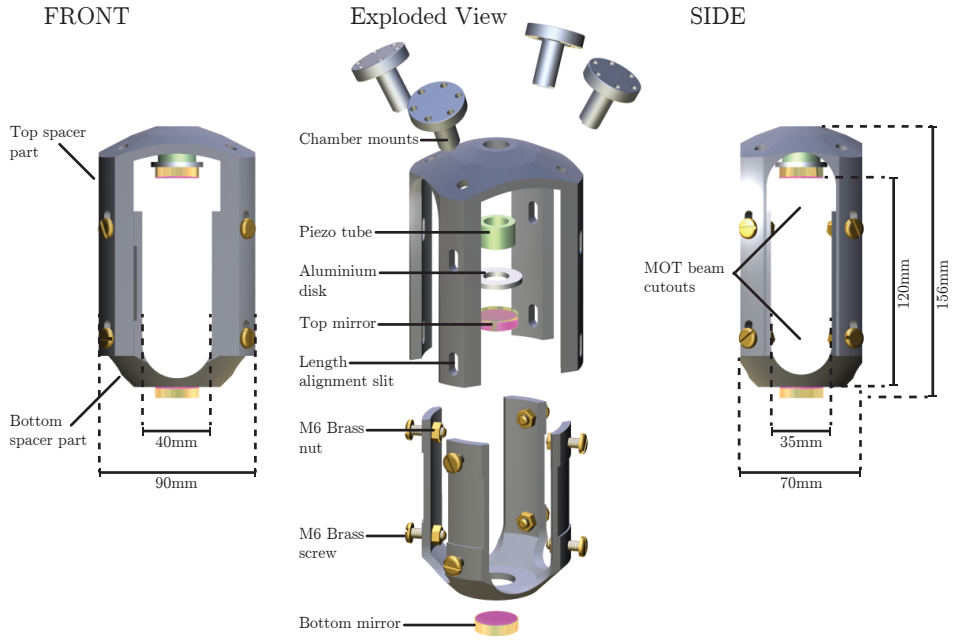

Figure 3.5: Three views of the science cavity construction. The cavity spacer is made from two aluminium parts machined in the UCL workshop. The design priorities were optical access, stability and a maximum cavity length. Construction details are explained in the text.

diameter and 6.35mm thick.[14]. Separation is provided by an aluminium spacer built at the UCL workshop. This spacer was designed for optical access to the MOT and the cavity mode, and is made as rigid as possible to reduce the susceptibiliy to vibrations. Aluminium was chosen due to its small paramagnetism and its mechanical properties.

It consists of two parts screwed together by eight brass M6 screws, washers and nuts. The lower mirror is glued to the outside of the lower spacer part, while the upper mirror is glued to an aluminium plate and then onto the piezo ceramic connected to the inside of the upper spacer part. The glue used was TorrSeal, which is suitable for high vacuum applications. The disc was placed between the mirror and the piezo tube to avoid stress on both components while actuating. The whole spacer is connected with four stainless steel mounts to the four top CF16 ports of the extended spherical octagon from Kimball Physics. During the construction phase, the length of the spacer could still be changed due

[14]Layertec Laser Mirror

to the length alignment slits; with loosened screws they allow for rough adjustments of ±4 mm.

Aligning for confocality First the upper part of the cavity spacer was prepared. First by cleaning all components in an ultrasound bath with dry acetone. Then the mirror was centred and glued onto the aluminium plate, the plate glued to the piezo ceramic, which itself was then connected to the spacer part. This construction was then mounted vertically in the lab with an incident 852 nm laser beam on the middle of the mirror. The beam was then back-reflected onto itself to model the position of the mode. The lower mirror, in a normal 1"-mirror mount, was then put into a position roughly 12 cm away from the upper mirror surface. After a bit of alignment a cavity was formed and the recorded transmission showed a rich resonance spectrum. Moving the lower mirror with a 3D translation stage and the mirror mount enabled us to couple most of the light into the 0th-order transverse mode of the cavity, which could be identified with a CCD camera and a monitor.

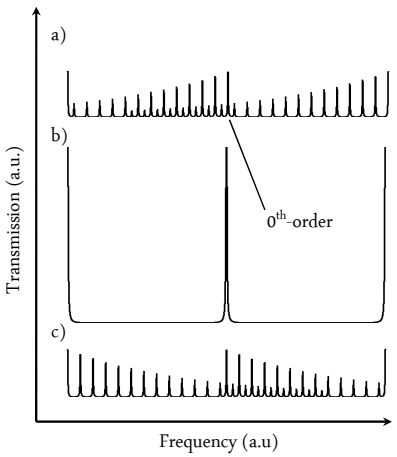

Figure 3.6: Mode spectrum around confocality. a) shorter than confocal, b) exactly confocal and c) longer than confocal

With misaligning the incoupling laser beam, light was coupled into different higher order transverse modes, so that the spectrum showed several higher order transmission peaks. With their frequency separation, the deviation from confocality could be estimated and reduced via the translation stage. Once all of the transverse modes were overlapped in one single peak, the peak height was maximized and the lower part of the spacer put into a position nearly touching the lower mirror. After tightening all the screws holding the two spacer parts together, the gap between mirror and spacer was bridged using four spots of TorrSeal. When the glue was cured, the mirror mount could be removed and the

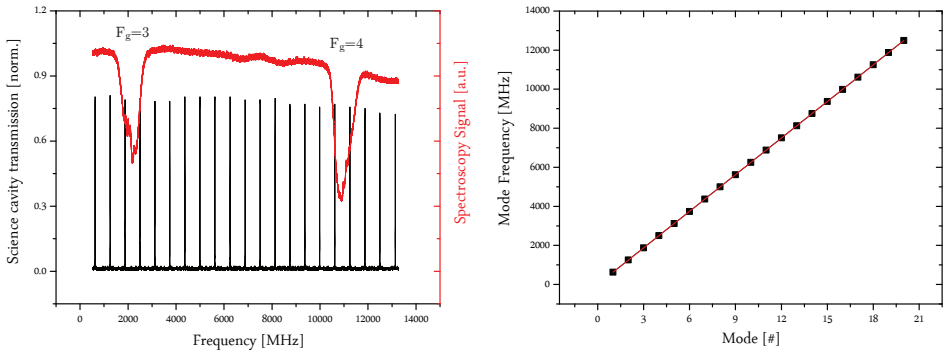

Figure 3.7: Left: The transmission through the cavity (black) while scanning a laser over all Cs $6^2S_{1/2} \Rightarrow 6^2P_{3/2}$ (red) features to calibrate the frequency axis.
Right: The mode number over mode frequency. The linear fit gives the mode spacing, which for a confocal cavity is half of the free spectral range.

rigid construction mounted into the vacuum chamber.

3.4.2 Cavity parameter

Free Spectral Range The free spectral range of a cavity is inversely proportional to the cavity's optical path length, and the optical path-length is important for the mode volume and the deviation from confocality.

To measure it we scanned a laser over the cavity whilst simultaneously performing a Doppler free spectroscopy on a Caesium cell. The transmission of the cavity showed a slight non-linearity in the mode-spacing. This was more an expression of the non-linear change in frequency when a linear ramp is applied to the ECDL piezo voltage, rather than an actual length change of the cavity. So before calibrating the frequency axis with the doppler free Caesium spectroscopy, the non-linearity was mathematically corrected. The transmission of the cavity, and the spectroscopy signal over the calibrated frequency axis, are displayed in figure 3.7.

From this graph the frequencies of the longitudinal cavity modes were selected and displayed as a function of the longitudinal mode index in figure 3.7. A linear fit of the data revealed the free spectral range to be:

$$\mathrm{FSR} = (1249.5 \pm 0.4)\ \mathrm{MHz}. \tag{3.1}$$

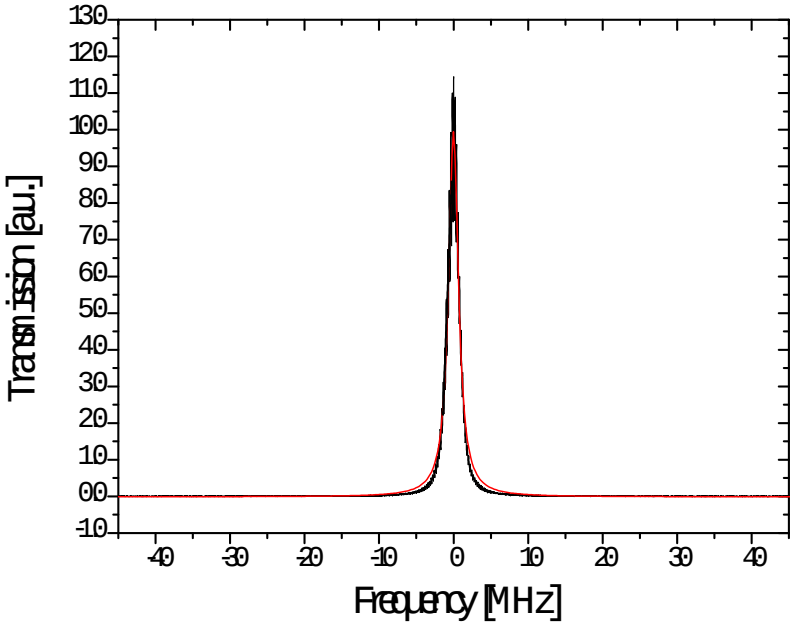

Figure 3.8: The cavity transmission as a function of the laser frequency. The photodiode signal (black) was fitted with a lorentzian (red) revealing a linewidth (FWHM) of $w = (1.603 \pm 0.003)$ MHz.

From this the actual length of the cavity can be deduced:

$$L = (119.96 \pm 0.03) \text{ mm}. \tag{3.2}$$

Using this method, the error in the cavity length is already about twice as large as the maximum change in cavity length with the piezo ceramic, so that the actual piezo voltage could be neglected.

Linewidth and Finesse The cavity linewidth was measured in a similar way to the free spectral range. A laser scanning over a Doppler free Caesium spectroscopy of the Cs $6^2S_{1/2}F = 4 \Rightarrow 6^2P_{3/2}$ F=3,4,5 transition was simultaneously injected into the cavity. The transmission of the cavity was collected with a photodiode and recorded with an oscilloscope. The known frequency difference between two atomic features was then used to calibrate the frequency axis. The transmission feature was fitted with a Lorentzian peak function which revealed its linewidth, and therefore the cavity loss rate κ (Figure 3.8).

The resulting Lorentzian linewidth FWHM is:

$$w = \kappa/\pi = (1.603 \pm 0.003)\ \text{MHz}. \tag{3.3}$$

Together with the free spectral range (equation (3.1)) this results in a finesse F of:

$$F = (780 \pm 2)\,. \tag{3.4}$$

Mode volume and coupling constant With the cavity length the beam waist of the fundamental Gaussian TEM_{00} mode can be calculated with formula (1.22) for the D2 line transition wavelength of $\lambda = 852.347\,\text{nm}$ [87]:

$$w_0 = \sqrt{\frac{L}{k}} = (127.57 \pm 0.02)\ \mu\text{m}. \tag{3.5}$$

To a very good approximation, just neglecting the curvature of the mirror surface, this results with equation (2.5) in a mode volume of:

$$V_{00} = \int^V |u_{00}(\vec{x})|^2\, dV = (1.533 \pm 0.001)\ \text{mm}^3 \tag{3.6}$$

and from this we finally arrive at the theoretical single atom single mode coupling constant g_{00} of the cavity system for a ^{133}Cs atom in the stretched magnetic sublevel $|F = 4, m_F = \pm 4\rangle \rightarrow |F' = 5, m'_F = \pm 5\rangle$ subject to on resonant $\sigma_\pm$ light and therefore a dipole moment of $\mu = 2.6850\,(24) \times 10^{-29}\,\text{C} \cdot \text{m}$ [87]:

$$g_{00} = \frac{\mu E_1}{\hbar} = 2\pi \times (118.94 \pm 0.02)\ \text{kHz}. \tag{3.7}$$

This cavity is deep in the bad cavity limit with $g \ll \kappa < \gamma$. The single-atom single mode interaction is dominated by environmental decoherence processes.

Maximum length change of the cavity The maximum length change of the cavity is important for two reasons. First, drifts in temperature, and therefore a length change of the cavity, can be compensated when the system is locked. The maximum length change provides an upper limit for a temperature change that can be compensated for. But more

importantly, it enables the possible change in length to get closer (or further) to (or from) perfect confocality, to change the degree of degeneraty of the higher order transverse modes. To measure the length change, a laser scanning over the Caesium $6^2S_{1/2}\ F = 4 \rightarrow 6^2P_{3/2}\ F = 5$ crossover transition was coupled into the 00-mode of the science cavity. This was used as a frequency standard. Changing the applied piezo voltage of the science cavity showed moving resonance peaks in the transmission as recorded on a photodiode. Each new longitudinal mode corresponds to a cavity length change of $\lambda/2$. Thus the piezo was scanned from the minimum to the maximum available voltage and the number of modes in the transmission passing the crossover feature were counted, and the corresponding voltages recorded. The length change per mode is given

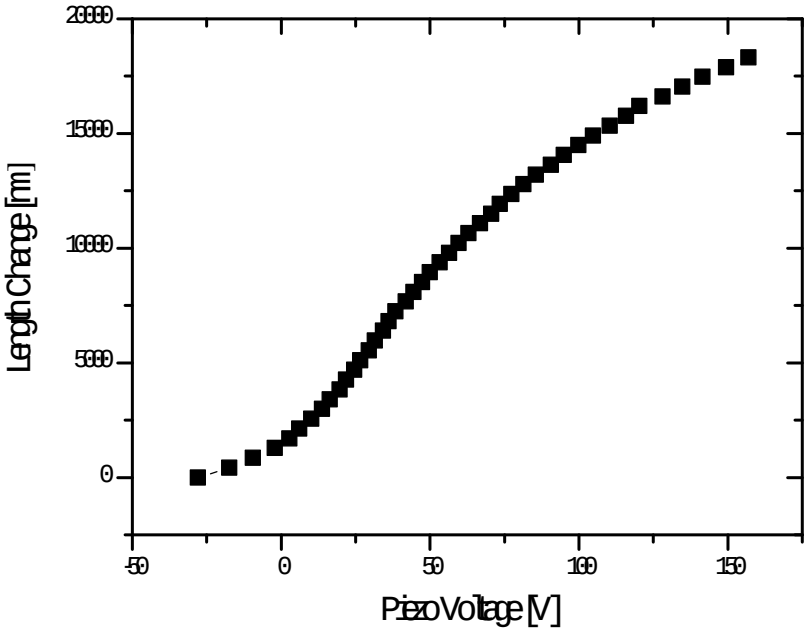

Figure 3.9: The maximum length change of the cavity measured via counting the number of observed resonances of an 852 nm laser.

by:

$$\Delta L = \frac{\lambda}{2} = \frac{(852.3473 \pm 0.0002)\,\mathrm{nm}}{2} = (426.1736 \pm 0.0001)\,\mathrm{nm} \qquad (3.8)$$

The error results from the presumption that over the whole time the measurement took, the cavity eigen frequency and the laser frequency

changed less than 100 MHz due to thermal or mechanical drifts, which was clearly justified. 43 different longitudinal modes could be observed. And thus total maximum length change is therefore:

$$\Delta L_{Max} = 43 \cdot \Delta L = (18325.45 \pm 0.01)\,\mathrm{nm} \tag{3.9}$$

Neither the minimum nor the maximum voltage coincided with a cavity mode, so that in fact the real maximum length change is more than 18.325 μm and less than 18.751 μm (corresponding to 44 longitudinal modes), which leaves us with a less optimistic error value of:

$$\Delta L_{Max} = (18.5 \pm 0.4)\,\mu\mathrm{m} \tag{3.10}$$

3.4.3 Deviation from confocality

The mode degeneracy in a cavity is an important figure for estimating the number of modes the cloud of atoms can interact with. In an ideal confocal cavity all of the higher order transverse modes with the same sum of longitudinal and transverse mode indices have exactly the same frequency. In general, our cavity, as well as everything else, has limited spatial dimensions, which introduces losses for modes with a bigger radius than the radius of the mirrors. Also the frequencies for higher order modes differ and since confocality is an exact point, there will always be a finite frequency difference. In addition to this, the mirrors are not parabolic, they are spherical mirrors. We investigated whether there are dielectric parabolic mirrors with an appropiate surface and coating quality, but could not find any off the shelf. And we decided against a custom made solution as a result of a cost-benefit analysis. Therefore we have to take spherical aberration into account. In this subsection the means to measure the deviation from confocality, as well as the results, will be presented.

Taking into account real mirrors and aberration Spherical mirrors in Fabry-Pérot Resonators are a source of spherical abberation. This makes the optical path-length inside the cavity and therefore the resonance condition a function of the radius on the mirror. In [99] the optical path-length corrected for spherical aberration, astigmatism and beam

front curvature is given by:

$$\Delta = 4(R+\epsilon) - \left[\frac{{\rho_1}^2{\rho_2}^2 \cdot \cos 2\theta}{R^3} + 2\epsilon(\frac{{\rho_1}^2 + {\rho_2}^2}{R^2})\right]. \tag{3.11}$$

Here ϵ is the length by which the cavity exceeds the confocal spacing $L = R$. R is the curvature of the mirrors. ρ_1 and ρ_2 are the fringe radii on the corresponding mirrors and θ is the angle between the cavity axis and the incoming light beam. For a small, central and well collimated beam $\cos 2\theta \approx 1$, so that equation (3.11) becomes :

$$\Delta = 4(R+\epsilon) - \left[\frac{\rho^4}{R^3} + 4\epsilon\frac{\rho^2}{R^2}\right]. \tag{3.12}$$

The resonance condition for light transmission of the cavity can then be written like:

$$n \cdot \frac{\lambda}{2} = 4(R+\epsilon) - \left[\frac{\rho^4}{R^3} + 4\epsilon\frac{\rho^2}{R^2}\right]. \tag{3.13}$$

Measuring the deviation from confocality In [15] they had a similiar cavity and therefore a similar problem in measuring the deviation from confocality precisely. They came up with a solution pointed out to them by [99], which is to observe the interference pattern of the light in the transmission of the cavity, while slowly changing its length. The observed fringe pattern then indicates the deviation from confocality especially when the cavity is shorter. Figure 3.10 shows the optical path-length as a function of the beam radius on the mirror for different deviations from confocality on the left. Clearly visible are the additional maxima for negative deviations from confocality. This manifests itself as merging fringes while scanning the mirror separation or the incident laser frequency. From the radius ρ of the merging fringe it is possible to deduce the seperation of confocality via:

$$\rho = \sqrt{-2\epsilon \cdot L}. \tag{3.14}$$

In [15] they used this method to determine the deviation from confocality of their cavity. It works because the cavity is shorter than the curvature

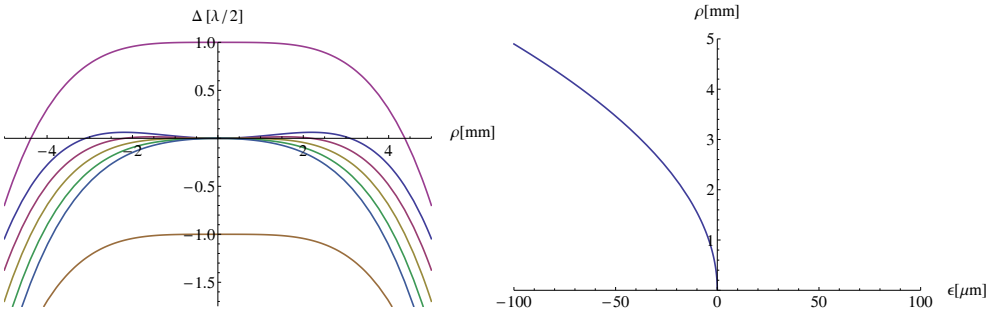

Figure 3.10: Deviation from confocality simulation.
Left: This graph shows the resonance condition of a cavity as a function of the radius ρ on the mirror (Equation 3.13). The central mode is displayed with different deviations from confocality and calculated for $R = 0.12\,m$. From top to bottom: $\epsilon = (-20, -10, 0, 10, 20)$ μm.
Right: The merging radius ρ of the fringe pattern over the deviation from confocality ϵ. No solution when the cavity length exceeds the radius of curvature ($\epsilon < 0$).

radius of the mirrors. For our science cavity we could not observe a merging fringe pattern in the transmission while changing the cavity length, which leads to the conclusion that in our case ϵ is positive.
Our way to overcome this problem was to measure the radius ρ of the fringe pattern as a function of the frequency of a probe laser, and then to fit it with equation 3.13. To do that we changed the piezo voltage to the minimum value and locked the cavity. Then we used the cavity probe laser and scanned it slowly over the resonance of the cavity, taking a webcam picture of the transmission every 10 MHz, and fitted an ellipse to the fringe pattern.
An example of the acquired images is shown in figure 3.11 on the right. Clearly visible is the aspect ratio and the orientation of the ellipse, and also a very faint second fringe which belongs to the next order. The long axis and the short axis were recorded for each image. Then we repeated the procedure after relocking the cavity (90 ± 1) FSR/2 of the 780 nm laser, or (17.5 ± 0.2) μm, shorter. Each dataset was then fitted with function (3.13). The resulting graph is shown in figure 3.11. The

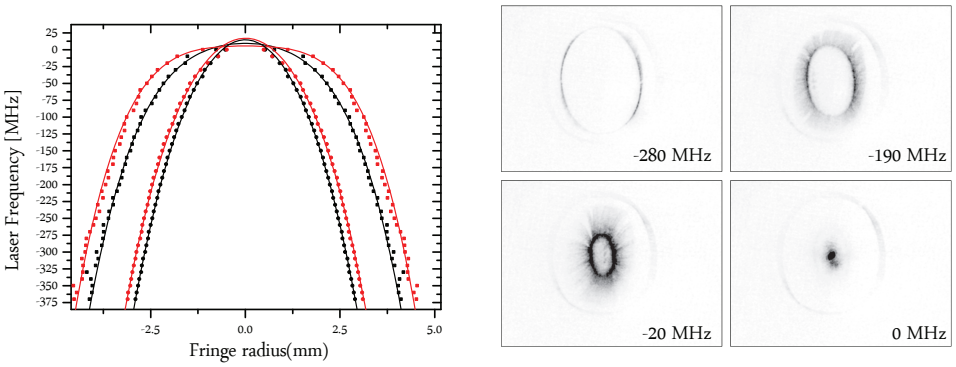

Figure 3.11: Measurement of the deviation from confocality.
Light: The frequency of the incident laser light over the measured radii of the ellipse in the two distinct directions (long axis: outer sets) for two different cavity length (red and black).
Right: The transmission of the cavity observed with a webcam for four different laser frequencies. Those frequencies are measured with respect to the resonance frequency of the 00-mode

deviation from confocality for the two axes are:

$$\begin{aligned} &\text{Long axis:} \\ \epsilon_{LA\,1} &= (21.9 \pm 1.4)\,\mu\text{m} \\ \epsilon_{LA\,2} &= (5.8 \pm 0.7)\,\mu\text{m} \\ \hline \Delta\epsilon_{LA} &= (16.1 \pm 1.6)\,\mu\text{m} \end{aligned}$$

$$\begin{aligned} &\text{Short axis:} \\ \epsilon_{SA\,1} &= (94 \pm 3)\,\mu\text{m} \\ \epsilon_{SA\,2} &= (76 \pm 4)\,\mu\text{m} \\ \hline \Delta\epsilon_{SA} &= (18 \pm 5)\,\mu\text{m} \end{aligned}$$

Both deviations are consistent within their error with the change in the cavity length ($(17.5 \pm 0.2)\ \mu$m) between the two measurements. The observed astigmatism is probably due to stress on the mirror during the alignment procedure. At this stage the mirror was mounted in a normal 1”-mount and secured with a plastic screw, which compressed the mirror along one axis. This quite obviously reduces the available mode density, since the transverse mode spacing in the direction with the large deviation from confocality is too big and the higher order transverse modes far less degenerate.

Mode degeneracy A statement about the degree of mode degeneracy can be made by considering the amount of higher order transverse modes per linewidth for a given deviation from confocality. With equation (1.24) this results, for the different values of deviation from confocality, in the following modes per linewidth:

$$\begin{aligned}
&\text{Long axis:}\\
&\epsilon_{LA\,1} \quad = (21.9 \pm 1.4)\,\mu\text{m} \quad \Rightarrow 11\frac{Modes}{w}\\
&\epsilon_{LA\,2} \quad = (5.8 \pm 0.7)\,\mu\text{m} \quad \Rightarrow 41\frac{Modes}{w}\\
&\\
&\text{Short axis:}\\
&\epsilon_{SA\,1} \quad = (94 \pm 3)\,\mu\text{m} \quad \Rightarrow 2\frac{Modes}{w}\\
&\epsilon_{SA\,2} \quad = (76 \pm 4)\,\mu\text{m} \quad \Rightarrow 3\frac{Modes}{w}
\end{aligned}$$

3.4.4 Cavity Stabilization System

To investigate the atom-cavity interaction in detail, the cavity eigen frequency needs to be stable, with respect to the atomic resonance frequency and, of course, with respect to the cavity cooling laser system. Figure 3.12 shows a the temperature related drift of the science cavity measured with the locking error signal from a previous stabilization setup. Even though the locking electronics have been replaced by a better version explained in more detail later in the text, what is clearly visible is the linear cavity drift of 500 kHz/s, which is obviously unacceptable for the experiment. It is also necessary to be able to tune the cavity length. Quickly on the timescale of one experimental cycle, computer controlled at best and, to reach every possible cavity-atom or cavity-laser detuning, at least by one half free spectral range, since this is the maximum possible detuning. To establish that, we implement two ECDLs lasing at 780 nm and three different locking schemes.

This section is structured as follows: firstly an overview of the complete locking schematic is given and the locks are briefly explained. Then each lock is presented with some explanation and, after that, the perfomance of the lock is demonstrated. The cavity length stabilization utilises three different locking schematics. One ECDL is stabilized via FM spectroscopy to the ^{87}Rb $5^2S_{1/2}F = 2 \rightarrow 5^2P_{3/2}F = 1, 3$ cross-over resonance feature. Another ECDL is stabilized onto a high order trans-

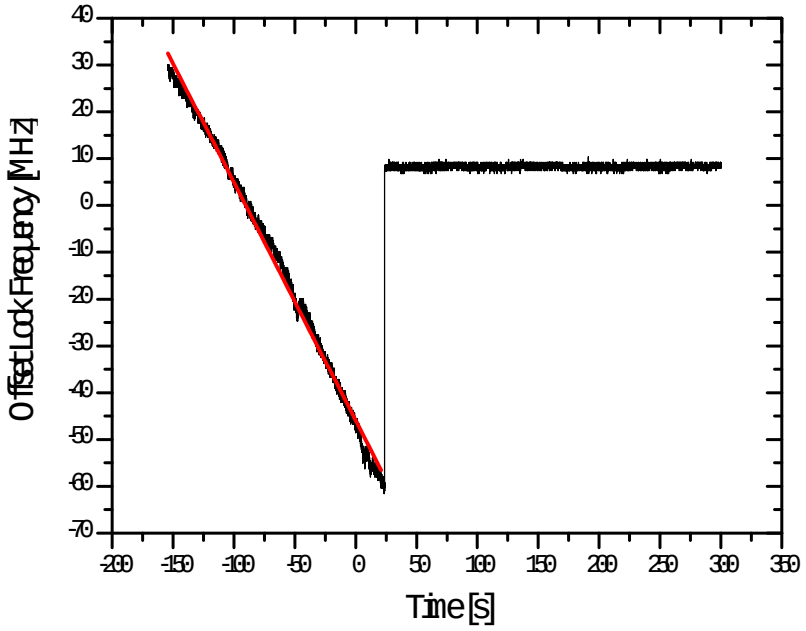

Figure 3.12: Linear drift of the cavity frequency in an old setup of the locking scheme. At $t = 25\,\mathrm{s}$ the locking system was activated.

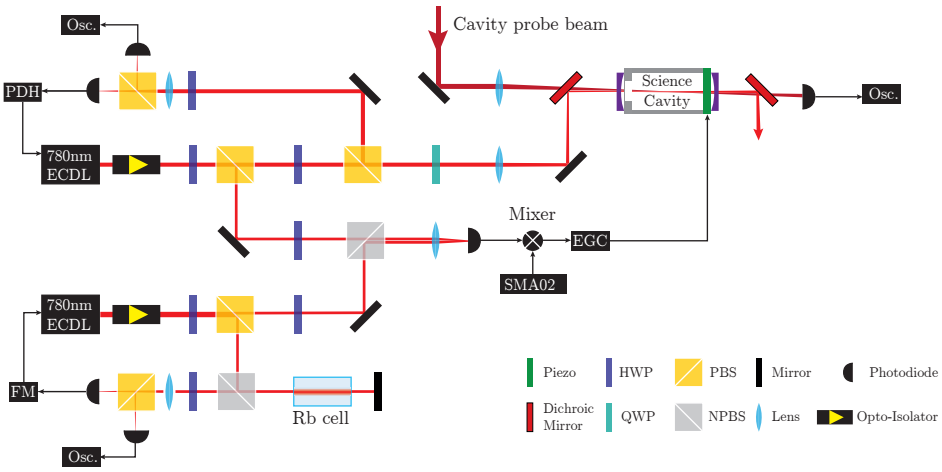

Figure 3.13: The cavity length stabilization setup.

verse mode of the science cavity. This is done with a Pound-Drever-Hall locking scheme [6] (which uses the same electronic components as the FM spectroscopy). Then parts of both lasers are overlapped on a photodiode and the homodyne signal is measured. This signal is mixed with the output of a computer-controlled frequency generator and an error signal is produced according to an offset locking technique developed in the group of Martin Weitz [83], which is then fed back to the cavity piezo.

Side of filter Offset lock This technique uses the frequency response characteristic of a 200 MHz low pass filter. The beat signal of the two ECDLs is measured with a fast photodiode[15]. The DC components of the light are filtered out by a Bias-Tee[16] and the remaining beat signal is amplified[17] and then mixed[18] down with the computer-controlled signal from a function generator[19]. After the mixer, the signal oscillating with the frequency difference of the two inputs is amplified[20], while the signal oscillating with the sum is discarded (or simply not amplified). This is then fed into the Error signal Generating Circuit (EGC). The frequency response of this circuit is shown in figure 3.14. The input frequency is the amplified output of the mixer. The slope of the error signal around 168 MHz frequency offset is (9.48 ± 0.01) mV/MHz. This signal locks the cavity length to an atomic reference.

3.5 Cavity Probe Laser System

The cavity probe laser system works in a similar way to the cavity stabilization laser system. We wanted to be able to lock the laser at any detuning possible to the cavity and to the atomic transition, and the laser should stay at this frequency over the duration of an experiment. In general everything written in the introduction of the cavity stabilization system is also true for the interrogation laser. The schematic of the system is shown in figure 3.15. The master laser is initially stabilized

[15] Hamamatsu G4176-03
[16] Minicircuits, ZX85-12G+ 0.1-12000 MHz
[17] Minicircuits, ZKL-2 10-2000 MHz
[18] Minicircuits, ZFM-2000
[19] RS SMT 02
[20] Minicircuits, ZFL-500LN

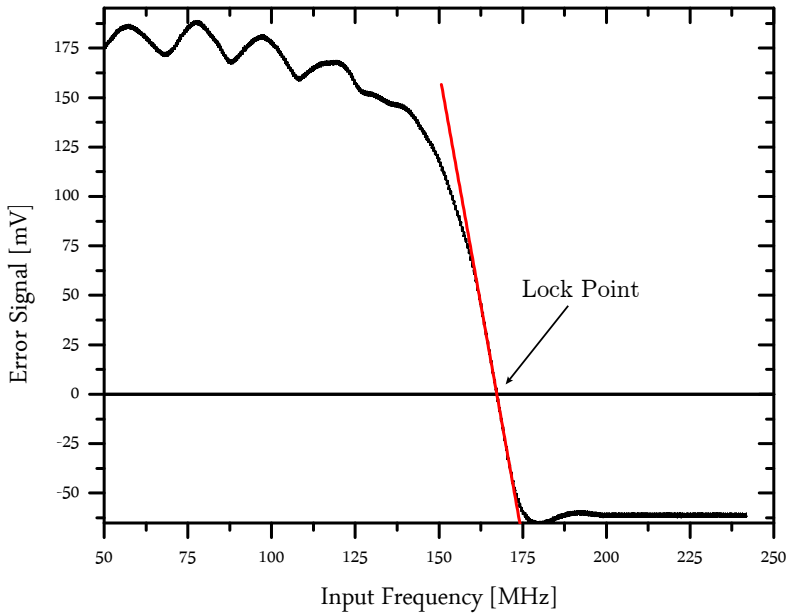

Figure 3.14: Characterization of the offset locking electronics. The slope of the error signal around zero is $(9.48 \pm 0.01)\,\mathrm{mV/MHz}$.

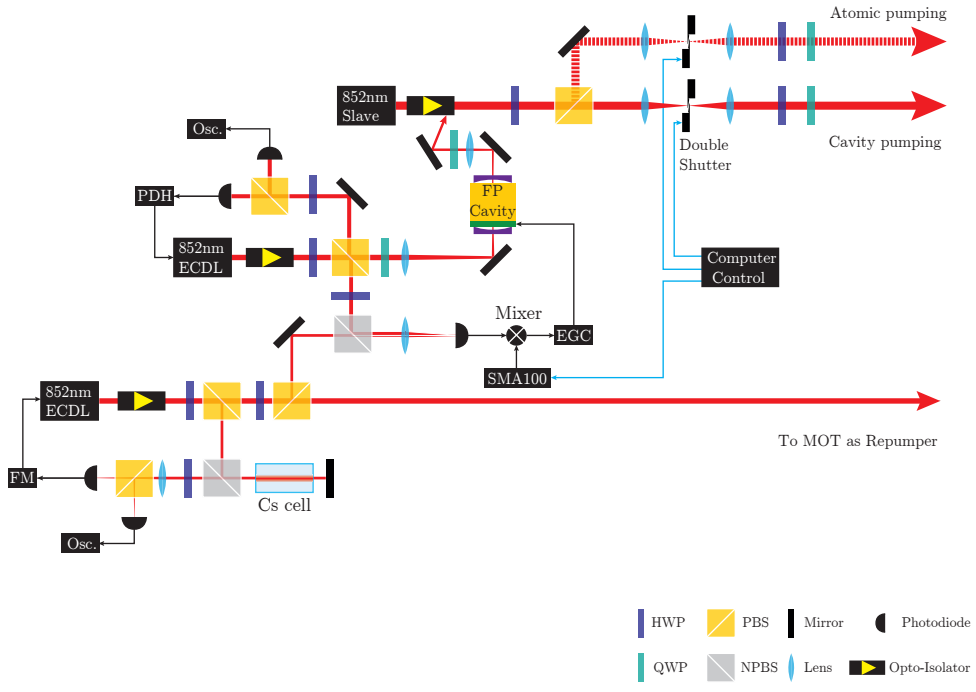

Figure 3.15: The cavity probe laser setup as explained in the text.

onto another cavity via a PDH stabilization. This cavity serves three purposes: firstly, it adds passive stability to the cavity master laser; secondly it is suppossed to narrow the linewidth via fast electronic feedback; and finally it acts as a frequency filter, when used in transmission, and therefore reduces the modulation side-bands.

Stabilization cavity The stabilization cavity spacer is shown in figure 3.16. It was designed with a square section ($4 \times 4\,\mathrm{cm}^2$), so as to be easy to manufacture and to mount. It has a central hole of 10 mm diameter for the optical path. The cavity is composed of two mirrors, a piezo and a Zerodur[21] spacer. Both mirrors are low loss mirrors from Layertec and the transmission of each mirror is specified to be 0.1%. Within the given boundaries of cavity stability the curvature of the mirrors is unimportant. One mirror is plane and the other one has a curvature radius of 1.5 m[22]. The cavity length is 5 cm and the piezo is 3 mm thick. The ring piezo[23] to control the cavity's eigen frequency has an inner diameter of 8 mm and an outer diameter of 13 mm. It is glued with Torrseal[24]concentric to the bore on one face of the cavity. Its maximum length change is supposed to be 3 μm. The 1/2" mirror is glued on the piezo and the 1" mirror is glued on the other face of the cavity. A FSR of (2822 ± 4) MHz and linewidth of (2.26 ± 0.02) MHz results in a finesse of $F = (1248 \pm 11)$. For thermal stability the cavity spacer is enclosed in a 1 cm thick perspex housing, sitting in a massive aluminium mount manufactured at the UCL workshop (shown in figure 3.17). For reduced

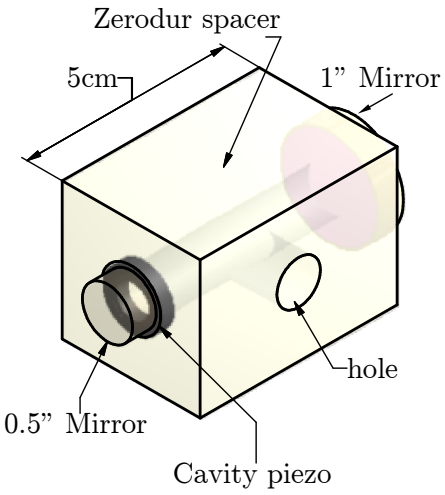

Figure 3.16: The schematic of the stabilization cavity and its spacer.

[21] Zerodur (Schott) is glass with a coefficient of thermal expansion (CTE) below $0.1 \cdot 10^{-6} 1/\mathrm{K}$

[22] Layertec, Laser Mirror, coating batch: G0405031

[23] Piezo HPSt 150/15-8/3, Piezomechanik GmbH

[24] Torrseal, rigid epoxy resin, Varian

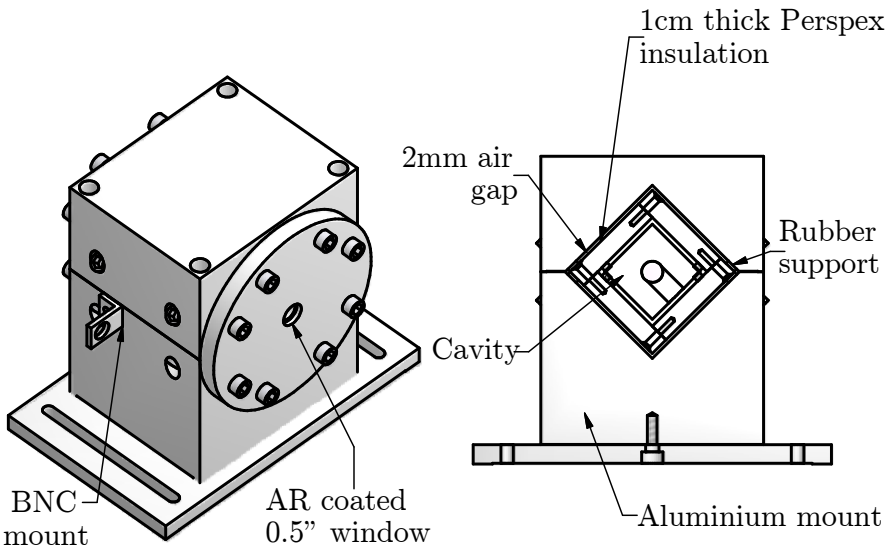

Figure 3.17: The mount of the stabilization cavity.

susceptibility to acoustic noise, the cavity spacer is mounted in the plane of the cavity mode [71].

Linewidth reduction with PDH To reduce the linewidth of the laser, the PDH error signal was fed back to the modulation input of the current driver of the cavity probe master, and directly onto the laser diode [70]. An estimate for the linewidth of the laser could be derived from a noise analysis of the error signal during lock and turned out to be (24 ± 2) kHz in 6 ms. The frequency noise added by the cavity cannot be seen this way. For a more rigorous analysis of the laser linewidth another similar laser [97] or a very long fibre [94] would have been necessary. But since the laser linewidth is not a crucial figure for the experiment, we refrained from spending more time on better measurements.
Most of the master laser light is used to generate a big error signal and to get as much cavity transmission as possible. The transmission is then used and fed into a slave laser. This has several intuitive advantages: first, frequency oscillations of the laser beam are converted into amplitude fluctuations in the transmission due to the response function of the cavity; the nonlinear response of the slave to the injection light intensity flattens those. Second: the "stabilization bumps" in the frequency profile of the laser, visible in the reflected light, are reduced due to the

frequency filtering property of the cavity. Third, the amount of light power is much bigger; the injected slave emitts up to 70 mW laser power for the experiment.
The light not needed for the slave injection is used to make the frequency of the cavity master laser controllable. It implements a similar setup as used for the cavity stabilization system. Light from the repumper laser is taken as an atomic reference, and is overlapped with light from the cavity master laser. The schematic is, in general, very similar to the one used in the cavity setup, but since the ground state hyper-fine splitting of the Cs $6^2S_{1/2}$ is, with 9192 MHz, a much bigger offset than the maximum 1500 MHz of the cavity lock, the components for the side-of-filter offset lock are therefore slightly different. The photodiode amplifier[25], the mixer[26] and the function generator[27] need a bigger frequency range. The Bias-Tee[28] limits the maximum offset frequency to 12 GHz.

Intensity control and switching Atomic samples are in general very susceptible to very small intensities of incoming laser light. First the laser was switched with an AOM because of its capacity of very short switch times. But the leaked light in the off-state was already by far too big and affected the atoms. The second fast method was switching with a Pockel cell, but again too much light illuminated the sample when it should not. The solution was a combination of two mechanical shutters with computer-controlled delay synchronization. The shutter construction is displayed in figure 3.18. One shutter is responsible for switching on, and the other one for switching off. For best performance, the shutter block is mounted on a translation stage and moved into the focus of the laser beam. The individual delays were measured and implemented into the computer control program. The rigid design guarantees little fluctuation in the delay times. In total, four mechanical shutters are used to switch two laser beams: the cavity probe and a beam to probe the atomic sample perpendicular to the cavity axis. But since quick intensity control, fast switching and rapid frequency sweeps were important as well, an AOM was added again into the beam-path. The switch time with the AOM

[25] Minicircuits ZVA-183+
[26] Minicircuits, ZX05-153+
[27] Rohde & Schwartz SMF 100A
[28] Minicircuits ZX85-12G-S+

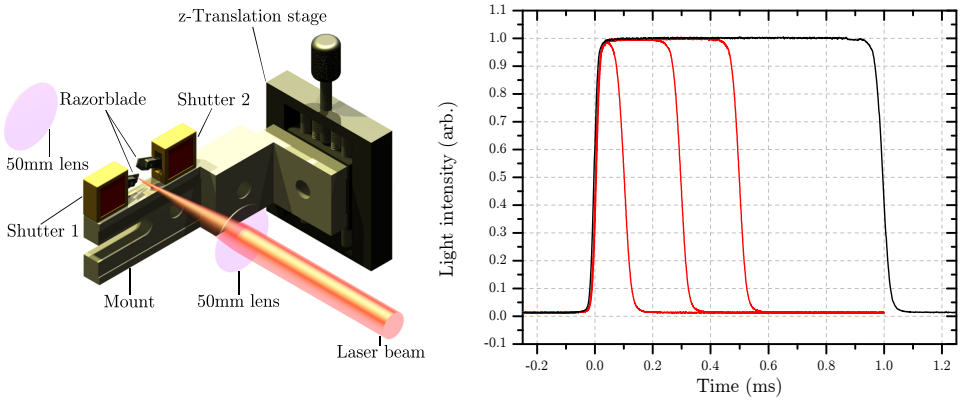

Figure 3.18: The performance of the double shutter
Left: Mechanical double shutter. Positioned in the focus of the laser beam is this shutter capable of producing light pulses of below 100 μs duration. This would not have been possible since the delay of each shutter alone would have been far too big.
Right: The intensity measured while switching. The 4 curves are for 1 ms (black), 500 μs, 300 μs and 100 μs (all red). The switch on duration from 10%-90% is (28 ± 4) μs and for the switch off (53 ± 4) μs. The temporal reproduction accuracy is ± 4 μs.

was measured to be below 1 μs.

System performance For the documentation of the system performance, figure 3.19 shows a slow computer controlled scan over the cavity resonance with the cavity probe laser system. The whole scan took 50 s and all the systems were locked. The cavity probe laser was then scanned in step jumps of 500 kHz every 2.5 s over the cavity resonance, and the transmission was recorded. Apart from the spikes due to the sudden change in locking point of the cavity probe laser, what is clearly visible is that over the whole time the relative frequency drift of the two locking systems is certainly much smaller than the step size of 500 kHz, therefore much smaller than the cavity linewidth of 1.6 MHz. This makes it suitable for our applications.

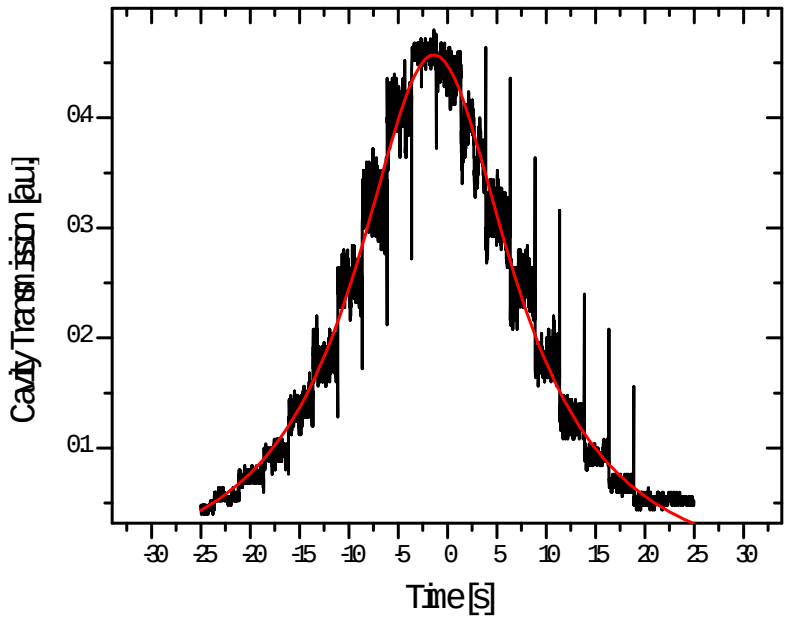

Figure 3.19: A slow scan over the cavity resonance

3.6 Summary

The experimental apparatus built for this part of the thesis was described. The main component, the nearly confocal cavity, was presented and characterized. The relevant cavity parameter can be found below:

Stabilization Cavity		
FSR	(2822 ± 4)	MHz
w	(2.26 ± 0.02)	MHz
F	(1248 ± 11)	
Science Cavity		
FSR	(1249.5 ± 0.4)	MHz
L	(119.96 ± 0.03)	mm
w_0	(127.57 ± 0.02)	μm
V_{00}	(1.533 ± 0.001)	mm^3
$g_{00}/(2\pi)$	(118.94 ± 0.02)	kHz
ΔL_{Max}	(18.5 ± 0.4)	μm
$w = \kappa/\pi$	(1.603 ± 0.003)	MHz
F	(780 ± 2)	
Deviation from confocality		
$\epsilon_{LA\,1}$	(21.9 ± 1.4)	μm
$\epsilon_{LA\,2}$	(5.8 ± 0.7)	μm
$\epsilon_{SA\,1}$	(94 ± 3)	μm
$\epsilon_{SA\,2}$	(76 ± 4)	μm
Corresponding mode density		
$\epsilon_{LA\,1}$	$\Rightarrow 11$	$\frac{\text{Modes}}{w}$
$\epsilon_{LA\,2}$	$\Rightarrow 41$	$\frac{\text{Modes}}{w}$
$\epsilon_{SA\,1}$	$\Rightarrow 2$	$\frac{\text{Modes}}{w}$
$\epsilon_{SA\,2}$	$\Rightarrow 3$	$\frac{\text{Modes}}{w}$

Table 3.1: Summary of the key cavity parameter.

Chapter 4

Observation of normal mode splitting

The experimental results of this chapter have been published in [104]: A. Wickenbrock, P. Phoonthong and F. Renzoni. *Collective strong coupling in a lossy optical cavity.* Journal of Modern Optics, 58(15), 1310-1316, 2011

In this chapter we report on experiments conducted on the previously described machine. The interaction of a cold cloud of ^{133}Cs atoms with the nearly confocal cavity is documented. Normal mode splitting as the hallmark of the collective strong coupling regime is observed as well as the corresponding avoided crossing and the dependence of the coupling constant g on the dipole matrix element of the optical transition. The collective normal mode splitting has been observed several times in different experimental settings over the last 20 years. While first experiments used an atomic beam of ^{133}Cs in 1989 [80], modern examples implement either ultra-cold atoms in the form of a Bose Einstein Condensate [9] or cold atoms from a magneto-optical trap [95]. The difference of our experiments is twofold: firstly the single atom parameters of this machine are deeply in the bad cavity limit. The relevant frequencies are determined to be $(g, \kappa, \gamma) = 2\pi \times (0.12, 0.8, 2.6) \times 10^6 \frac{1}{s}$. Only the large number of atoms loaded into the mode lift the system into the strong coupling regime. Secondly, this is the first observation of normal-mode splitting in a nearly confocal multimode cavity, which we will investigate further

in the following chapter. To compare the setup to other experiments, we define here the *collective cooperativity parameter*, which is the ratio of the collective coupling constant Ng^2 to the decoherence rates κ and γ:

$$C_{coll} = \frac{Ng^2}{2\kappa\gamma}, \tag{4.1}$$

with γ being the free space polarization decay rate defined as half of the excited state decay rate Γ. Collective cooperativity parameters bigger than unity indicate the strong coupling regime, which is a necessary condition for cavity cooling of multi-level atoms or molecules [55] but also interesting for other collective effects such as self-organisation and superradiance [21]. We show that in our system up to $(1.33 \pm 0.08) \times 10^5$ atoms are effectively coupled to the resonator resulting in a collective cooperativity of $C_{coll} = (186 \pm 5)$.
Before the results are presented, the experimental methodology is explained.

4.1 Experimental Procedure

To observe the normal-mode splitting as a function of the available system parameter we loaded the magneto-optical trap directly into the center of the cavity mode. A schematic of the experiment can be seen in figure 4.1. For the first experimental sequence, to show the $\sqrt{N}$ dependence of the splitting, we varied the atom number by changing the loading time of the MOT. An experimental sequence can be seen in table 4.1. Since the vacuum-Rabi splitting is even visible while the MOT is switched on, the cavities resonance frequency was aligned with the probe scanning until the two peaks had the same height. Then the cavity stabilization was activated, keeping the cavity resonance at the same frequency during the whole experiment. If the first measurement of the normal mode splitting showed two asymmetric peaks, the radio frequency offset of the locking was adjusted accordingly until both normal modes had the same transmission intensity. Two different ways of measuring the cavity transmission were implemented. The first involved, loading the MOT for an arbitrary time, then switching all the MOT beams and magnetic fields off. After a delay of 250 μs the shutter for the stabilized cavity probe beam

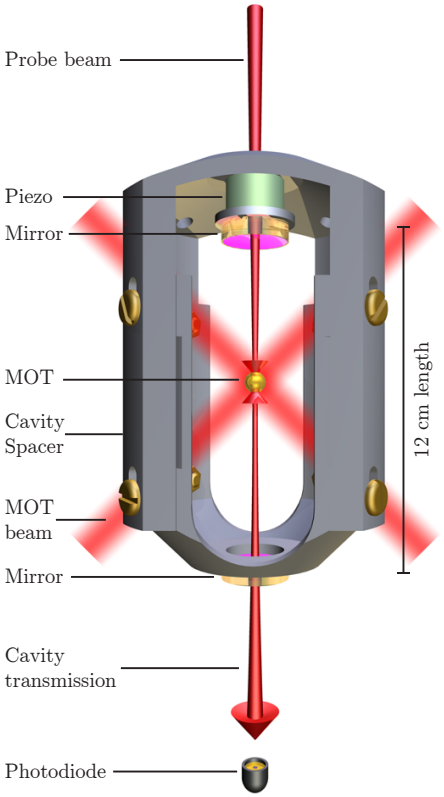

Figure 4.1: The experimental schematic for the normal mode splitting experiment. The figure shows the main ingredients for the observation of the cavity transmission. First, the magneto-optical trap (gold) is loaded into the cavity. The position of two pairs of MOT beams is indicated, while the 3rd pair is orthogonal to the image plane. For better visiblity the magnetic coil cage is omitted. The number of atoms in the mode is varied by changing the loading time of the MOT. For different detunings, a weak probe beam, mode matched for optimum coupling into the TEM_{00} interrogates the cavity-atom system and the cavity transmission is measured with a photodiode, averaged and recorded onto hard disc. The data were aquired via a DAQ-USB card.

was opened for 2ms and the cavity-atom system exposed to a weak σ_+ polarized laser beam, mode matched to the TEM_{00}-mode. The transmitted power through the cavity was measured to be below $(2.0 \pm 0.2)\,\mathrm{nW}$, which is for all the atom numbers involved much smaller than the critical photon number to cause bistable behaviour according to [34]. During the exposure the cloud of cold atoms was beginning to expand ballistically and fall due to gravity. But for temperatures of around $50\,\mu\mathrm{K}$ (well below the ^{133}Cs Doppler limit) during this time the MOT could be considered static. The effect of moving atoms onto the normal mode splitting is a modified coupling constant, averaged over one wavelength of the optical lattice in the cavity [54]. The transmission data were then aquired by integrating the photodiode signal over 1 ms in the middle of the complete exposure time to make sure not to observe any switching effects. Before the cycle started again, the cavity probe laser lock was changed via the function generator.

The second method involved positioning the probe laser slightly below the low energy normal mode peak and then, after releasing the MOT, to scan over the whole feature in about 2 ms. For this to work, the lock

needed to be open, an additional ramp signal to be applied and the system to be relocked. The ramp start was triggered with the same signal as the opening shutter of the probe beam in table 4.1. The data aquisition this way was much faster than with the previous method but it came with the cost that both peaks were scanned at slightly different times. Especially for low atom numbers and relatively high beam intensities this caused an asymmetry in frequency, height and width of the second peak with respect to the first peak even when the cavity resonance frequency matched the atomic transition. So this method was used only to document the avoided crossing and to compare the normal mode splitting of different hyperfine transitions, where the atom number was fixed and the beam power adjusted accordingly to avoid this effect.

Experimental Sequence	MOT Loading	Delay	Probe On	DAQ	Probe Off	Image	Delay	R&S Trigger
Time [ms]	100-3000	0.25	0.5	1	0.5	2.2	0.3	250
MOT shutter								
MOT switch								
B-field MOT								
Probe shutter								
DAQ trigger								
R&S trigger								
Camera trigger								

Table 4.1: The experimental control sequence for the normal mode splitting experiment. The columns from left to right represent the timestamp as they are written into the computer control cards. All displayed channels are digital, where green indicates the ON state and grey the OFF state.

4.2 Normal mode splitting in a nearly confocal cavity

Figure 4.2 shows the results for the first experimental run. Clearly visible is the splitting of the cavity resonance when atoms are introduced into the system. For each loading time the probe laser was scanned from $-2\pi \times 50\,\mathrm{MHz}$ to $2\pi \times 50\,\mathrm{MHz}$ in steps of $2\pi \times 2\,\mathrm{MHz}$ with respect to the empty cavity resonance by changing the radio frequency controlled

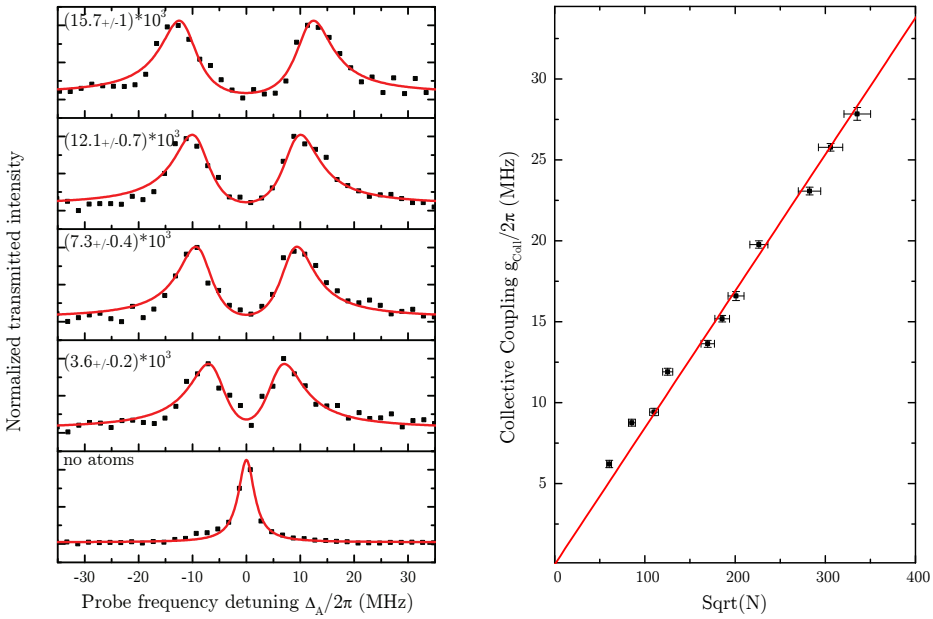

Figure 4.2: Evidence of strong collective coupling.
Left: The transmission data as a function of the probe frequency with respect to cavity resonance for different atom numbers. The data were fitted according to equation (2.11)
Right: Summary of the collective coupling parameter as a function of the atom number. The atom number was measured via fluorescence imaging for each experimental run with a different MOT loading time. The x-axis was then recalibrated so that the slope corresponds to the single mode coupling constant $g/2^{1/2}$. The slighty smaller coupling is because the atoms were free to move while being probed according to [54].

cavity lock after each cycle. Once the data were aquired the atom number was measured by taking a fluorescence image without changing any other system parameter. The transmission data were then fitted with the cavity-atom transmission function from equation (2.11). The free fitting parameters were κ, ω_0 and Ng^2 (and amplitude and offset).
The fit results for the collective coupling parameter were then displayed over the square root of the measured atom number (where we assumed a shot-to-shot error in atom number of 6%). As expected the collective coupling proved to be linear with $\sqrt{N}$. The resulting data were then fitted with a straight line and the atom number recalibrated to ensure a slope equal to $g/2^{1/2}$. The factor to rescale the atom number to match the theoretical coupling constant was 1.47 and could be attributed to the effect, that not all MOT atoms were in the center of the mode where

the coupling is strongest. The fit result for the cavity loss rate κ was $\kappa_{fit} = 2\pi \times (5.8 \pm 0.2)\,\mathrm{MHz}$ which is about 7 times more than measured with the empty cavity. That the transmission peaks appear broader in figure 4.2 is in agreement with the theory, which predicts a linewidth averaging effect (experimentally observed several times, first in [80] and more recently in [95]). It is just the magnitude of the increase which is unexpected. Initially we attributed this fact to the multi-mode character of the near confocal resonator, which we come back to in the next chapter.

The largest collective coupling constant we observed in the conducted experiments was $\sqrt{N}g = (27.8 \pm 0.4)$ MHz which corresponds to an effective number of $(1.33 \pm 0.08) \times 10^5$ atoms coupled to the TEM_{00} mode with effective coupling constant $g/2^{1/2}$. While with this atom number the maximum collective cooperativity was above $C_{coll} > 180$ the atom number corresponding to $C_{coll} = 1$ is just 600 indicating the border to the strong coupling regime.

4.2.1 Avoided crossing

A second set of data involved data aquisition method two. For different cavity frequencies with respect to atomic transition the normal mode splitting was recorded with a quick scan of the cavity probe laser over the normal-mode splitting double feature. If the cavity resonance was far away from the atomic transition the atoms have little effect on the cavity resonance. Just when the cavity resonance is close to the transition frequency the normal mode splitting gets observable. The mixing angle of the new dressed states depends inversly proportional to the detuning. For large detunings the dressed state of the cavity-atom system have just a small atomic component so that the nearly pure cavity resonance can be observed. The atom number for this experiment was kept constant for all different cavity-atom detunings and the scan speed after the release of the MOT was measured to be $2\pi \times 40\,\mathrm{MHz\,ms^{-1}}$. For each detuning 20 traces were averaged and a selection of the results are displayed in figure 4.3 on the left and the whole summary on the right.

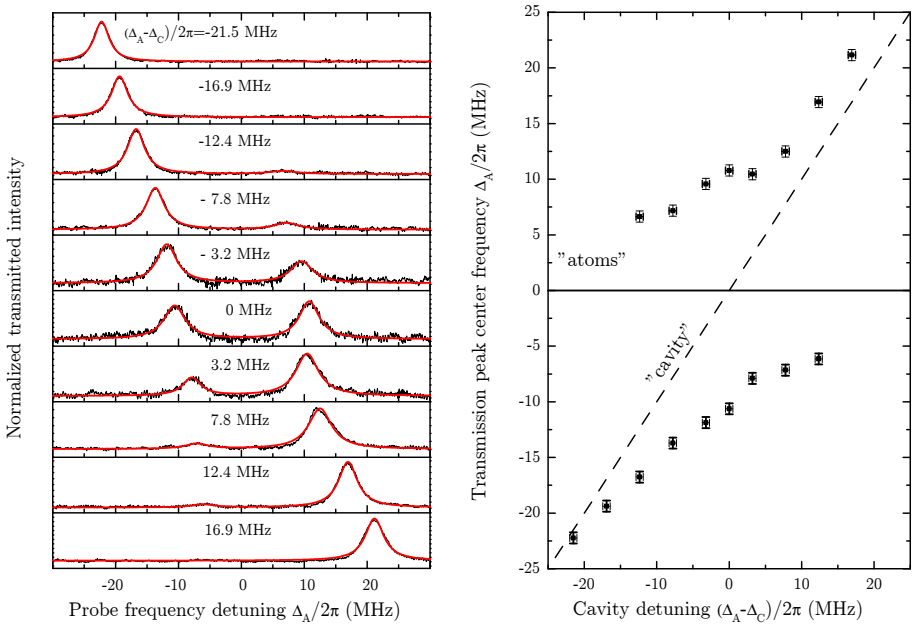

Figure 4.3: The avoided crossing of the cavity-atom system.
Left: The transmission data for different cavity-atom detunings $\Delta_A - \Delta_C = \omega_C - \omega_A$ during a quick scan after MOT release. The x-axis was calibrated with the empty cavity at different frequencies and the data then fitted with a double lorenzian.
Right: Summary of the avoided crossing. The center frequencies for both peaks are displayed over the cavity-atom detuning. The effective atom number for the whole experiment was kept fixed at $N_{eff} = (16.8 \pm 1.0) \times 10^3$. The error in cavity resonance alignment was estimated to be below $2\pi \times 0.3\,\mathrm{MHz}$. Without atoms, the bare state of the cavity should follow the dashed line. The horizontal line indicates the atomic transition frequency. Introducing atoms to the cavity splits the resonance according to the new dressed state basis and the avoided crossing gets observable.

4.2.2 Scaling with the relative transition strength

The last set of data shows in a convincing way the scaling of the normal mode splitting with the relative transition dipole element of the different hyperfine levels of the ^{133}Cs. For an effective atom number of $N_{eff} = (9.4 \pm 0.5) \times 10^3$ the cavity resonance was first moved on resonance to the $4 - 5$ transition. Again, 20 traces were averaged with the same scan speed as mentioned before. Then, the cavity was shifted by 252 Mhz to the red to be on resonance to the $4 - 4$ transition. To avoid populating dark states the polarization of the probe laser beam was made linear and with the same atom number the normal mode splitting was recorded.

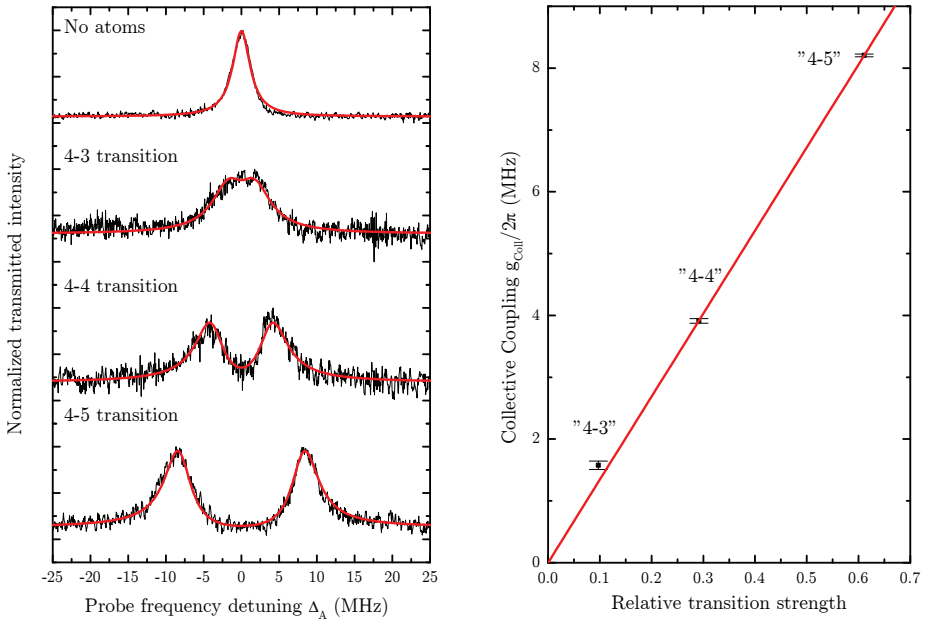

Figure 4.4: The normal mode splitting for different hyperfine transitions. **Left:** For the same effective atom number of $N_{eff} = (16.8 \pm 1.0) \times 10^3$ the normal mode splitting was recorded with a quick scan over the double feature for all the different available hyperfine transitions of the ^{133}Cs $6S^2_{1/2}F = 4 \rightarrow 6P^2_{3/2}F = 3, 4, 5$. The data were fitted with the transmission function of a cavity containing atoms (2.11) with the coupling constant as a free parameter.
Right: The different measured coupling for each hyperfine transition is displayed over the relative dipole matrix element taken from [87]. According to the definition of the coupling constant the dependence should be linear.

For the last excited hyperfine transition with the weakest relative dipole matrix element the cavity was shifted on resonance to the $4-3$ transition. All traces are displayed in figure 4.4 on the left. The data were then fitted with the cavity transmission function (2.11) with the collective coupling constant as a free parameter. On the right of figure 4.4 the fit results are displayed over the relative dipole matrix element taken from [87]. Even though it is just a very simple model, which doesn't take into account optical pumping or the different initial magnetic sublevel populations, the collective coupling constant appears to be linear in the relative dipole transition strength as indicated by the definition of the coupling constant g (2.2).

4.3 Summary

This chapter presented a selection of experiments in the collective strong coupling regime. Up to $(1.33 \pm 0.08) \times 10^5$ ^{133}Cs atoms were effectively coupled to the TEM_{00} mode of a nearly confocal resonator where the coherent dynamics of a single atom is dominated by the incoherent loss rates κ and γ. As predicted the collective coupling scales linearly with $\sqrt{N}$ as well as with the relative dipole matrix element. And our system reaches the strong coupling regime for atom number as low as 600. Increasing the number of particles within the mode enables us to reach collective cooperativities of up to $C_{coll} = (186 \pm 5)$. A regime where the coherent interaction between the collective atomic mode and the multi-mode field of the resonator is dominant over cavity decay and polarization decay rate. The system is therefore suitable to study other collective effects such as collective self-organizations and superradiance [21]. But before we were going to do that, we were interested in the multi-mode component, which we ignored so far. The system seems to be fairly well described by an effective single mode, the only hint that there is more to the multi-mode field in the resonator is the slightly too big cavity loss rate as derived from fitting the transmission data with the cavity transmission function (2.11) and leaving the cavity loss rate as a free parameter. The derived κ_{fit} is about 7 times larger than the measured TEM_{00} κ which was determined by cavity linewidth measurements to be $2\pi \times 0.8\,\mathrm{MHz}$.

Chapter 5

Collective strong coupling in multi-mode cavity quantum electrodynamic

Parts of the experimental results of this chapter are submitted for publication: A. Wickenbrock, M. Hemmerling, G. Robb, C. Emary, and F. Renzoni. *Collective strong coupling in multi-mode cavity QED.* 2012

This chapter presents experimental results investigating the collective strong coupling regime in the previously described apparatus. To gain understanding of the multi-mode dynamics in the coupled atom-cavity system we implemented an intensified CCD camera, borrowed from another experiment in our group [77], and repeated the transmission measurements of the previous chapter. The camera enabled us to observe a rich transverse mode spectrum of the nearly confocal resonator. Implementing a degenerate transverse mode cavity for cavity QED experiments seems at first sight counter-intuitive, since infinite degenerate vacuum modes are available in free space already. The result is well known and can be observed in any ^{133}Cs filled glass cell: spontaneous emission is an irreversible process. For this reason, most literature on the Jaynes- or Tavis-Cummings model is interested in single-mode interaction. Some exceptions are [2, 33, 50, 73, 85, 90, 108]. Most of those are restricted to a two-mode interaction. In [85] the atomic population inversion in a cavity with M modes is analyzed analytically. One result reveals that the M

modes can be represented by just one effective coupling constant g_{eff}:

$$g_{eff} = \sqrt{\sum_{i=1}^{M} g_i^2}. \tag{5.1}$$

So by increasing the number of available modes, the effective coupling constant should increase as well. This is used as an argument in favour of confocal cavities in [21, 101]. In this chapter we will present the first evidence for an increased effective coupling constant, which could be attributed to the presence of higher order transverse modes. A second interesting feature of the interaction with multiple modes concerns quantum computing: photons as qubits have a long and successful tradition, they have great coherence properties but are hard to store. Cavities can serve several different purposes in this context (e.g. [74, 96, 98]). Atoms in multi-mode cavities could be used, for example, as nodes in a quantum computing network, since the atom would be able to coherently exchange photons as qubits with spatially different transverse modes, which could be addressed with different laser beams. In this chapter we show, how the atoms in our setup redistribute photons from the TEM_{00} mode to higher-order modes.

The chapter is organized as follows: first, the use of a multi-mode cavity is motivated by simulating the master equation for a simple multi-mode system. These simulations were conducted by Dr. Michal Hemmerling from the University of Strathclyde, Glasgow. Then the changes to the experimental setup and the methodology are explained before the experimental results are presented. The chapter ends with a short summary.

5.1 Multi-mode, multi-atom Jaynes-Cummings model

To get an idea of the behaviour of a small number of atoms in a multi-mode field, the Jaynes-Cummings-Hamiltonian needs to be extended. The extension from the single-mode, single-atom Hamiltonian (2.1) is straight forward: in a frame, rotating with the pump frequency ω_P, the

N-atom, M-mode Hamiltonian can be written as [21]:

$$\begin{aligned} H = \sum_{a=1}^{N} -\hbar\Delta_A \sigma_a^z + \sum_{n=1}^{M} -\hbar\Delta_C a_n^\dagger a_n - i\hbar\eta_n \left(a_n - a_n^\dagger\right) \\ -i\hbar \sum_{a=1}^{N}\sum_{n=1}^{M} \left(g_n\left(\hat{\mathbf{x}}_a\right)\sigma_a^+ a_n + g_n^*\left(\hat{\mathbf{x}}_a\right)\sigma_a^- a_n^\dagger\right). \end{aligned} \tag{5.2}$$

Here, $\Delta_C = (\omega_P - \omega_C)$ is the pump-cavity detuning and $\Delta_A = (\omega_P - \omega_A)$ the pump-atom detuning, and η_n is the pumping rate of mode n. The first row describes the energy in the modes and the atoms and the second row represents the interaction term. Adding more atoms and modes also affects the environmental decoherence properties. The Liouville term is changed according to:

$$\begin{aligned} \mathcal{L}\rho = \sum_{n=1}^{M} \kappa_n \left(2a_n \rho a_n^\dagger - a_n^+ a_n \rho \right. \\ \left. - \rho a_n^\dagger a_n + \gamma \sum_{a=1}^{N} \left(2\sigma_a^- \rho \sigma_a^+ - \sigma_a^+ \sigma_a^- \rho - \rho \sigma_a^+ \sigma_a^-\right), \right. \end{aligned} \tag{5.3}$$

where κ_n is the cavity loss rate of mode n. The first row can be attributed to incoherent decay of the cavity modes, while the second row describes the relaxation of the excited state of the atoms. The kinetic energy and the position-dependence of the incoherent scattering rate, as well as the spatial distribution of the emitted photons, have been omitted. In this simple model we just consider well localized atoms without momentum.

The evolution of a system containing 2 atoms strongly coupled to 3 modes $(1, 2, 3)$ can be seen in figure 5.1.
The parameters are:

$$\begin{aligned} (g_1, g_2, g_3) &= (2, 1, 0.5)\,\kappa, \\ (\kappa_a, \kappa_b, \kappa_c) &= \kappa, \\ (\eta_2, \eta_3) &= 0, \\ \eta_1 &= 10^{-3}\kappa, \\ \gamma &= 0.2\kappa. \end{aligned} \tag{5.4}$$

So, technically the coupling to mode 3 is not "strong" since $\kappa_3 > g_3$, but nevertheless a frequency scan of the coupled system, as seen in the

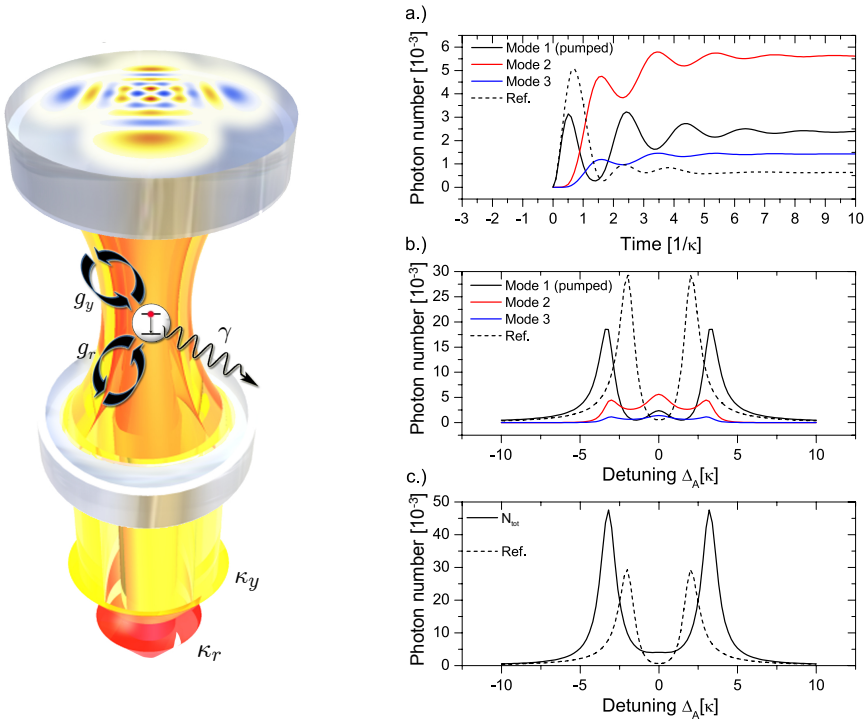

Figure 5.1: A simplified model of the multi-mode, multi-atom interaction. **Left**: A schematic describing the system. A 2-level atom inside a cavity with two transverse modes interacts with both of them with rate g_r (red mode) and g_y (yellow mode). Decoherence is due to spontaneous emission into the environment with rate γ, and cavity loss of each mode with rates κ_r and κ_y respectively. The cavity loss allows us to observe the cavity transmission, which can be a superposition of both modes.
Right: Results of numerical simulations of the master equation for two atoms interacting with three cavity modes. The top panel a) presents the evolution of the photon number expectation value of each mode seperately, while mode 1 is being pumped for $\Delta_C = 0$. Photons are redistributed to other modes via interaction with the atoms. Panel b) shows the steady state value of the photon number as a function of the pump detuning Δ_C for each mode, while c) shows the coherent superposition of the three mode's steady-state photon number. The normal mode splitting is larger according to the effective coupling constant g_{eff}. As a reference, the respective single-mode, single-atom evolution is given for mode 1.

bottom panel in 5.1 reveals the normal mode splitting in cavity photon number with effective coupling constant g_{eff}.
The panel shows the expectation value of the $\left(a_1^+ + a_2^+ + a_3^+\right)(a_1 + a_2 + a_3)$ operator. The mode resolved photon number can be seen in the middle panel, while the top panel shows the evolution of the expectation value of the 3 modes over time for $\Delta_C = 0$. As a reference, the single-atom, single mode behaviour is given in each panel as well. The parameters are the same as for mode 1. The increase in the normal mode splitting

is clearly visible; the two maximum transmission peaks are separated by exactly $2g_{eff}$. What can also be seen is that even though only mode 1 is being pumped, the excitation gets distributed into the other modes as well.

5.2 The effective number of atoms

Getting a good estimate of the atom number in the mode is crucial for understanding the system's dynamics and in evaluating its characteristics. Also, since it is a multi-mode cavity, the different coupling constants g_{nm} for each TEM_{nm} have to be calculated. As stated in the introduction, the position-dependent coupling constant g_{00} in the single-mode case equals:

$$g_{00}(\vec{x}) = \sqrt{\frac{\mu^2\omega_C}{2\hbar\epsilon_0 V_{00}}} u_{00}(\vec{x}) \,. \tag{5.5}$$

Where μ is the dipole matrix element of the electronic transition, ω_C is the cavity's resonance frequency, V_{00} is the mode volume of the fundamental mode and $u_{00}(\vec{x})$ is the mode function of the electric field.
The mode volume for the TEM_{00} mode is given by the integral over the expectation value of the mode:

$$\begin{aligned} V_{00} &= \int_V u_{00}(\vec{x})^* \, u_{00}(\vec{x}) \, dV \\ &= \frac{\pi w_0^2}{2} \frac{L}{2} \end{aligned} \tag{5.6}$$

This relationship needs to be generalized for the case of higher order transverse modes. The higher-order mode function for the electric field at the beam waist can be written with the aforementioned (1.23) complete set of Hermite-Gaussian polynomials, replacing the *Gouy phase* and *beamfront curvature* by a plane wave term: $\sin(kz)$, which is a good approximation when close to the centre of the beam:

$$u_{nm}(\vec{x}) = \sqrt{\frac{1}{2^n n!}\frac{1}{2^m m!}} H_n\left(\sqrt{2}\frac{x}{w_0}\right) H_m\left(\sqrt{2}\frac{y}{w_0}\right) \exp -\frac{x^2+y^2}{w_0^2} \sin(kz) \,. \tag{5.7}$$

For the mode volume calculation the problem can be reduced to the two transverse dimensions at the centre of the beam in the z-direction since due to conservation of energy each z-plane has the same photon probability. The z-direction enters the mode volume via the factor $L/2$.
A generalized expression for the mode volume of the higher-order transverse modes is:

$$V_{nm} = \frac{1}{|u_{nm}(\vec{x})|^2_{max}} \int_V |u_{nm}(\vec{x})|^2 \, dV = \frac{V_{00}}{|u_{nm}(\vec{x})|^2_{max}}, \tag{5.8}$$

where the normalization factor ensures that the mode function has maximum value of 1. With this expression, the position dependent transverse coupling constant $g_{nm}(\vec{x})$ becomes:

$$g_{nm}(\vec{x}) = \sqrt{\frac{\mu^2 \omega_C}{2\hbar\epsilon_0 V_{nm}}} \frac{u_{nm}(\vec{x})}{|u_{nm}|_{max}}, \tag{5.9}$$

and this can be used to calculate the effective number of atoms in the TEM_{nm} mode:

$$N_{nm} = \frac{1}{|u_{nm}(\vec{x})|^2_{max}} \int |u_{nm}(\vec{x})|^2 \, \rho_{\mathrm{MOT}}(\vec{x}) \, dV. \tag{5.10}$$

So apart from knowing the precise shape of the mode function in question, a good estimate of the MOT's density function $\rho_{\mathrm{MOT}}(\vec{x})$ is crucial. For the experiment, we took fluorescence images with a calibrated camera and fitted a 2D Gaussian to the background-subtracted data. For small atom numbers, the atom distribution in a MOT can be well described by a 3D Gaussian density function. With a single fluorescence image just two dimensions are accessible. But since the shape of the magnetic field gradient is radially symmetric, so too should the MOT be. Therefore a single 2D image reveals all the information necessary to reconstruct the density function. The MOT fitting function used was:

$$\rho_{\mathrm{MOT}}(\vec{x}) = \rho_{max} e^{\frac{-1}{2}\left(\frac{x}{s_r}\right)^2} e^{\frac{-1}{2}\left(\frac{y}{s_r}\right)^2} e^{\frac{-1}{2}\left(\frac{z}{s_z}\right)^2} \tag{5.11}$$

where s_r and s_z are the radial and axial width respectively, and ρ_{max} is the peak density at the centre of the MOT as derived from the 2D image fit.

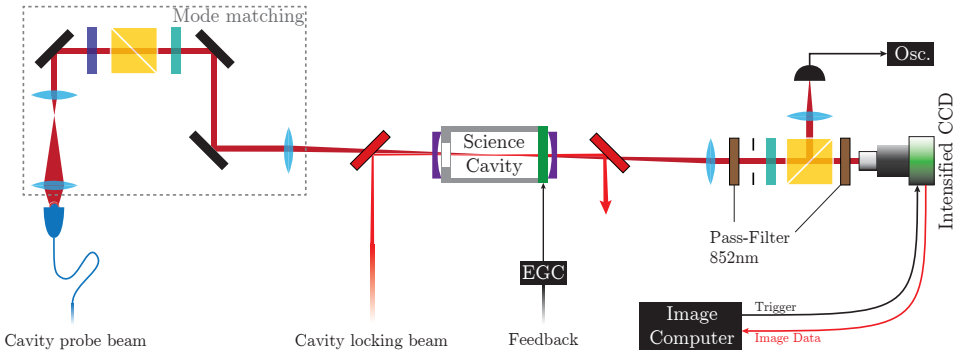

Figure 5.2: Changes made to the experimental setup described in chapter 4. Instead of just a photodiode, the transmission of the cavity is collected by an intensified CCD camera and a photodiode. A polarizing beam splitter cube and a quarterwave plate allow for polarization dependent analysis of the transmitted light.

5.3 Experimental procedure

The experimental procedure didn't change much compared to the last chapter. An additional trigger was introduced to drive the mechanical shutter of the intensified CCD camera. The timing of the camera shutter was not crucial since the exposure time was controlled with the laser beam. To investigate the normal mode splitting, the MOT was first positioned in the cavity centre. This was done by changing the magnetic field of the anti-Helmholtz coils and also an offset magnetic field with three pairs of compensation coils. During this process, the cavity frequency was locked at the atomic transition frequency so that a weak frequency scanning cavity probe laser showed the normal mode splitting in the transmission on the photodiode. The splitting was then maximized by moving the MOT in the mode. Three different sets of data were then taken, and in this thesis I report just on the first, since the data analysis for the other two is still on-going. The data sets differed in the coupling of the probe beam to higher-order modes. For the first set, the probe beam was mode-matched to couple most of the light into the TEM_{00} mode. To achieve this, all of the optical surfaces and all of the optical pathlengths of the incoupling optics were represented by a matrix M. Then the theoretically calculated cavity TEM_{00} mode was propagated out of the cavity to the incoupling lens, making sure, that the beam after the lens was collimated, and the beam waist was calculated. To match the TEM_{00} mode, the cavity probe beam coming from a fibre was adjusted in beam-size by

a telescope to match the calculated outgoing beam. Once that was done, the incoupling of the probe beam into the mode was maximized by coupling most of the light into the TEM_{00} subset of modes, or better, the difference between the two subsets was maximized. This is possible since the mode subset degenerate with the TEM_{01} mode has no on-axis component so, for a well aligned Gaussian beam, the mode overlap is reduced. To couple light efficiently into a specific mode of a confocal cavity is in fact harder than it sounds. Normally, mode matching is fairly straightforward: observing the transmission of a scanning laser reveals several transverse resonance peaks. Then, identifying the 00-mode with a camera and maximizing the transmission of the corresponding transmission peak, usually results in a good mode-matched laser beam. In a close to confocal cavity, nearly all incoupling alignments result in transmission peaks with the same frequency, so to couple light effectively into a single mode relies on thorough calculations of the accessible beam parameters and observation of the beam shape with the camera. Anything else other than a single Gaussian indicates higher-order mode components. For the first set of data, the relative weight of the TEM_{00} mode in the empty cavity transmission was $(98 \pm 1)\,\%$. The other two sets were a misaligned version of the mode-matched TEM_{00} beam and, in one experiment, with a collimated beam without mode-matching optics at all.

Like in the last chapter, for each set, a MOT was loaded into the cavity for a specific time, then the MOT light and the magnetic field were switched off and the compensation coils were switched from positioning the MOT to compensating for background magnetic fields. After a short delay time (for the fields to decay) the cloud of atoms was probed for 1.5ms with a weak *linearly polarized* probe beam, with frequency detuning Δ_C, and the transmission was recorded with the camera. For better signal-to-noise ratios, three images were averaged. This was repeated for several detunings over a range of $|\Delta_C/(2\pi)| = 100\,\mathrm{MHz}$ with step sizes of $\Delta_C/(2\pi) = 2\,\mathrm{MHz}$ for the cavity containing atoms and a stepsize of $0.25\,\mathrm{MHz}$ for the empty cavity. All the measurements were repeated twice, with alternating circular polarizations incident onto the camera. This was done to check for eventual polarization effects due to residual magnetic fields, which could not be observed. For the following analysis, both polarization data sets are combined. For each MOT load-

ing time, fluorescence images of the MOT were taken at the exact same time, whereas in the transmission experiment the MOT would have been probed. This way the MOT's density function, which was used in the analysis to calculate the effective atom number, was recorded as well. For each loading time, ten images were fitted with a 2D Gaussian revealing a spread of the MOT's maximum density of around 6%.

Transmission analysis The modal decomposition of several overlapped transverse cavity modes in the transmitted light with a single intensity image is impossible. For a true reconstruction of the different modal components more intensity data is needed [105]. But in our case the situation was simpler. Firstly, we were not interested in the phase information of the modes, instead we wanted to know the absolute higher-order components and secondly we were not working with an infinite set of modes, but rather a dramatically reduced set.
To get a good estimate of the modal components of the transmitted light, we fitted each image with the following intensity function:

$$I(x,y) = \left| \sum_{n,m=0}^{N,M} \alpha_{nm} u_{nm}(x,y) \right|^2 , \tag{5.12}$$

where α_{nm} is a complex fit parameter representing the weight of mode u_{nm} in the mixture. The data of a given image was first fitted with $N = M = 0$ and then the maximum mode indices were successively increased in the order of their coupling strength g_{nm}, taking into account the corresponding confocal subset of modes:

$$\begin{aligned}
I_1(x,y) &= |\alpha_{00} u_{00}(x,y)|^2 , \\
I_2(x,y) &= |\alpha_{00} u_{00}(x,y) + \alpha_{11} u_{11}(x,y)|^2 , \\
I_3(x,y) &= |\alpha_{00} u_{00}(x,y) + \alpha_{11} u_{11}(x,y) + \alpha_{02} u_{02}(x,y) + \alpha_{20} u_{20}(x,y)|^2 , \\
I_4(x,y) &= \cdots .
\end{aligned} \tag{5.13}$$

For each fitting, the R^2 value (coefficient of determination) was noted as a measure of the fit quality, and the series was omitted if adding more modes to the function did not improve the R^2 value measurably. The

resulting set of transverse modes used to fit each image was:
$(00, 11, 20, 02, 40, 04, 31, 13, 22, 60, 06)$.

5.4 Experimental results

An example of the data is shown in figure 5.4. On the left it shows the transmission as derived from adding up all the pixel values as a function of the probe laser detuning, for a MOT loading time of 1250 ms. This loading time corresponds to an effective atom number in the corresponding mode, as derived from equation (5.10), of:

nm	N_{eff}
00	$(84 \pm 5) \times 10^3$
11	$(126 \pm 8) \times 10^3$
20	$(127 \pm 8) \times 10^3$
02	$(149 \pm 9) \times 10^3$

This table, as most of the following analysis, is restricted to the four strongest modes in the cavity transmission. The mode volume of the TEM_{20} mode is twice as big as the mode volume of the TEM_{00}, therefore it contains more atoms, though not twice as much because the density of the MOT also follows a Gaussian distribution. The difference between the atom number in the TEM_{20} and the TEM_{02} modes even though their volume is the same, is due to the fact that the first mode index increases the mode size along the short-axis of the MOT. Along the radial direction (long axis), the magnetic field gradient is only half the gradient along the axis connecting both anti-Helmholtz coils (short axis), and the width of the Gaussian density profile is therefore bigger. The other MOT parameters for 1250 ms are: $(s_z, s_r) = (161 \pm 1, 255 \pm 6)$ μm and a peak density $\rho_{max} = (1.2 \pm 0.1) \times 10^{10}$ atoms/cm^3. On the left, the cavity transmission of the probe laser without atoms is shown in a similar way. Key images of the transmission are presented to emphasize the visibly different transmission features with and without atoms. An image reconstructed with the fit results is also shown next to each presented transmission picture.

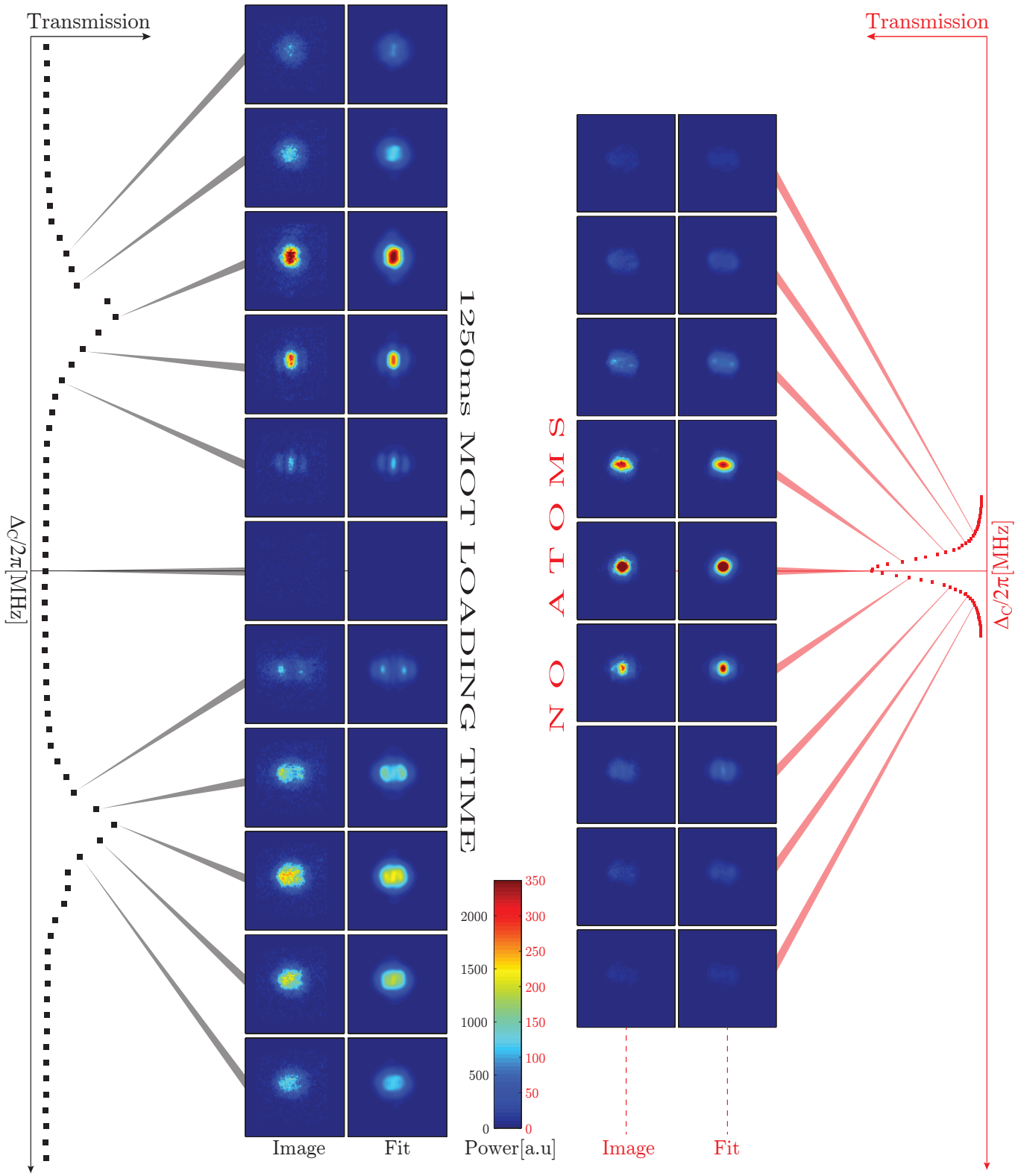

Figure 5.3: Mode-resolved normal mode splitting data example.
Left: The graph on the left shows the overall emitted power of each image as a function of the probe detuning for a cavity loading time of 1250 ms. The frequency difference per image is $\Delta_C/(2\pi) = 2\,\mathrm{MHz}$. Some key images are shown together with their fitted result counterparts.
Right: The graph shows the integrated transmission of the empty cavity. The stepsize is $\Delta_C/(2\pi) = 0.25\,\mathrm{MHz}$. Even though for different frequencies the shape deviates slightly from the Gaussian TEM_{00} profile, $|\alpha_{00}|^2$ dominates the distribution with a relative weight of more than 98%. The saturation visible in some of the images is artificial, since I wanted to show them all on the same colour scale.

5.4.1 Increased multi-mode coupling constant

All the mode components of the transmitted light displayed the normal mode splitting. To measure the coupling constant of the system, the corresponding mode-resolved image data was fitted with the transmission function of the coupled cavity-atom system (2.11). Fit parameters were the maximum cavity transmission T_0, cavity decay rate κ and the collective coupling constant g. For each loading time and each mode the effective atom number in the respective mode was calculated, and then the measured collective coupling constant was displayed against the square root of the effective atom number in the mode. The result for the strongest four modes can be seen in figure 5.4. From top to bottom the data including the transmission fit can be seen for: no atoms, 50 ms, 175 ms, 350 ms and 1500 ms loading time. The last row shows the derived collective coupling versus the square root of the atom number. The first 8 data points were then fitted with a straight line and the gradient of this line represents the single-mode single-atom coupling constant. The fitted gradient is displayed for each mode in figure 5.5. Together with the fit result, the theoretical calculations for different coupling constants are presented as well. We note here that the initial m_F-state distribution of the atomic sample is not spin-polarized. We therefore have a distribution of different m_F states, each one with a different dipole matrix element according to the Clebsch-Gordon coefficient of the transition. The previously derived coupling constant of $g_{00}/(2\pi) = (118.94 \pm 0.02)\,\mathrm{kHz}$ assumes the atom to be in the highest $m_F = 4$ state with a σ_+ polarized laser beam coupling it to the excited $m_F = 5$ state. Instead, in this experiment, the laser polarization was linear and the atoms were distributed over different m_F states. Optical pumping with linear polarized light results in a complex equilibrium population of each sublevel, with an accumulation of population close to $m_F = 0$ [87]. The average dipole moment is much smaller than it is for circular polarized light. The third theoretical value uses the average dipole matrix element for unpolarized light and a flat m_F state distribution. The results are also displayed in table 5.1. The theoretical values for the coupling constant dismiss any effect of the other modes and are, in all the cases, smaller than the measured single-atom, single-mode coupling constant. The most reasonable

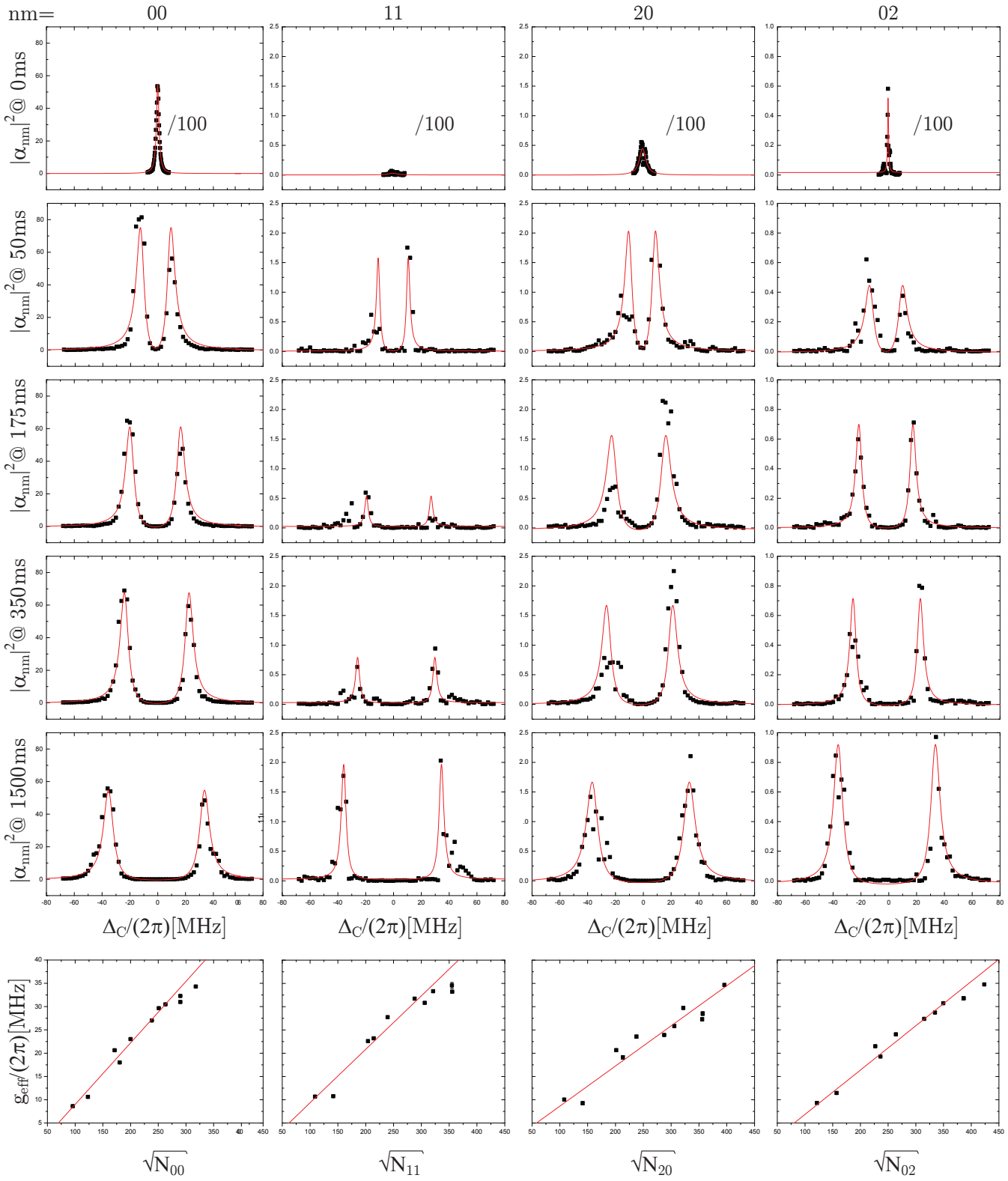

Figure 5.4: Mode-resolved normal mode splitting data.
From top to bottom the loading time increases: $(0, 50, 175, 350, 1500)$ ms loading time respectively. The data, derived from fitting the transmitted intensity with a 2D mode function as described in the text, is fitted with the transmission function eq. (2.11) and, without atoms, with a Lorentzian. The bottom row summarizes the data. The collective coupling for each mode is displayed versus $\sqrt{N}$ of the respective mode as derived from fluorescence images.

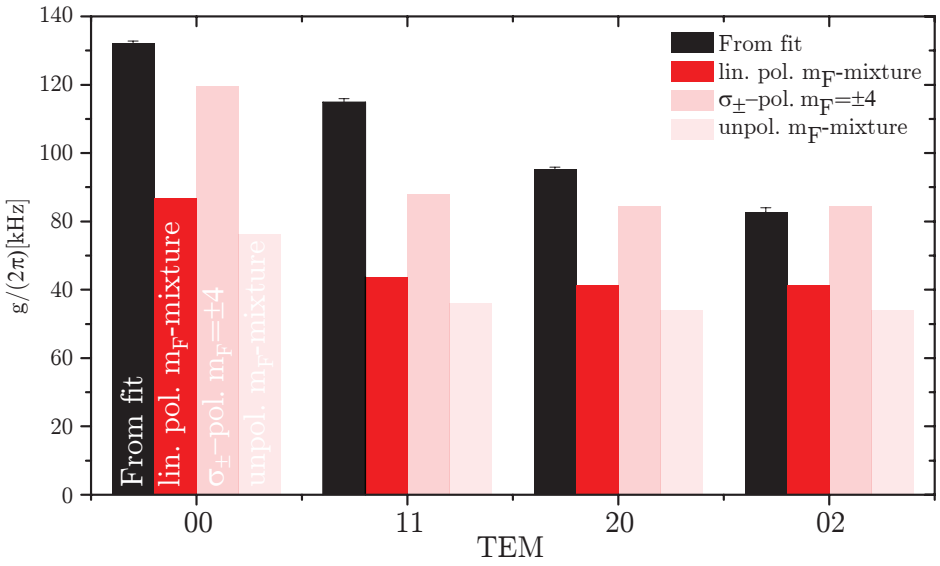

Figure 5.5: The coupling constants derived for each mode from fitting the mode decomposed transmission $|\alpha_{nm}|^2$ data versus $\sqrt{N_{nm}}$, in comparison with three theoretical values for g_{nm} neglecting any coupling between the modes.

value for the theoretical coupling constant is the linear polarized value, in which case the measured coupling constant is on average more than 50% bigger than the predicted one. This effect could be attributed to the presence of the nearly degenerate higher-order modes. To explain the observed increase of 80% in the coupling constant of the TEM_{11} at least the first six strongest coupled transverse modes need to contribute to the effective multi-mode coupling constant.

5.4.2 Atom mediated photon redistribution

A second observed effect concerns the mode composition of the light with and without atoms. During data acquisition, we observed that the shape of the transmitted light changed with and without atoms, and also differed for each peak of the normal mode splitting (as can be seen in figure 5.4). The modal decomposition of the transmission was helpful to gain insight into the photon redistribution effect due to the atoms. For this, the maximum value of the fitted transmission data was normalized

Mode	nm	00	11	20	02	
Mode volume	V_{nm}	1.52	2.81	3.04	3.04	mm^3
Measured:	$g_{meas}/(2\pi)$	(131 ± 1)	(115 ± 1)	(83 ± 1)	(95 ± 1)	kHz
Lin. pol.:	$g_{lin}/(2\pi)$	87	64	61	61	kHz
$\mu = 1.95 \times 10^{-29}$C/m						
Increase:	$g_{meas}/g_{lin} - 1$	(52 ± 1)	(80 ± 2)	(35 ± 2)	(55 ± 1)	%
σ_+ pol.:	$g_{\sigma_+}/(2\pi)$	119	88	84	84	kHz
$\mu = 2.69 \times 10^{-29}$C/m						
Iso. pol.:	$g_{iso}/(2\pi)$	76	56	54	54	kHz
$\mu = 1.76 \times 10^{-29}$C/m						

Table 5.1: Measured coupling constant versus theoretical predictions. Constants from [87]. The increased coupling with respect to the theoretical single mode values could be explained by the presence of degenerate higher order TEM modes. For comparison the other theoretical possible single mode values for different light polarizations and m_F-state distributions are given as well.

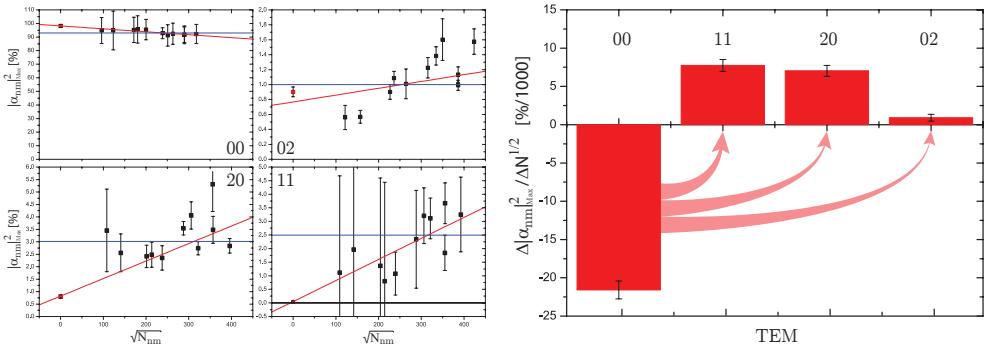

Figure 5.6: The effect of the atoms on the modal composition of the transmission.
Left: Normalized mode maximum $|\alpha_{nm}|^2$ as a function of $\sqrt{N_{nm}}$ for the four main modes. The zeroth order component decreases while the higher order components increase. The data was fitted with a straight line (red) and the weighted mean for all the datasets with atoms was computed (blue).
Right: The results of the straight line fit shows the decrease of the 00-mode and the increase of the other mode components. For 10^6 ($\sqrt{N_{00}} = 1000$) atoms in the mode, the linear fit reveals a decrease of more than 20%.

so that:

$$\sum_{n,m=0,0}^{Set} |\alpha_{nm}|^2_{max} = 1. \tag{5.14}$$

Then this data was displayed versus $\sqrt{N_{nm}}$, as derived from the images, and the result fitted with a straight line. The result is quite clear at least for the TEM_{00} mode: increasing the number of atoms in the mode

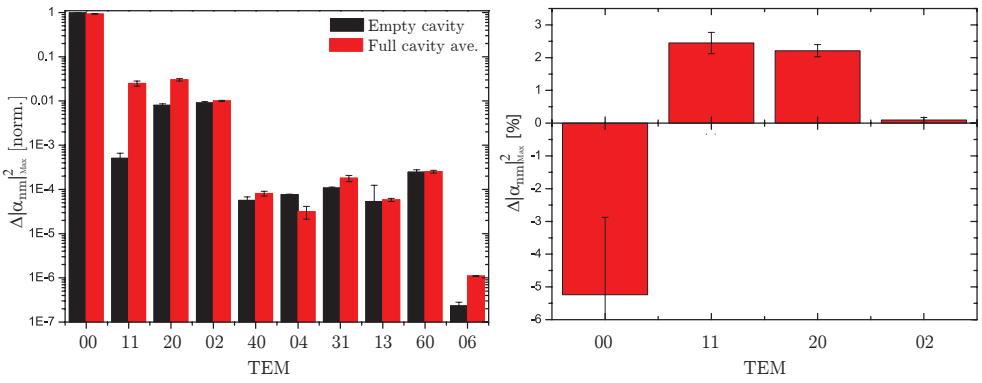

Figure 5.7: The averaged effect of atoms on the modal composition of the cavity transmission.
Left: For most higher order modes the average of the normalized maximum transmission value with atoms (red) and without atoms (black). Most modes show on average an increase in the higher order components of their mode composition.
Right:. For the most dominant four modes, the difference between both values is displayed. The data confirms the redistribution effect of the atoms, away from the central mode into higher order components. The decrease of about 5% of the TEM_{00} goes to nearly equal amounts to the (11) and (20) modes.

reduces the relative weight of the TEM_{00} component linearly from more than 98% initially with no loaded atoms to below 93% for the maximum loaded atom number. Unfortunately the straight line fit is worse for the other modes, but the fit nevertheless indicates a trend, which is, in all higher-order cases, positive.

A second analysis was conducted, since the straight line fits of the higher-order components were not so convincing. The weighted mean of the maximum mode component with atoms was compared with the empty cavity values. The results are displayed in figure 5.7 on the right. The graph looks very similar to the results of the straight line fits and in fact confirms its result: loading atoms into the cavity changes the composition of the transmitted light; the TEM_{00} component decreases, while all the other increase. Additionally, the left part of figure 5.7 presents the mode decomposition results for most of the higher-order modes used to fit the image data for the empty cavity, and the weighted mean of all the loaded cavity images. This graph also justifies the restriction to the (00,11,20,02) mode subset, since all other components were several orders of magnitude smaller.

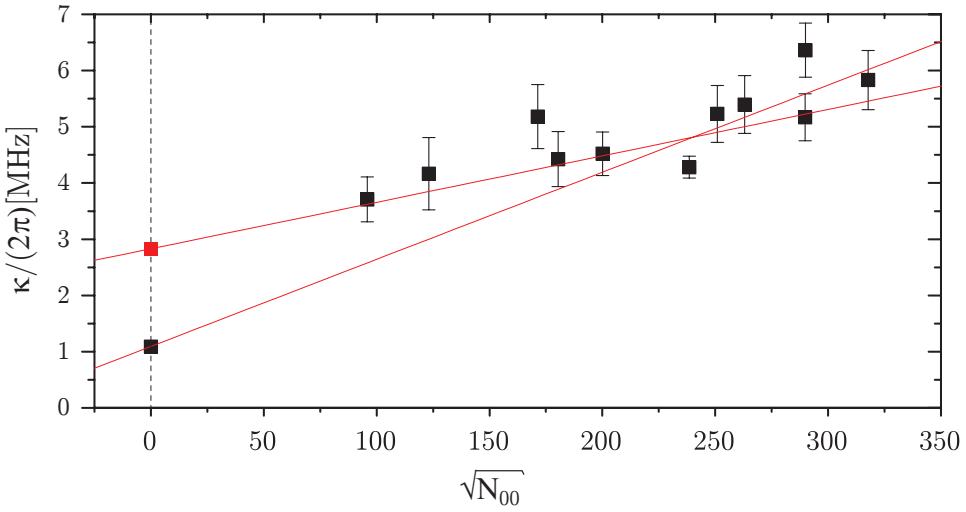

Figure 5.8: Cavity loss rate κ_{00} of the TEM_{00}-mode versus $\sqrt{N_{00}}$. All of the observed cavity loss rates are bigger with atoms in the cavity than without. The data was fitted with two straight lines. The first including the empty cavity loss rate and the second without. The interception point of the straight line fit excluding the empty cavity suggests a much higher κ than actually observed.

5.4.3 Influence of different m_F-states

The width of the observed normal mode splitting peaks in the transmission is again larger than the expected value. In the previous chapter, we speculated that the cavity loss rate is affected by the presence of higher-order transverse modes. The data in this chapter suggests this is not the case or not the main process. The cavity loss rate κ was a free fit parameter of the decomposed transmission fit and, for all the modes, a significantly increased κ was observable. The results for the TEM_{00} mode are displayed in figure 5.8. The straight line fit to the data reveals that increasing the atom number increases the linewidth of the transmission peaks. This suggests a mixture of differently coupled subgroups of atoms, due to their m_F state for example. Since we are already starting with a mixture of different m_F ground-state atoms and each subset is coupled with a different coupling constant, proportional to the dipole matrix element of the transition, it is likely that this is the true reason for the observed discrepancy to the one species model. The different m_F state populations are not accessible in the current setup and neither is it certain or likely that they remain stable during the probe with linear polarized light. But if there are different subgroups of atoms,

this also means that the mode content is effectively less than previously calculated, which increases the observed coupling even further.

5.5 Summary

This chapter presented a selection of experiments in the strong coupling regime. Several thousand ^{133}Cs atoms were effectively coupled to a nearly confocal cavity. The transverse mode degeneracy, as a characteristic of the confocal cavity and its effect on the coupling strength, was investigated. The transmission data was recorded with an intensified CCD camera and the image data was fitted with a composition of several higher-order transverse modes. The analysis of the separate mode components revealed the normal mode splitting for most of the higher-order transverse components. Therefore the atoms are simultaneously coupled to more than just one mode. To get an estimate of the single-atom coupling constant, the normal mode splitting data was displayed against the square root of the effective atom number in the respective mode. The atom number was measured from fluorescence images for each loading time, and the effective atom number was computed as the integral over the product of the MOT density and the mode's photon probability function. The observed single-atom, single-mode coupling strength was up to 80% bigger than the expected $g_{11}/(2\pi) = 64\,\mathrm{kHz}$, which could be attributed to the presence of the degenerate higher-order transverse modes according to a model presented in [85]. In fact, the first six strongest coupled modes need to contribute to explain the observed increase. A second effect the mode decomposition revealed was that the composition of the transmitted light was affected by the presence of atoms in the cavity. The relative weight of the TEM_{00} mode in the empty-cavity transmission was more than 98%, with adding more atoms and therefore increasing $\sqrt{N_{00}}$ this component decreased linearly. The atoms transferred the light into different available higher-order modes, which could find interesting application in quantum computing. Atom-filled multi-mode cavities could act as nodes in a quantum computing network, enabling the creation of multi-particle entanglement, or be used to store photonic qubits from different optical fibres in the atomic polarization. The multi-mode character of the cavity light field also enables straight forward implementation of

logic gates. Depending on the relative phase of for example two different TEM modes, they either interact with the cloud of atoms or they don't. And the relative phase of the two fields is controllable over their optical pathlength difference.

Chapter 6

Summary of the ^{133}Cs experiments

This part of the thesis presents work with cold ^{133}Cs atoms in a nearly confocal cavity. We were initially motivated to conduct research regarding a new cooling scheme implementing optical cavities. But since initial temperature measurements remained inconclusive and did not show signs of a cavity related temperature reduction, we started to investigate the basis of the cavity-atom interaction in our setup: the strong collective coupling of the cavity-atom system. The experimental apparatus built for this purpose was described and the science cavity characterized. The system is relying on two different locking schemes to guarantee frequency stability. Both are presented in detail and their overall performance exemplified. The science cavity's key feature is its large mode volume and its nearly confocal geometry. The deviation from confocality, as an important measure for the degeneracy of the higher-order transverse modes, was measured and showed a slight astigmatism, which was probably introduced during the construction phase, but was in general so small, that at least some higher-order transverse modes could be considered degenerate. The first conducted experiment proves the strong coupled character of the atom-cavity system by measuring the normal mode splitting, in the transmission signal of a probe beam, as a function of the loaded atom number. Furthermore, the dependence on the detuning of the cavity resonance to the atomic transition is investigated, and shows the characteristic avoided crossing of a coupled system. The measurements were

extended in the second experiment. Several more normal mode splitting spectra were recorded and, in contrast to the first experiment, analyzed with respect to their modal composition. We found an increased coupling constant, which might be attributed to the presence of degenerate higher-order transverse modes. The last experiment paves the way for a more thorough analysis of the observed coupling constant increase. In particular, knowledge of the initial m_F-state populations, as well as initial m_F state preparation would improve the findings. Furthermore, the initial width of the atomic sample should preferably be smaller than the fundamental cavity beam-waist to make a spatially resolved measurement possible. The spatial shape of the higher-order transverse mode interference pattern was ignored so far, but might be a key feature for the understanding of the mechanism. Analysis of the two other data sets, which were collected in the second experiment, might already shed light onto the behaviour under different pumping mode geometries.

The following part of this thesis deals with an entirely different setup from an atomic physicist's perspective, but fairly similar from an external point of view: vacuum chambers, laser beams and alkali metals are still involved. For this part, however the focus of interest lies on transport phenomena of cold ^{87}Rb atoms in modulated dissipative optical lattices. Concluding remarks and an outlook on the ^{133}Cs experiment will be given in the last chapter.

Part II

^{87}Rb atoms in dissipative optical lattices

Ratchet experiments with cold atoms have a long tradition in our group [28–30, 46]. Stochastic transport phenomena in dissipative optical lattices have been studied in great detail by several PhD students and post docs, both experimentally [22, 27, 52] and theoretically [10], since 2003. Most experimental aspects have changed but the topic has remained the same. The first apparatus, which was partly recycled for the first part of this thesis, built by Dr. Philip Jones studied the ratchet effect with ^{133}Cs atoms. Later Dr. Ralf Gommers and Dr. Peter Douglas started a second experiment with ^{87}Rb atoms in a glass cell, which was taken over by Dr. Vyacheslav Lebedev and then by me and others. All the atoms used in those experiments were trapped in MOTs loaded from the background gas; initially a great idea since the requirements for the vacuum and laser system are lower. But to take ratchet experiments further into the quantum regime [84], or to investigate chaotic transport in a Hamiltonian ratchet, the lifetime of the traps was not long enough. The limiting factor was the vacuum chamber background pressure. Thermal atoms with several 100 m/s velocity are a convincing argument to leave a Magneto-Optical Trap.

This part of the thesis describes my part of the work conducted on the ^{87}Rb ratchet machine. It will start with an introduction to the interesting field of Brownian motors and their realisation in optical lattices. Then the experimental changes to the vacuum chamber and the laser system are discussed and summarised. The following chapter deals with the first ratchet experiment [102] conducted by Nihal Abdul Wahab and myself. It generalises the results published in [17] from the amplitude domain to the frequency domain. The next chapter describes an experiment in which we used the ratchet effect merely as a tool. It investigates an effect called “vibrational resonance”. A fast oscillating force, much faster than any other time scale of the system, can be used to renormalise the depth of a potential [103]. If the results prove to be more general, several applications in atomic physics and beyond, could be imagined. In the last chapter, the main results of this part are summarised and an outlook on the ^{87}Rb experiment is given.

Chapter 7

Brownian Motors - Extracting work from thermal fluctuations

The quest to trick nature into providing infinite amounts of energy from nothing is probably as old as society itself. The idea behind Brownian motors or, for electric circuits, Brillouin's rectifiers is to use mechanical or electrical rectification mechanisms to extract useful work from thermal fluctuations. For an electrical circuit it is easier to construct because it would simply be a diode and a resistor in series. The diode would rectify the resistor's thermal white Johnson noise and the current could be used to drive an engine: energy from nothing. Brownian motors follow the same mechanism in mechanics. One might think of it as a windmill working without wind; just random collisions of gas atoms with the wings of the windmill cause rotation and the mill to do work. Normally those collisions average to zero, but with a suitable way to hinder momentum transfer in one direction, the mill rotates in the other direction: a weight gets lifted while the environment spontaneously cools. The device to rectify the fluctuation is called a ratchet and a model of the mechanism can be seen in figure 7.1. If the apparatus were at thermal equilibrium, the extraction of work would violate the second law of thermodynamics. If the temperatures of the reservoir on the left and the reservoir on the right are different the apparatus is just a normal heat engine, as shown by Feynman in his famous lectures [23]. But our motivation to study the

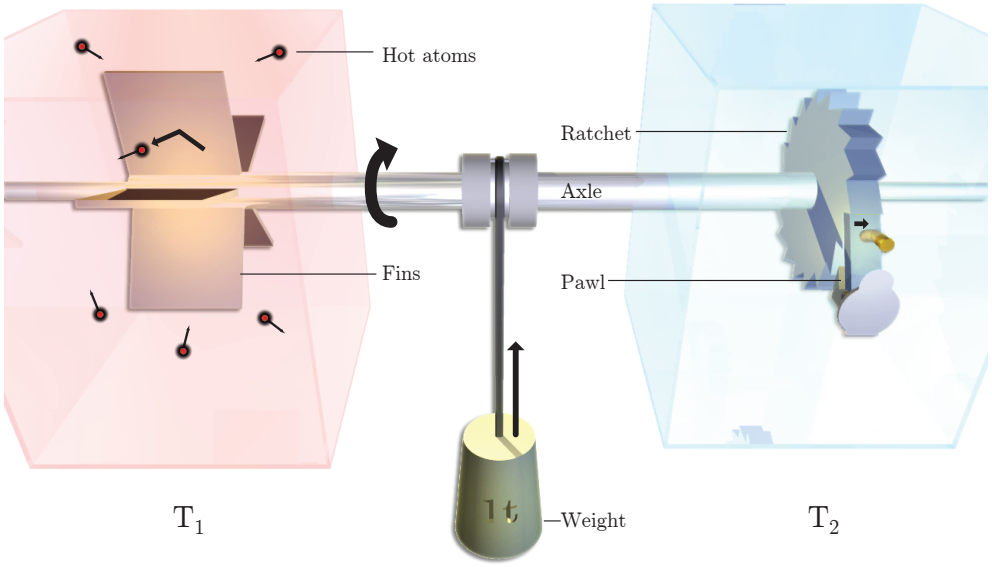

Figure 7.1: Example of a Feynman Ratchet. Gaseous atoms in the container on the left collide with the large but very lightweight fins of the apperatus. The axle connects the fins to a wheel with asymmetric teeth. A pawl stops the wheel rotating in one direction but doesn't hinder rotation in the other. If an atom collides with the fins in container 1 in the right direction it will rotate the axle and lift the weight. If the direction is wrong the rotation is stopped by the pawl and the weight stays where it is. If the temperature T_1 is higher than T_2 this apparatus could actually work.

ratchet effect has a related but slightly different origin: the generation of deterministic transport in a noisy environment with an unbiased driving force. It is a recurring theme in modern science with wide ranging implications for a variety of research areas, reaching from the understanding of intercelluar transport in biochemistry, to stochastic resonances in models to explain the periodic occurence of the ice ages. A great introduction and review of the field is given by Peter Reimann in [81] and, more recently, by Peter Hänggi and Fabio Marchesoni [35]. The design criteria given for a Brownian motor from [35] are the following:

1. "Spatial and temporal periodicity critically affect rectification."

2. "All acting forces and gradients must vanish after averaging over space, time and statistical ensemble."

3. "Random forces of thermal, non-thermal or even deterministic origin assume a prominent role."

4. "Detailed balance symmetry" ... "must be broken by operating the

device away from thermal equilibrium."

5. "A symmetry breaking mechanism applies."

Our implementation of a Brownian motor in the so called rocking ratchet configuration is an ensemble of cold ^{87}Rb atoms in a closely red detuned dissipative optical lin. ⊥ lin. lattice. It is a spatio-periodic potential driven by a biharmonic force with time average zero. Random forces are implemented by photon scattering of the atoms. The driving force brings the system far away from thermal equilibrium and the question to answer is: which symmetry-breaking mechanism is responsible for the observed transport? The direction and the strength of the resulting current is a non-trivial function of the system parameters such as the driving frequency, amplitude and phase, the scattering rate, the potential depth and so on. Current reversals are an important feature of a ratchet system. In applications such as the separation of different atomic species, it would be perfect to be able to choose external parameters resulting in a particle current in one direction for one species and a current in the other direction for the other species. In general, tuning system parameter over a broad range with a single handle is quite a desirable situation. The theoretical interpretation of the occurrence of current reversals is a much discussed, controversial topic and "...has given rise to research activity on its own" [59].

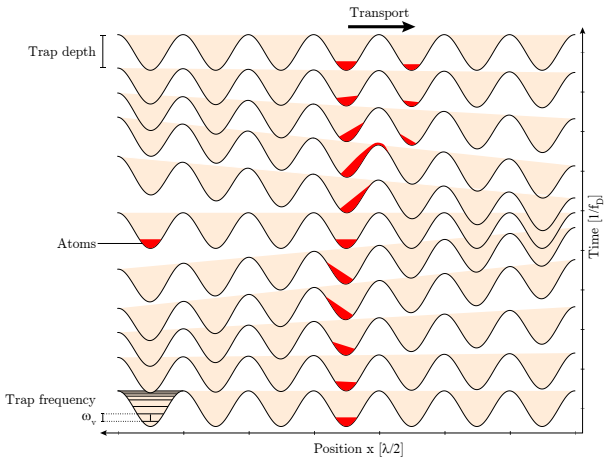

Figure 7.2: Illustration of the rocking ratchet mechanism. In the accelerated frame of the lattice the atom experiences an oscillating force. The response of the atoms depends on all the system parameters, like potential depth and vibrational frequency, but also on the amount of damping due to Sysiphus cooling and the nonlinearity of the potential.

A rocking ratchet in our case is implemented by modulating the frequency of one of the lattice beams. This produces a periodically moving

interference pattern in the laboratory frame and a periodically tilting potential in the accelerated frame of the lattice. In the illustration of figure 7.2 the periodic potential of the lattice is shown for different instances in time during one biharmonic modulation cycle. The processes for current generation range from harmonic mixing [24] to gating effects [32].

Chapter 8

Experimental Upgrade - Double chamber ^{87}Rb machine

This chapter describes the changes made to the ^{87}Rb experiment after taking it over from the previous PhD student. It progressed from being a single MOT chamber, loaded from the background gas with a high pressure and a small lifetime, to a double MOT system with a differential pumping stage and two magneto-optical traps. The first MOT providing precooled atoms in a concentrated beam to load the second MOT in an ultra high vacuum environment. Even though those changes were not necessary for the following experiments, they were important upgrades for future experiments and made the conducted experimental data-taking process much more convenient; if just for the bigger number of atoms and the resulting contrast enhancement. This chapter presents the new vacuum chamber, the laser system, and the calibration of the EOM setup used in chapter 10.

8.1 The new vacuum design

The old vacuum system for ^{87}Rb experiment is described in [52] and was built by Ralf Gommers and Peter Douglas. The pumping tract of the chamber was similar to the one in the previously mentioned ^{133}Cs experiment. But instead of Kimballs Extended Octagon the MOT was

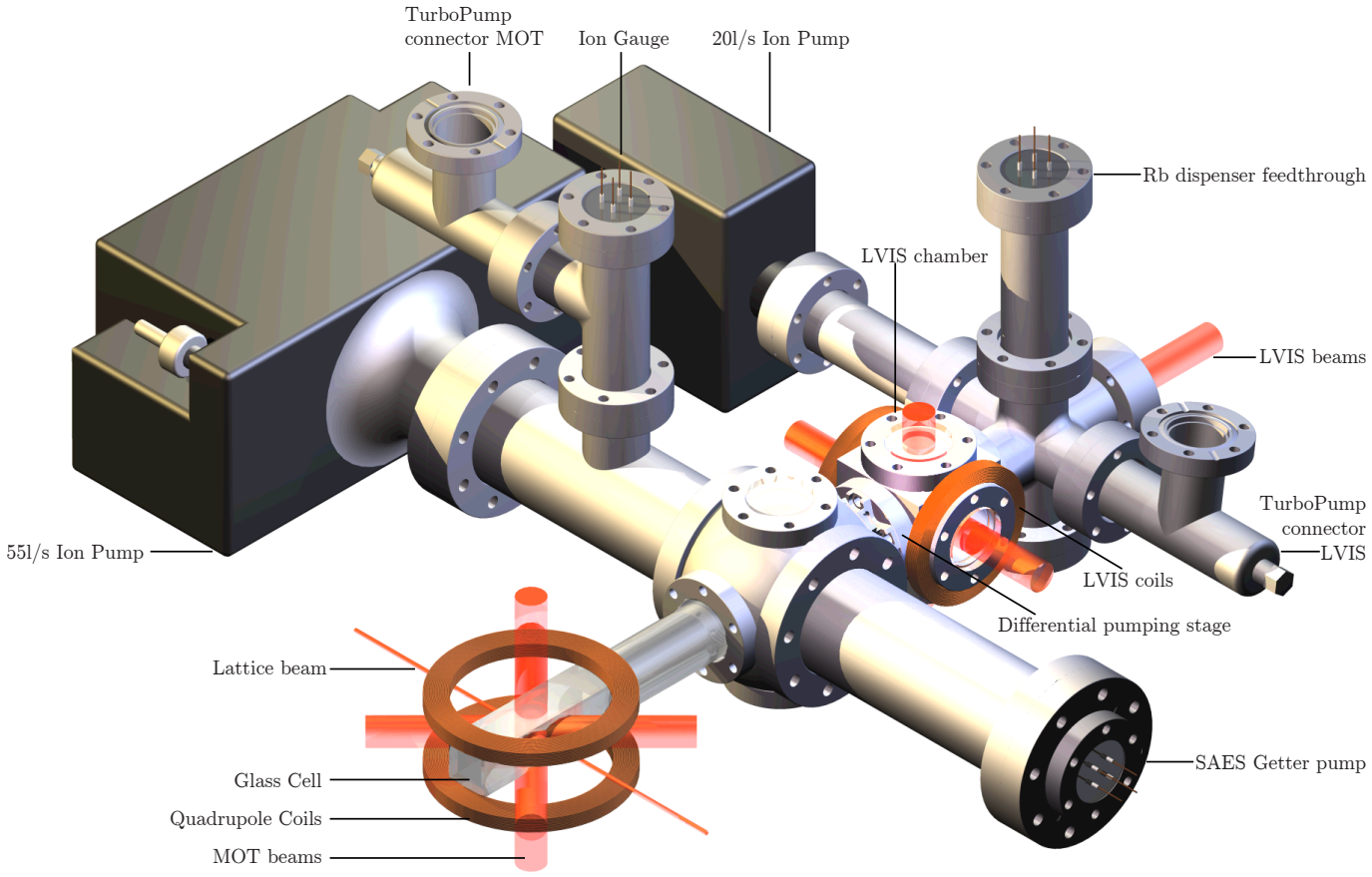

Figure 8.1: Overview of the new ^{87}Rb vacuum setup.

trapped in the centre of a glass cell. It was loaded from background gas containing ^{87}Rb emitted from alkali dispensers[1] in the same part of the chamber. The achieved vacuum pressure was higher than 4×10^{-9} mbar measured via the ion pump current limiting the lifetime of the trap to below 3 s and would therefore not be suitable for the creation of a Bose-Einstein Condensate for example (or just a very small one). The new vacuum design is displayed in figure 8.1 in an overview and in figure 8.2 in detail showing the orientation of the cold atomic beam and the LVIS (Low-Velocity Intense Source of atoms).

The chamber contains two magneto-optical traps, one in the LVIS chamber and another one in the glass cell. Both chamber parts are con-

[1]SAES Getter, Rb AMD Rb/NF/5.4/12.5/FT 10

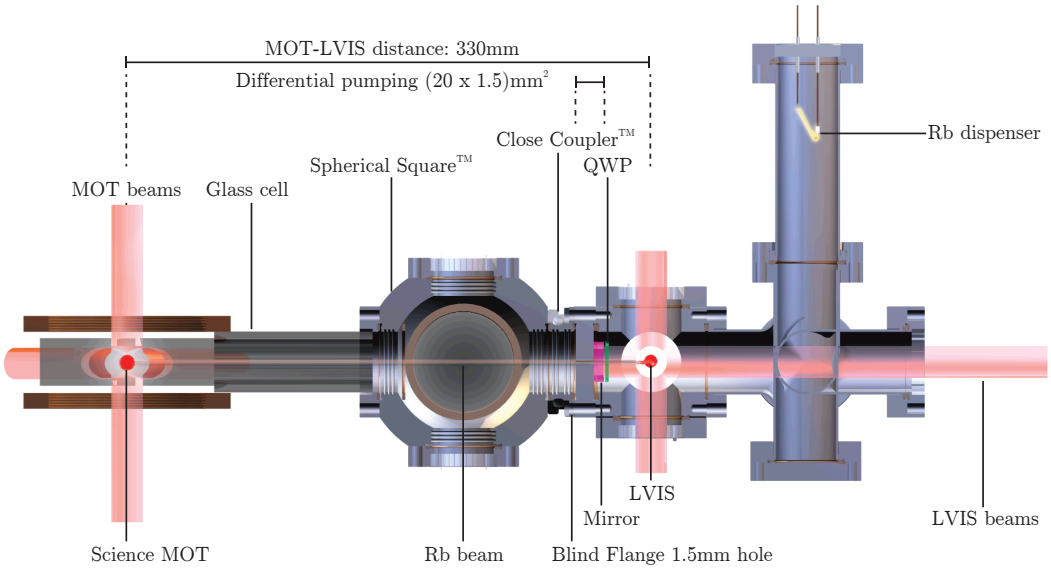

Figure 8.2: Section through the ^{87}Rb vacuum setup along the atom beam. The distance between the two MOTs is indicated as well as the differential pumping stage.

nected via a (1.5×20) mm^2 hole acting as a differential pumping stage. The pressure in the small chamber is much higher since also contains the source of ^{87}Rb atoms in form of three ^{87}Rb dispensers. The pressure in the LVIS chamber is maintained by a 20 l/s ion pump[2], and in the glass cell by a 55 l/s ion pump[3] and a SAES getter pump[4]. An additional ion gauge offers the possibility to read out the vacuum pressure. Both chambers are accesible via a valve for the initial pump down. After construction the whole chamber was baked at about 130 °C for several days to increase outgassing and therefore reduce the final background pressure. The maximum temperature was limited by the glue[5] used to fix the LVIS mirror and the quarter wave plate in the 6-way cube. But nevertheless a pressure well below 2×10^{-10} mbar was reached. Due to technical problems with the driver of the ion gauge we were restricted to use the ion pump controller[6] to read out the pressure, and since it reached its minimum we need to measure the trap life-time to deduce the vacuum pressure. The design of the vacuum chamber was supposed

[2]Varian Inc.,Vaclon Plus 20 StarCell
[3]Varian Inc.,Vaclon Plus 55 StarCell
[4]SAES Getter, SORB-ACGP100 MK5 St 707
[5]TorrSeal
[6]Varian Inc., Dual Controller

to be compact. The distance between the LVIS and the science MOT was kept to a minimum to decrease the amount of atoms lost due to gravitational sag and divergence of the cold atom beam. Another design criteria for the UHV side was to have the biggest possible connection to the powerful pumps so as not to reduce their pumping speed by geometrical limitations. Both pumps are made for a 4 1/2" flange. To connect them in the most sensible way to the 2 3/4" flange of the glass cell and the cube, we used another Kimball component[7]: a so called spherical square with two 4 1/2" ports and four 2 3/4" ports. The small ports are occupied by the glass cell, two viewports (for atomic flux measurements, or an optical plug beam for example) and, in line with the glass cell, a flange adaptor from Kimball Physics[8]. This adaptor connects the spherical octagon with the blind flange of the LVIS cube in under 18 mm. The overall distance from the LVIS to the science MOT is 330 mm. Figure 8.2 presents a section of the setup. The LVIS in the standard 2 3/4" 6-way cube is principally just a normal MOT, but the 6th MOT beam in the direction of the science chamber is back reflected from a mirror and a quarter wave plate glued to a blind flange. The mirror, quarter wave plate and blind flange contain concentric 1.5 mm diameter holes. For atoms in front of the hole, radiation pressure is unbalanced and the LVIS beam from the right pushes cold atoms into the science cell. There the beam of cold atoms gets trapped again by a second set of 6 MOT beams and a magnetic quadrupole field. A helpful comparison in terms of atomic flux of different two-chamber-systems can be found in [72]. Figure 8.3 shows one of the first loading curves of the science MOT in the glass cell on the left, and a characteristic decay curve after switching the LVIS off on the right. Even though there is plenty of room for improvement in terms of the loading rate ($18 \times 10^6 \frac{\text{atoms}}{\text{s}}$) and the final atom number, after 416 s (roughly 7 min) there are still 3% of the atoms left. This alone would correspond to an exponential decay time of 132 s (in good agreement with the longer lifetime in the double exponential fit) and a vacuum pressure of 6.5×10^{-11} mbar. This is of course just a rough estimate according to calculations in [4] presuming that just background ^{87}Rb atoms collide with the trapped ensemble, leading to trap loss in

[7] Kimball Physics, MCF450-SphSq-E2C4
[8] Kimball Physics, MCF275-FlgAdptr-C2

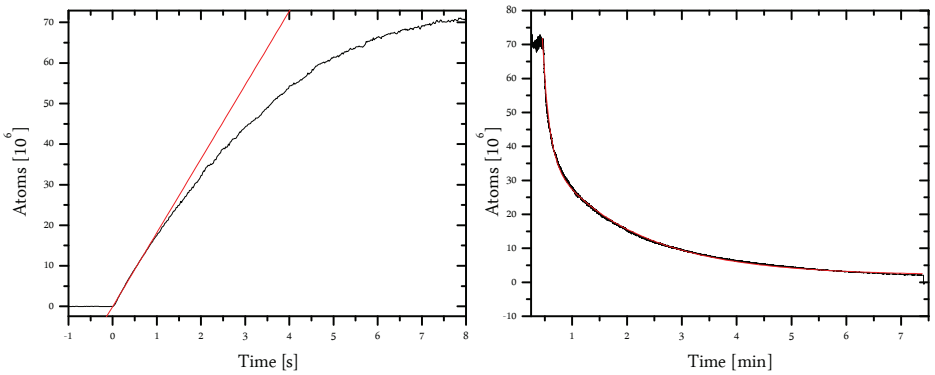

Figure 8.3: ^{87}Rb science MOT loading and decay.
Left: The loading of the ^{87}Rb science MOT. The fitted line from the origin has a slope of 18×10^6atoms/s.
Right: After switching the atomic source off, the science MOT decays. The curve was fitted with a double exponential decay. The longer exponential decay time is 131.4 s. The quicker initial decay with $\tau = 9.9$ s is most probably density related.

70% of all collisions. But it nevertheless shows the suitability for BEC creation in a magnetic trap.

8.2 Rb Laser System

The laser system of the double MOT system is displayed in figure 8.4. For remarks about the locking schemes and the abbreviations relate to chapter 3. The setup consists of two ECDLs locked via DF-DAVLL to different ^{87}Rb transitions. The first ECDL, the master laser, is stabilised to the prominent $5^2S_{1/2}\, F = 2 \rightarrow 5^2P_{3/2}\, F = 1, 3$ crossover feature, then upshifted by about 200 MHz with a double pass AOM. The frequency of this AOM can be changed via the computer control the detuning to the cycling transition can be adjusted between $-6\Gamma \leq \Delta_A \leq +2\Gamma$. The close to resonant light then injects the slave for the LVIS and another slave for the lattice. The rest of the light is shifted further up with another AOM by 80 MHz and then injected into a third slave for the science MOT. This is done in order to have an AOM in the beam path of the third slave so that the intensity of the science MOT cooling light can be controlled by varying the applied radiofrequency amplitude. This is necessary to switch the light off rapidly (of course with an additional mechanical shutter to shut off any leaked light left) but mostly to control the intensity of

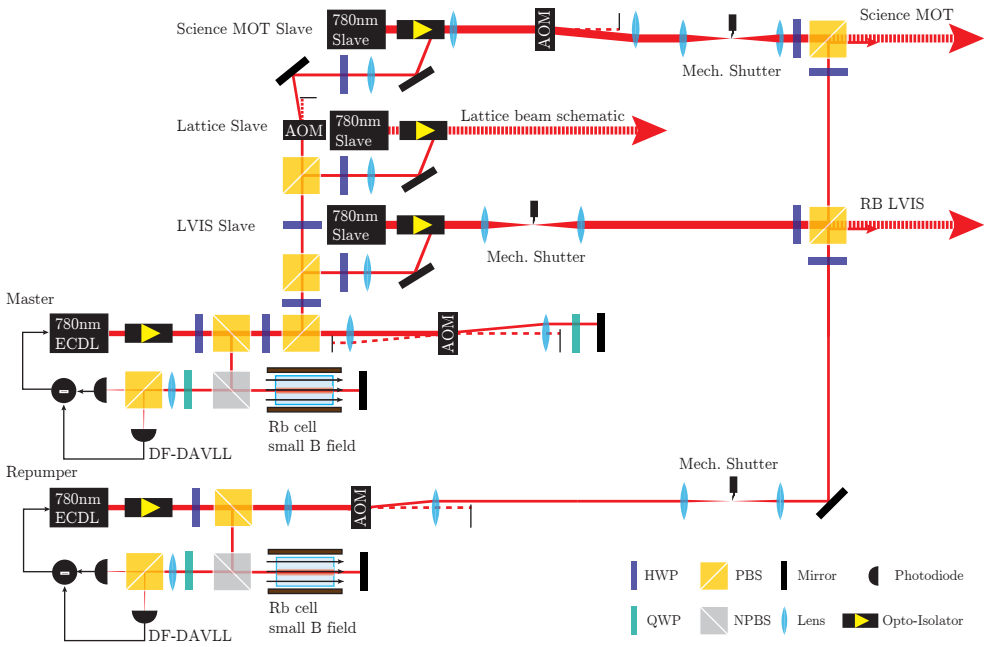

Figure 8.4: ^{87}Rb laser system for the double MOT system. Two ECDL lasing at 780 nm produce the cooling and repumping light for two MOTs and one optical lattice beam. For details see text.

the light e.g. to optimise an optical molasses phase. All laser diodes used are wavelength selected[9]. The repumper ECDL is also locked via another DF-DAVLL to the $5^2S_{1/2}F = 1 \rightarrow 5^2P_{3/2}F = 1, 2$ crossover and upshifted by an AOM to be on resonance with the $5^2S_{1/2}\ F = 1 \rightarrow 5^2P_{3/2}\ F = 2$ transition. After the AOM the beam is split for the two MOTs and overlapped with the cooling beams. The lattice laser setup will be presented in the following chapter since it varies slightly between the two experiments.

8.3 Double pass electro-optic modulator

For the fast modulation of the optical lattice we implemented an Electro-optic modulator (EOM). EOMs are powerful devices to produce high frequency phase-modulation of a laser beam. They rely on the linear electro-optic effect, which describes a change in refractive index proportional to an applied voltage in crystals without inversion symmetry. The

[9]Sanyo DL-7140-201W

change in refractive index alters the optical path length and therefore the phase of a laser beam passing through it. EOMs come in two kinds: single frequency and broadband. Since the required voltages are quite high, single frequency EOMs include microwave cavities to guarantee large modulation indices β for low drive voltages. But the frequency response exhibits a narrow band-pass characteristic which makes them mostly interesting for sideband production at high frequencies. For the experiment discussed in chapter 10 we used a broadband EOM[10], which doesn't possess a microwave cavity (which would also be quite big for the frequency involved) and therefore needs high driving voltages. The maximum input voltage is 210 V corresponding to a maximum phase change of $\phi = 3.15$ rad with a modulation index of $\beta = 15$mrad/V at 1064 nm. The driver for the EOM was home built according to the design in [69]. It is a differential amplifier configuration with complementary emitter followers providing peak-to-peak voltages of up to 550 V with just a 300 V power supply. It achieves that by swapping polarity of the output signal each halfwave. The gain is supposed to be factor 100 and the large signal bandwidth up to 1300 kHz; just about enough for our purposes. To increase the maximum modulation index, we double passed the EOM, which effectively doubles the modulation index for a given voltage (and the modulation frequencies involved).

EOM calibration The electric field of a laser beam with a sinusoidal phase modulation can be written as:

$$E_{mod}(x,t) = \frac{E(x)}{\sqrt{2}}\left(e^{-i\omega t}e^{-i\beta\sin(\omega_{\mathrm{HF}}t)} + \text{c.c.}\right). \tag{8.1}$$

Here ω is the frequency of the light field, ω_{HF} the frequency of the modulation and β the modulation index. For small β, expanding the modulating exponential into a Taylor series and expressing $\sin\omega_{\mathrm{HF}}t$ by exponentials leaves:

$$E_{mod}(t) = \frac{E(x)}{\sqrt{2}}\left[e^{-i\omega t}\left(1 - \frac{\beta}{2}\left(e^{i\omega_{\mathrm{HF}}t} - e^{-i\omega_{\mathrm{HF}}t}\right)\right) + \text{c.c.}\right], \tag{8.2}$$

[10] EOM New Focus 4002-M

which is the laser light oscillating with now three frequencies: ω, $\omega - \omega_{\mathrm{HF}}$ and $\omega + \omega_{\mathrm{HF}}$, the carrier and the first pair of side bands:

$$E_{mod}(x,t) = \frac{E(x)}{\sqrt{2}}\left[e^{-i\omega t} \pm \frac{\beta}{2} e^{i(\omega \mp \omega_{\mathrm{HF}})t} + \text{c.c.}\right]. \tag{8.3}$$

This is a common derivation to make the appearance of side bands plausible but more generally the amplitude of the n-th sideband is given by the n-th Bessel function $J_n(\beta)$, with the modulation index as the argument. Bessel functions are oscillating functions of their argument, so for specific modulation indices the corresponding sideband dissappears. Figure 8.5 shows the optical setup used to calibrate the EOM. The lattice laser

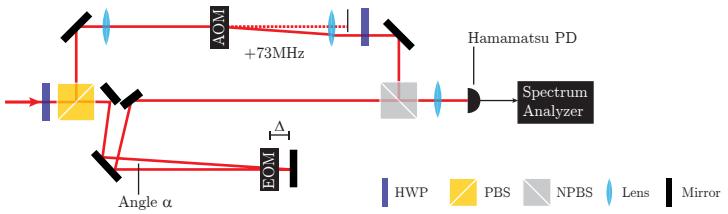

Figure 8.5: The optical setup for the calibration of the EOM. For details regarding the calibration process refer to the text.

beam is split by a polarising beam splitter cube. One component passes through the double pass EOM while the other component passes through an AOM to get shifted in frequency by +73 MHz. The light passes the EOM in a small angle α and gets backreflected after a small distance Δ. The small angle is introduced to separate incoming and outgoing beams to be able to use all the power and not to rely on a beamsplitter. Δ adds a phase difference between the two passes through the EOM, but for the frequencies involved in our experiment it can be ignored. After rotating the polarization into the same plane, both beams are overlapped again on a non-polarizing beamsplitter and the homodyne signal is recorded with a fast photodiode[11]. The analysis on a spectrum analyzer[12] looks like figure 8.6 for different applied modulation voltages. The signal is centred around the frequency difference of the two beams of +73 MHz. The last panel in 8.6 shows the simulated frequency spectrum of the laser beam for the maximum available modulation index β. The first 14 sidebands have non-negligible amplitudes corresponding to a spectral width of $28\,\omega_{\mathrm{HF}}$.

[11] Hamamatsu, GaAs MSM Photodetector G4176-03
[12] Anritsu MS2718B Spectrum analyzer 9 kHz-13 GHz

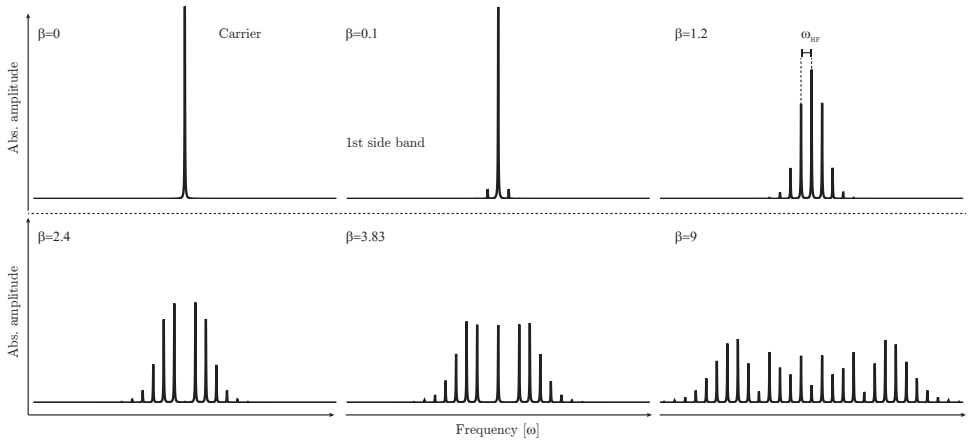

Figure 8.6: The plots show the frequency components of a sinusoidal phase modulated light field with modulation index β and modulation frequency ω_{HF} for different modulation indices. $\beta = 0.1$ corresponds to the case used for the Pound-Drever-Hall stabilisation in chapter 3, for $\beta = 2.41$ the carrier amplitude becomes zero and for $\beta = 3.83$ the first sideband disappears. The last panel shows the maximum modulation index used in the experiment discussed in chapter 10.

With $\omega_{\mathrm{HF}}/(2\pi) = 1\,\mathrm{MHz}$ the light would be much broader than the bandwidth of an AOM (used for the production of the biharmonic force for example). Besides, the refraction angle for the frequency component at $\pm 14\,\omega_{\mathrm{HF}}$ would be quite different, spatially separating the orders. This is why, in contrast to the slow frequency modulation of the lattice beam for the ratchet effect done with an AOM, the high frequency modulation needed the EOM. In order to find out about the effective modulation index, the applied voltage corresponding to Bessel function zeros of the first two sidebands and the carrier are recorded and displayed for three example frequencies in figure 8.7 on the left, and in a summary on the right. The bandwidth of the EOM driver and EOM together appears to be larger than the one predicted for the EOM driver alone (large signal bandwidth $-3\,\mathrm{dB} = 1.3\,\mathrm{MHz}$). All the β/V are within the -3 dB limit and the whole system is therefore suitable to investigate the effect of a high frequency modulation on an optical lattice potential in chapter 10.

8.4 Summary

In this chapter the changes made to the ^{87}Rb vacuum system were motivated and discussed. The new chamber contains two MOTs in a so

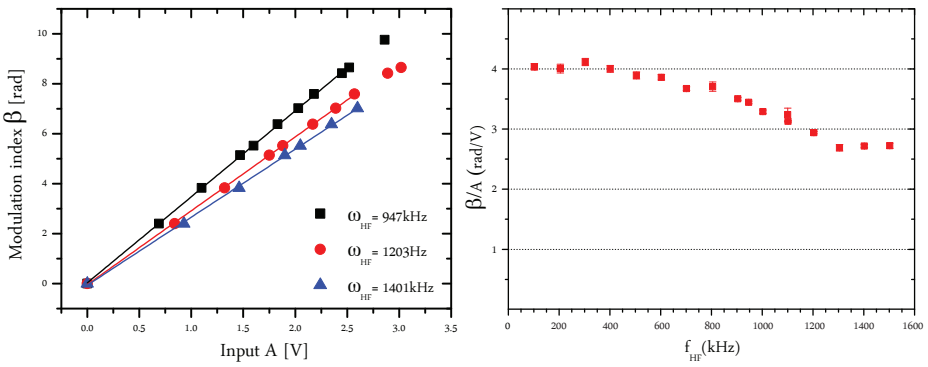

Figure 8.7: The results of the EOM calibration. The voltages corresponding to oberserved zeros of the Bessel function are used to calibrate the modulation index β per volt. The graph on the right shows the summary of the measurements in the first graph. All the shown frequencies are within the -3 dB range commonly used to identify the bandwidth of a circuit.

called LVIS configuration. The vacuum pressure in the science part of the chamber improved dramatically and a MOT lifetime of up to 132 s was observed, corresponding to a vacuum pressure of 6.5×10^{-11} mbar. The laser system used for the following experiments is briefly described and the EOM construction discussed. The modulation bandwidth was determined to be above 1.5 MHz and the maximum modulation index to be 10.5 rad, for low driving frequencies.

Chapter 9

Current reversals in a rocking ratchet: The frequency domain

The experimental results of this chapter have been published in [102]: A. Wickenbrock, D. Cubero, N. A. Abdul Wahab, P. Phoonthong, and F. Renzoni. *Current reversals in a rocking ratchet: The frequency domain.* Physical Review E 84, 021127 (2011).

9.1 Previous work

This work relates to an experiment done in 2010 by our group [17] in collaboration with David Cubero from the university of Seville, Spain. It studied the mechanism of a current reversal in a rocking ratchet when varying the amplitude of the drive, both experimentally and theoretically. The mechanism behind the current reversal was identified as symmetry breaking due to dissipation-induced phase lag. It was shown that this kind of current reversal is only observable in a ratchet system with moderate dissipation. Numerical simulations confirmed that in the overdamped case, as well as in the Hamiltonian limit, this kind of current reversal could not be observed. Previous attempts to theoretically analyse the origin of current reversals [59] considered a correspondence to a bifurcation between a chaotic and an ordered regime, identifying it as a

dynamic effect. To extend the argument in favour of dissipation-induced symmetry breaking as the dominant mechanism, the work in this chapter generalises the results in [17] to a second observed current reversal occuring when varying the drive frequency of the ratchet. Numerical simulations, conducted by David Cubero, confirm the dependence of the reversal on the amount of dissipation.

9.2 Experimental Setup and symmetry analysis

We consider a ratchet setup consisting of Brownian particles in a spatially symmetric periodic potential driven by a biharmonic oscillating force. The Langevin equation, including a linear friction term, governing the dynamics is:

$$m\ddot{x} = -\alpha\dot{x} - \frac{\partial U(x)}{\partial x} + F(t) + \xi(t). \tag{9.1}$$

Here $U(x) = U_0 \cos(2kx)/2$ is the periodic potential created by the 1D optical lattice, α the friction coefficient due to the presence of sub-Doppler cooling mechanisms, $\xi(t)$ a Gaussian white noise term due to photon scattering, uncorrelated and with average zero ($\langle \xi(t) \rangle = 0$ and $\langle \xi(t)\, \xi(t') \rangle = 2D\delta(t - t')$), and $F(t)$ the biharmonic force from the lattice beam modulation described by:

$$F(t) = F_0 \left[A_1 \cos(\omega_D t) + A_2 \cos(2\omega_D t + \phi) \right]. \tag{9.2}$$

Symmetries Symmetry analysis is a powerful tool to investigate whether, for a given ratchet setup, a directed current can occur or not. In general, if the equation of motion is invariant under a transformation, which can transfer one atomic trajectory into another one with opposite velocity, the average observed particle current is zero. In order to get directed current in a spatio-periodic potential, the following symmetries need to be broken [24]: the shift symmetry; particle trajectories are invariant under the transformation:

$$(x, p, t) \Rightarrow (-x, -p, t + T/2), \tag{9.3}$$

with T the period of the drive. The shift symmetry is broken for any value of the phase ϕ in a biharmonic drive given by equation 10.14. The second symmetry to be broken is the time reversal symmetry, corresponding to invariance under the transformation:

$$(x, p, t) \Rightarrow (x, -p, -t)\,. \tag{9.4}$$

Since this symmetry depends on the damping of the particle in the lattice, three different scenarios need to be distinguished. First, the Hamiltonian case: no dissipation leaves the time reversal symmetry intact for values of the phase $\phi = n\pi$ with n integer. Therefore no particle current can occur. It can be shown [24] that the resulting average velocity for a lattice without dissipation is, in leading order:

$$\langle v \rangle = v_{max} \sin \phi. \tag{9.5}$$

The opposite extreme, the overdamped regime, realised numerically by neglecting the inertia term in equation 9.1, involves a third symmetry: the so called *super-symmetry* [81]; particle trajectories remain invariant under the transformation:

$$(x, p, t) \Rightarrow (x + \lambda/2, -p, -t)\,, \tag{9.6}$$

with $\lambda/2$ the spatial period of the optical potential. For values of the phase $\phi = \pi/2 + n\pi$ with n integer, the system is symmetric under this transformation and the generation of a directed current is prohibited. In our case, a system with moderate amounts of dissipation, time symmetry is broken for values of the phase $\phi = n\pi$ allowing the generation of current. If the dissipation is weak a dissipation-induced symmetry breaking phase lag ϕ_0 has to be taken into account. The current then follows [78]:

$$\langle v \rangle = v_{max} \sin(\phi + \phi_0)\,, \tag{9.7}$$

where the phase lag ϕ_0 vanishes in the Hamiltonian limit and becomes $-\pi/2$ in the overdamped regime. Note that the sign of the phase lag differs from the literature [78] to be consistent with the experimental data. The experimental realisation is shown in 9.1. The MOT master laser

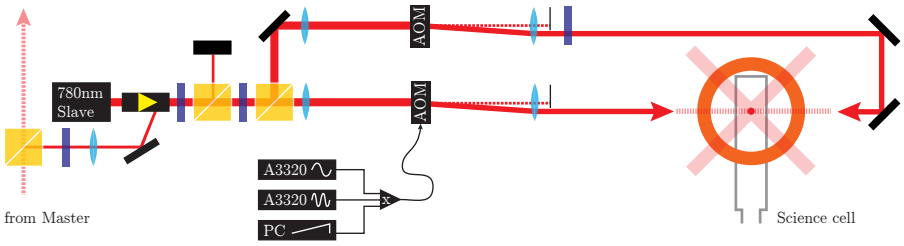

Figure 9.1: Schematic of the lattice laser for the current reversal analysis.

(compare figure 8.4) injects the lattice slave with light having a detuning of $-6\Gamma \leq \Delta \leq +1\Gamma$. The light then gets split by a polarising beam splitter and each arm is fed through an AOM. The AOM shifts the resulting lattice frequency to a detuning of $\Delta = (-9 \pm 0.5)\,\Gamma$. The frequency of one AOM gets modulated according to the biharmonic force. The signal of two computer controlled phase locked function generators[1] is electronically added and multiplied with a constant third signal. The multiplication ensures that the modulation can be switched on adiabatically by applying a ramp voltage from the computer control[2]. The resulting signal is fed into the frequency modulation input of the AOM driver[3]. The amplitude of the modulation A_ν is measured in Hertz frequency shift per applied voltage . The resulting force amplitude on an atom in the accelerated frame of a sinusoidal input signal can be written as:

$$F_0 = -\frac{m}{k}\,(2\pi)^2\,A_\nu f_D U_{FG}, \tag{9.8}$$

with m the atomic mass, k the wavevector of the lattice, A_ν the modulation amplitude, f_D the modulation frequency in Hertz, and U_{FG} the applied voltage from the function generator. So in order to keep the modulation force amplitude constant for different frequencies the amplitude of the frequency modulation must be adjusted. The different force amplitudes will be abbreviated with:

$$F_0 \propto A_\nu f_D U_{FG} = g_0, \tag{9.9}$$

[1] Agilent: 3220A, 20 MHz Function / Arbitrary Waveform Generator.

[2] The computer control on ^{87}Rb experiment possesses essentially the same components as the one described in chapter 3. Even though the user interface is quite different the hardware components are the same.

[3] Rohde & Schwarz: Signal Generator 9 kHz- 1.040 GHz.

since all the other system parameters remained the same.
A typical experimental procedure can be seen in table 9.1. The sequence

Experimental Sequence	MOT Loading	LVIS off	Load Lattice	Modulation Ramp	Full Drive	Delay	Image	Delay	Background
Time [ms]	3000	50	2	1	8	2.2	2	100	2
MOT shutter									
MOT switch									
LVIS switch									
B-field MOT									
Lattice switch									
Mod. Trigger									
Mod. Index				ramp	full				
Camera trigger									

Table 9.1: The experimental control sequence for the current reversal experiment. The columns from left to right represent the timestamp as they are written into the computer control cards. Most channels are digital, where green indicates the ON state and grey the OFF state. With a lattice beam detuning of $(-9 \pm 0.5)\ \Gamma$ and a beam intensity of $43.5\,\mathrm{mW/cm^2}$, the corresponding vibrational frequency was $\omega_{vib}/(2\pi) = (175 \pm 5)$ kHz.

starts with loading the science MOT from the LVIS for 3 seconds. This way, up to 10^8 atoms were loaded before the LVIS beams were switched off. After 50 ms delay the MOT magnetic field and laser beams were switched off as well and the lattice beams turned on. In 2 ms the atoms were cooled via Sysiphus cooling until they were localised in the lattice. Then the modulation was linearly ramped up; one millisecond appeared to be sufficient to avoid any switching effects. For each frequency the modulation was kept at full amplitude for another 8 ms. After an appropriate delay time for the mechanical shutter of the MOT beams to open, the cloud was imaged via fluorescence imaging onto a CCD. Since the CCD camera used in the ^{133}Cs experiment had a higher quantum efficiency than the one used initially in the ratchet setup[4], it was used for this experiment as well. The background image was taken 50 ms after the first image and immediately subtracted. The resulting image was fitted with a 2D gaussian via a MATLAB script and the key parameter displayed and saved.

[4] AVT Marlin F-033B/C

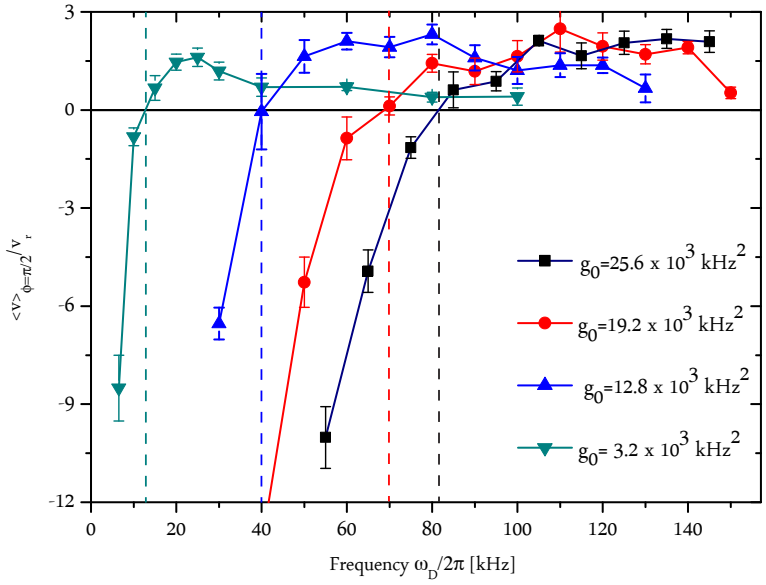

Figure 9.2: The observed ratchet current for a biharmonic phase of $\phi = \pi/2$ as a function of the applied drive frequency $\omega_D/(2\pi)$ for four different driving amplitudes g_0. For all force amplitudes a current reversal, marked by the vertical lines, is clearly visible.

9.3 Experimental Results

The first experiment conducted implemented a driving force (equation 10.14) with a phase fixed at $\phi = \pi/2$ between the two harmonics. In the Hamiltonian regime this is where the maximum current should be observable. The ratio between the two force amplitudes was chosen to be $A_1/A_2 = 2$. The aim of the experiment was to investigate how the observed current behaves with a variation of the drive frequency ω_D. After driving, the MOT is imaged via fluorescence imaging to deduce the velocity of its centre of mass. A typical experimental sequence is shown in table 9.1. For each driving frequency several images were taken and averaged. The experiment was repeated for different maximum force amplitudes A_1 and A_2. While varying the frequency, the product of frequency and driving amplitude was kept constant according to equation 9.8. The resulting current, in units of the recoil velocity, is shown in figure 9.2. The appearance of a current reversal as a function of the drive frequency ω_D, as predicted [57] and observed before in [31], is clearly visible for all

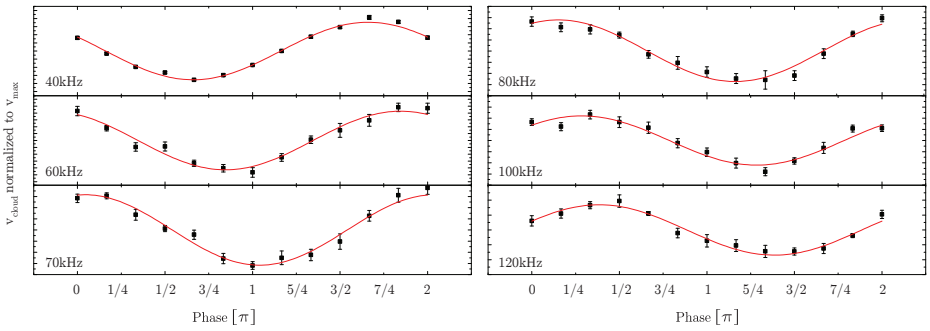

Figure 9.3: Experimental results for a force amplitude of $g_0 = 19.2 \times 10^3\,\mathrm{kHz}^2$. The average cloud velocity is presented for different phases of the biharmonic drive. Each panel shows experimental data for a different frequency normalized to the maximum velocity for comparison. The data is fitted according to equation (9.7). Cleary visible is a major variation in the dissipative phase lag ϕ_0 with the drive frequency $\omega_D/2\pi$.

driving amplitudes. To establish a relationship of the current reversal with dissipative effects, the current has to be studied as a function of the phase between the two harmonics of the driving. The resulting sine curve should behave according to equation (9.7). For each driving force amplitude g_0 and driving frequency ω_D the phase of the two harmonics was varied from 0 to 2π in steps of $\pi/6$. As an example the resulting plots for the force amplitude $g_0 = 19.2 \times 10^3\,\mathrm{kHz}^2$ and six different frequencies are shown in figure 9.3. The full analysis can be seen in figure 9.4. For each set of the four force amplitudes investigated, the resulting sine amplitude v_{max} and the resulting phase lag ϕ_0 derived from fitting the data with function (9.7) is displayed for the different drive frequencies. While the amplitudes stay always finite for each curve, the phase lag shows a large variation from $-\pi$ to 0 around the current reversal frequency observed in figure 9.2. Note that the phase of the biharmonic drive was fixed at $\phi = \pi/2$ so that a phase lag value of $\phi_0 = -\pi/2$ results in a vanishing current. In conclusion, the observed current reversal is determined by the large variation of the dissipation-induced phase lag ϕ_B similiar to the observations in the amplitude regime [17]. Therefore generalising the link between dissipation-induced symmetry breaking and current reversals, to the frequency domain.

To solidify the established link between symmetry breaking due to dissipation and the observed current reversal, the Hamiltonian limit and the overdamped regime were numerically investigated. For several exper-

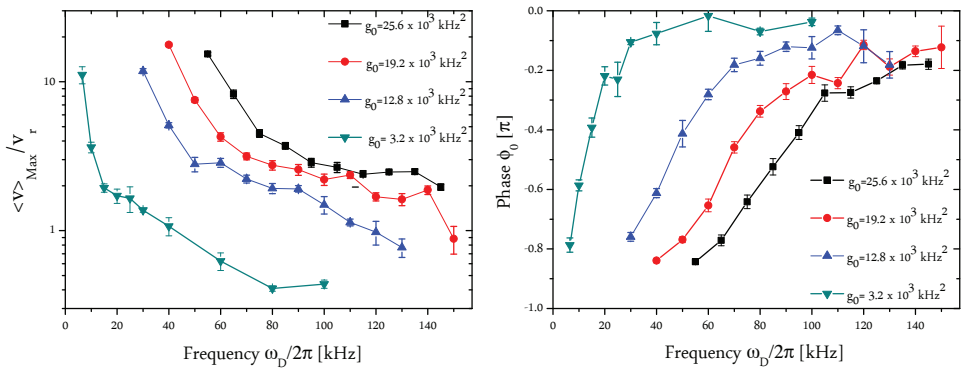

Figure 9.4: Ratchet Experiment results: amplitude and phase lag
Left: The amplitude fit parameter as derived from fitting data sets like the ones displayed in figure 9.2 with function (9.7) displayed over the driving frequency for 4 sets of different force amplitudes. The maximum current amplitude stays finite for all of the investigated parameters.
Right: The corresponding phase lag ϕ_0. The horizontal lines indicate a phase lag of $\phi_0 = -\pi/2$. At this value the initial current for the fixed biharmonic driving phase ϕ vanished and changed its sign.

imental reasons these regimes were not accessible with our apparatus. As with the numerical simulations in the amplitude regime [17], the results displayed in figure 9.5 were produced by David Cubero. In the Hamiltonian regime and in the overdamped regime the dissipation induced phase lag should be fixed by the symmetries of the system (Hamiltonian: $\phi_0 = 0$, overdamped: $\phi_0 = -\pi/2$), so that a variation in driving frequency should not produce a current reversal. Those two cases correspond to the left and right panels in figure 9.5 respectively. The middle panel is a simulation for parameters similar to the experiment. For moderate dissipation, a variation in the drive frequency produces a variation in the dissipation induced phase lag ϕ_0, resulting in a current reversal for a fixed driving phase of $\phi = \pi/2$. This cannot be observed in the Hamiltonian nor the overdamped regime. A variation in driving frequency results in a change in amplitude but not in a change in phase lag. The numerical simulations therefore confirm the validity of the link between current reversals in the frequency domain and dissipation-induced symmetry breaking.

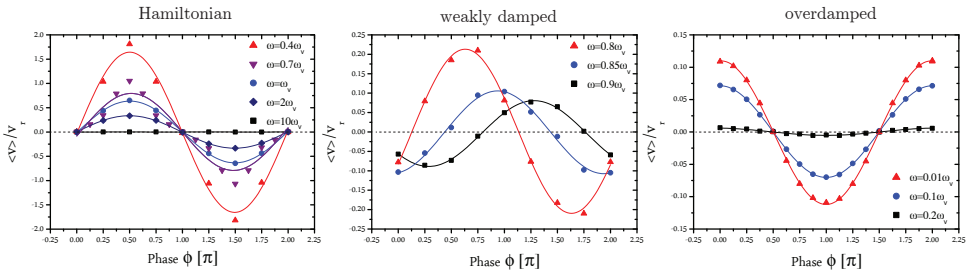

Figure 9.5: Average atomic velocity for different driving frequencies obtained by numerical simulation with $\omega_v = k\left(2U_0/m\right)^{1/2}$ and $A_1 = A_2 = 1$
Left: The Hamiltonian regime; no friction and therefore no noise ($\alpha = D = 0$). Driving force amplitude $F_0 = 0.2U_0k$, where U_0 is the depth of the confining potential.
Middle: The weakly damped regime. This regime corresponds to the experimental realisation and shows a current reversal for most driving phases ϕ with variation of the driving frequency. The simulation parameters are: driving force amplitude $F_0 = 0.2U_0k$, friction coefficient $\alpha = 0.15\alpha_0$ and noise strength $D = 1.994D_0$, with $\alpha_0 = mkv_0$, $D_0 = {\alpha_0}^2 v_0/k$ and $v_0 = \left(U_0/m\right)^{1/2}/10$.
Right: The overdamped regime. Simulation parameters are: $_0 = U_0k$, $\alpha = 100\alpha_0$ and $D = 1.944 \times 10^3 D_0$. The appearance of the *super-symmetry* fixes the phase lag to $\phi_0 = -\pi/2$, and no current reversal appears when varying the frequency of the biharmonic force.

9.4 Summary

The mechanism underlying the appearance of a current reversal with varying frequency of the biharmonic drive in a spatio-periodic ratchet system with ^{87}Rb atoms was investigated. The origin of the current reversal appears to be dissipation-induced symmetry breaking and is therefore not observed in the numerically simulated Hamiltonian and overdamped regime. This experimental study extends and generalises this link from previous work done in our group, which identified the same symmetry breaking mechanism as the origin of a different class of current reversals appearing when scanning the amplitude of the biharmonic force [17].

Chapter 10

Potential renormalization in an optical lattice

The experimental results of this chapter have been published in [103]: A. Wickenbrock, P. C. Holz, N. A. Abdul Wahab, P. Phoonthong, D. Cubero, and F. Renzoni. *Vibrational Mechanics in an Optical Lattice: Controlling Transport via Potential Renormalization.* Physical Review Letters 108, 020603 (2012).

10.1 Introduction

This chapter describes the second experiment conducted on the ^{87}Rb machine. For this experiment we worked with Philip Christoph Holz from the University of Augsburg, who also published the main results in his diploma thesis [42]. ^{87}Rb atoms were loaded into a 1D lin $\perp$ lin lattice, and an atomic current due to the ratchet effect was suppressed and revived as a function of the amplitude of an applied very high frequency phase modulation of one of the laser beams. Furthermore, the diffusion properties in an optical lattice driven by the high frequency modulation were investigated. For specific values of the applied modulation, the optical potential vanishes and leads to superdiffusion in the lattice. The ^{87}Rb atoms are not confined anymore along the lattice direction, while photon scattering still takes places. The effect of a high frequency oscil-

lating force on the response of a bistable system was recently investigated in [51]. It was shown that for an appropriate choice of the force amplitude the response of the system could be optimised. Similarly to *stochastic resonance* (see for example [26]), where a weak signal can be amplified by appropriate noise levels, this effect was termed *vibrational resonance*. It triggered several further publications (e.g. [7, 13]) and was also investigated theoretically in the context of transport phenomena in periodic potentials [8]. Since it is a very general effect, several interesting applications can be envisaged. Not just for the control of potentials where it was not possible before, for example in solid state physics, but also in the context of new measurement devices, where the response of a low frequency system can be used to measure the amplitude of an unknown high frequency signal [7].

To gain some intuition of this effect a brief introduction to the appearance of the potential normalization due to a high frequency signal is given before the theoretical treatment is presented. Then the experimental setup and the sequence will be discussed briefly before the experimental results are displayed. As in the previous chapter, numerical simulations by Dr. David Cubero, Seville, supported our results. The chapter ends with a brief summary.

10.1.1 Time-averaged high frequency phase modulation

The dipole force on a particle in a 1D optical potential can be written as:

$$F(z,t) = F_0 \cos\left[2kz - \alpha(t)\right], \tag{10.1}$$

where $F_0 = -2kU_0$ with U_0 the potential's depth, k the wavevector of the light, and $\alpha(t)$ an additional time-dependent phase factor for example by changing the optical pathlength of one of the beams. A phase change of $\alpha = 2\pi$ would result in a translation of the optical potential or the zero crossings of the dipole force by $\Delta z = \lambda/2$, or one lattice site. This can happen on several different time scales. If it happens slowly, an atom in the ground state of the trap follows the translation of the lattice. If the phase changes faster, the atom would exhibit a dynamical response

with excitations in higher energy states; it would start to oscillate. If the phase changes much faster than the atom can follow due to its inertia, then the force can be averaged.
If we presume a dynamically changing phase like:

$$\alpha(t) = \beta \sin \omega_{\mathrm{HF}} t, \tag{10.2}$$

with β the modulation index in radians and insert this into equation 10.1 the spatially dependent force becomes:

$$F(z,t) = F_0 \cos\left[2kz - \beta \sin \omega_{\mathrm{HF}} t\right]. \tag{10.3}$$

For a frequency ω_{HF} much bigger than any other frequency in the system, in the limit of $\omega_{\mathrm{HF}} \to \infty$, the particle will not react to the lattice shift at all due to its inertia but it will still experience an average of the oscillating force. The force on the atom averaged over one cycle of the fast oscillation can be written as:

$$\begin{aligned} \overline{F(z)} &= \frac{F_0 \omega_{\mathrm{HF}}}{2\pi} \int_0^{2\pi/\omega_{\mathrm{HF}}} dt \cos\left[2kz - \beta \sin \omega_{\mathrm{HF}} t\right] \\ &= F_0 J_0(\beta) \cos 2kz \\ &= F_{ave} \cos 2kz. \end{aligned} \tag{10.4}$$

So the time averaged force has the same spatial periodicity as the force with no phase modulation, but the amplitude is renormalized by the 0th order Bessel function[1]. The Bessel function as seen in figure 10.1 is an oscillating function with a decreasing amplitude. For the averaged or renormalized force this means that for certain modulation depths the amplitude becomes zero and then negative. The depths of the potential follows the Bessel function as well; if the force averages to zero, the potential disappears. Figure 10.1 displays the relations of the relevant quantities in a modulated optical lattice.

[1]Here we used the integral representation of the
0th order Bessel function: $J_0(x) = \frac{1}{2\pi} \int_0^{2\pi} \cos\left[-x \sin(\tau)\right] d\tau$.

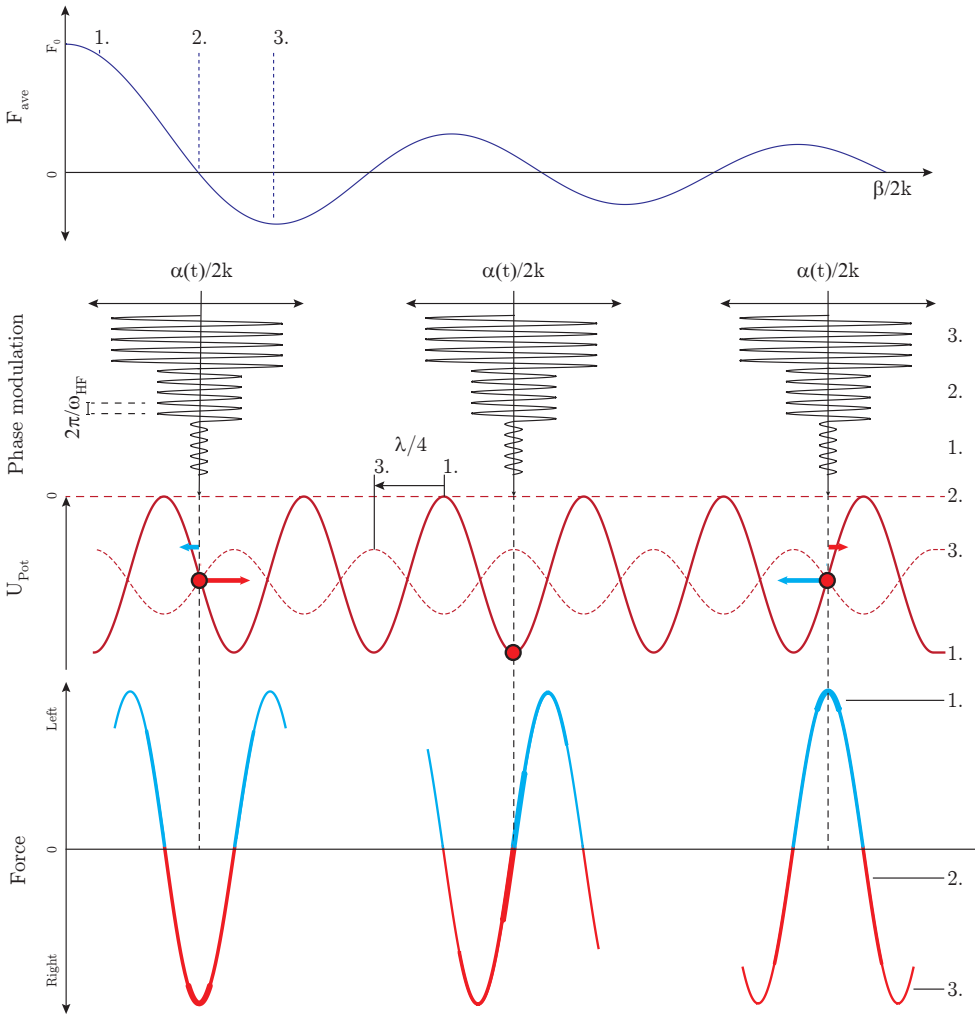

Figure 10.1: Detailed schematic describing the force averaging mechanism. The top shows the averaged force following the 0th order Bessel function over the modulation depths. A very fast phase modulation causes the potential to spatially move and the atom to experience different forces corresponding to the position of the atom for different times. The second row shows this translation of the lattice potential for the three amplitudes following a sinusoid with frequency ω_{HF}. The bottom shows the force experienced by the atom during one cycle of the phase modulation (the different modulation amplitudes are indicated by the line thickness). The integral over this curve results in the average force. Above the force the resulting potential can be seen. Three atoms are in the lattice, one at the maximum force to the right, one in the potential centre, and another at the position corresponding to the maximum force to the left. For small modulation (1) the potential does not change by much. The second modulation depths (2) makes the average force, and therefore the potential vanish since the amplitude corresponds to the first zero crossing of the Bessel function. The stronger 3rd modulation (3) reproduces the potential with roughly 40% of the intital potential depths. Interestingly the force is reversed and therefore the potential wells are shifted in space by $\lambda/4$.

10.2 Potential renormalization - Model and definitions

The treatment in the previous section should provide some insight into why the potential renormalization appears. An atom exploring a periodic potential on a very fast timescale effectively averages all spatial dependences. Whether the potential moves with respect to the atom or a force moves the atom with respect to the potential is therefore irrelevant; the relative oscillation is of importance. For the following treatment, in agreement with the ratchet effect literature, the system is transformed into the accelarated frame of the phase modulation. The phase modulation then appears as an oscillating force. A more rigorous description of the dynamics in a lin $\perp$ lin optical lattice loaded with atoms exhibiting a magnetic substructure ($J_g = 1/2 \rightarrow J_e = 3/2$) is given by the semiclassical Fokker-Planck equation [47]. The probability density $P_\pm(z, p, t)$ for each atom with mass m in the ground state sublevel $|\pm\rangle = |J_g = 1/2, M_g = \pm 1/2\rangle$ at position z and momentum p follows:

$$\left[\frac{\partial}{\partial t} + \frac{p}{m}\frac{\partial}{\partial z} - U'_\pm(z)\frac{\partial}{\partial p} + F(t)\frac{\partial}{\partial p}\right] P_\pm = -\gamma_\pm(z)P_\pm + \gamma_\mp(z)P_\mp + \frac{\partial^2}{\partial p^2}\left[D_\pm(z)P_\pm + L_\pm(z)P_\mp\right], \tag{10.5}$$

with $U'_\pm(z) = dU_\pm(z)/dz$ and

$$U_\pm(z) = \frac{U_0}{2}[-2 \pm \cos(2kz)] \tag{10.6}$$

is the optical potential for the respective groundstate $|\pm 1/2\rangle$ in the lin $\perp$ lin lattice generated by laser beams with wave vector k. $F(t)$ is a time-dependent driving force in the accelerated frame originating

from the phase modulation of the lattice beams.

$$\begin{aligned} \gamma_{\pm}(z) &= \frac{\Gamma'}{9}[1 \pm \cos(2kz)], \\ D_{\pm}(z) &= \frac{7\hbar^2 k^2 \Gamma'}{90}[5 \pm \cos(2kz)], \\ L_{\pm}(z) &= \frac{\hbar^2 k^2 \Gamma'}{90}[6 \mp \cos(2kz)]. \end{aligned} \tag{10.7}$$

$\gamma_{\pm}(z)$ is the spatially dependent transition rate between the ground state sublevels, with Γ' the photon scattering rate; $D_{\pm}(z)$ is a noise strength coefficient describing random momentum jumps as a result of photon interaction without ground state sublevel transitions; and $L_{\pm}(z)$ is related to random momentum jumps that appear in fluorescence cycles when the atom undergoes a transition between the atomic sublevels. The normalization condition for the probability density is given by:

$$\int \mathrm{d}z \int \mathrm{d}p \, [P_{-}(z,p,t) + P_{+}(z,p,t)] = 1. \tag{10.8}$$

The resulting force from the phase modulation can be written as:

$$F_{\mathrm{HF}}(t) = A_{\mathrm{HF}} \sin(\omega_{\mathrm{HF}} t + \phi_0). \tag{10.9}$$

To study the effect of a very large, very fast driving force on the atoms, formally the limit $\omega_{\mathrm{HF}} \to \infty$ is considered. For the force to have any effect the amplitude $A_{\mathrm{HF}} \to \infty$. Without other forces the atom would oscillate with frequency ω_{HF} following $z(t) = -r \sin(\omega_{\mathrm{HF}} t + \phi_0)$, where:

$$r = \frac{A_{\mathrm{HF}}}{m\omega_{\mathrm{HF}}^2}, \tag{10.10}$$

is the amplitude of the oscillation and indicates the potential forces the atom is experiencing during one cycle of the HF force. The relation to the phase modulation index β is given by:

$$r = \frac{\beta}{2k}. \tag{10.11}$$

Integrating, and therefore averaging, over one cycle of the HF force removes the high frequency components from the Fokker-Planck equation,

describing the dynamics in a renormalized Fokker-Planck equation with the following renormalized quantities:

$$\begin{aligned}
\bar{U}_{\pm}(\hat{z}) =& \frac{U_0}{2}[-2 \pm \mathrm{J}_0(2kr)\cos(2k\hat{z})], \\
\bar{\gamma}_{\pm}(\hat{z}) =& \frac{\Gamma'}{9}[1 \pm \mathrm{J}_0(2kr)\cos(2k\hat{z})], \\
\bar{D}_{\pm}(\hat{z}) =& \frac{7\hbar^2k^2\Gamma'}{90}[5 \pm \mathrm{J}_0(2kr)\cos(2k\hat{z})], \\
\bar{L}_{\pm}(\hat{z}) =& \frac{\hbar^2k^2\Gamma'}{90}[6 \mp \mathrm{J}_0(2kr)\cos(2k\hat{z})].
\end{aligned} \tag{10.12}$$

Where:

$$\mathrm{J}_0(2kr) = \frac{1}{2\pi}\int_0^{2\pi} \mathrm{d}\phi_0 \, \cos(2kr\sin\phi_0) \tag{10.13}$$

is the Bessel function of the first kind (compare figure 10.1). The renormalization by the HF field is formally correct in the limit $\omega_{\mathrm{HF}} \to \infty$ but it can also be seen as the lowest order of a multiple time-scale formalism using the expansion parameter $\epsilon = \omega/\omega_{\mathrm{HF}}$ [12].

10.3 Experimental Setup

To analyse the effect of the high frequency modulation on the dynamics of the atoms in the lattice, two experiments were conducted.
Firstly, we investigated how transport due to an applied biharmonic force is affected by the renomalisation of the potential.
Secondly, the diffusive motion of the atoms in the optical lattice was examined. The experimental setup for the lattice laser can be seen in 10.2. The lattice laser is injected by the master ECDL displayed in figure 8.4. The light from the slave laser is then split by a PBS cube and one arm is fed through the double pass EOM to enable the high frequency phase modulation. This light is diffracted through an AOM, which is not only used to shift the light to the right frequency ($\Delta = -13.5\Gamma$), but also to apply the biharmonic force via frequency modulating the AOM input. The other arm of the lattice is also shifted down by the same frequency with another AOM. First, the ratchet effect, clearly relying on a spatially periodic potential, was used to probe the lattice. Therefore an additional biharmonic force of the form:

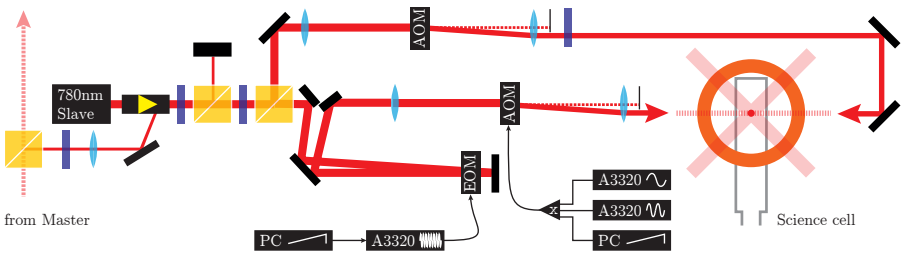

Figure 10.2: The lattice laser setup similar to figure 9.1 but with included double pass EOM. The EOM was modulated with a function generator[2] and the signal amplified in a home built high frequency, high gain amplifier (see 8.3). The modulation depth was controlled over the function generator's amplitude modulation input. The ramp was provided by the analogue computer control card and a MATLAB routine. The biharmonic force was produced by frequency modulating the AOM's input frequency in a similar way to chapter 9.

$$F(t) = F_0 \left[A_1 \cos(\omega_D t) + A_2 \cos(2\omega_D t + \phi) \right], \tag{10.14}$$

was applied via frequency modulation of one of the AOMs. Renormalizing the lattice potential by applying the HF field should enable us to control the transport through the lattice. The experimental sequence for the experiment is shown in table 10.1.

Experimental Sequence	MOT Loading	LVIS off/ Comp.	Molasses	Load Lattice	HF ramp	BH ramp	BH drive	Image	Delay	Background
						Diffusion study: HF drive: 1−16 ms				
Time [ms]	2000	50	8	1	1	4	5	4	50	4
MOT beams										
LVIS switch										
B-field MOT	$20\frac{G}{cm}$	$40\frac{G}{cm}$								
Lattice switch										
Mod. Trig. HF										
Mod. Index HF					ramp	full	full			
Mod. Trig. BH	OFF during DIFFUSION STUDY									
Mod. Index BH	OFF during DIFFUSION STUDY					ramp	full			
Camera trigger										

Table 10.1: The experimental control sequence for the study of transport suppression and diffusion in a high frequency modulated lattice. For the diffusion study no biharmonic drive was applied. Instead the drive time of the high frequency modulation was varied between $1 - 16\,ms$.

10.4 Transport control via high frequency modulation

For the directed transport study, ^{87}Rb atoms were loaded from the LVIS into the science MOT, then compressed for 50 ms and further cooled in an 8 ms optical molasses phase. After switching all the MOT beams off, the lattice beam is turned on. In this configuration it took about 1 ms to localise the atoms in the optical lattice. Then the high frequency phase modulation was ramped up in 1 ms, from no phase modulation to the final value A_{HF} which was then changed for different experiments. For each value of the final amplitude A_{HF} of the HF-modulation a whole sine curve following:

$$\langle v \rangle (\phi) = v_{\max} \sin (\phi - \phi_0) , \tag{10.15}$$

was taken according to chapter 9. For the driving parameters in this experiment the dissipation induced phaselag ϕ_0 was very small. The biharmonic force was ramped up linearly in 4 ms and kept at full drive for another 5ms. Then, to measure the ensemble average position, a first fluorescence image was taken and after 50 ms a second without atoms, which was then subtracted from the first as the background. The resulting images were fitted with a 2D gaussian. To derive the velocity for a given phase the full drive time of the biharmonic force was varied and the results fitted with a linear function, the slope of which corresponds to the velocity v of the atomic current for the biharmonic phase ϕ. After spending some time optimising the procedure with respect to switching effects of both the HF-field as well as the biharmonic drive, we started varying the strength of the applied fast oscillation.

A standard data set showing the characteristic $\sin (\phi - \phi_0)$ behaviour for different applied HF-modulations can be seen in figure 10.4 (with the experimental parameters in its caption). For no applied high frequency modulation, transport of the atomic cloud appears due to the ratchet effect as a function of the phase of the biharmonic drive. But for increasing values of the HF-drive, the current amplitude decreases, vanishes completely and then reappears.

The full picture can be seen in figure 10.4, which displays the maximum atomic current from fitting each data set with a sine according

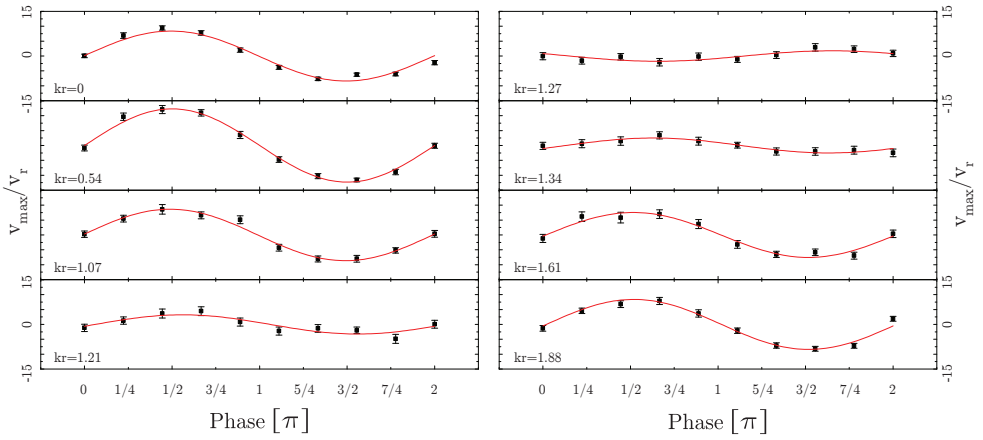

Figure 10.3: Transport data as a function of the phase ϕ of the biharmonic drive for different amplitudes of the applied HF-frequency. For no HF-modulation the data follows clearly the expected sine like behaviour (compare equation (10.15)) with a negligible phase lag ϕ_0. Increasing the amplitude of the modulation the current first disappears and then reappears as expected by the behaviour of the Bessel function. Also, visible in the second panel is an initial increase in sine amplitude. This could be attributed to a superimposed resonance, when the renormalized lattice frequency matches the applied biharmonic drive. The experimental parameters are the same as in figure 10.4 for the highest HF drive of $\omega_{\mathrm{HF}} = 8.8 \times 10^6\,\mathrm{rad/s}$.

to (10.15). Each point represents $v_{\max}$ for a different driving amplitude expressed over the modulation depth $\beta/2$ in units of kr. The modulation depth with the EOM was varied from minimum zero to a maximum of $\beta/2 = 6.04\mathrm{rad}$, which was limited by the maximum voltage applicable to the EOM and EOM driver. The experiment was repeated for three sets of data with different applied high frequencies. Due to the bandwidth limitations we had to restrict the investigation to a maximum ratio $\omega_{\mathrm{HF}}/\omega_v \approx 10$. For all used HF frequencies the same behaviour could be observed. For zeros of the Bessel function the current due to the ratchet effect dissappears. For local maxima of the absolute of the Bessel function the current was revived. The findings were supported by numerical simulations by David Cubero. They are visible in figure 10.4 on the left in comparison with the experimental data on the right. Cubero's simulations fill the void left due to the bandwidth limitations of the EOM and allow us to observe the results for $\omega_{\mathrm{HF}} \to \infty$ and for the finite ratio $\omega_{\mathrm{HF}}/\omega_v = 20$. The qualitative behaviour of the potential renormalization due to the high frequency phase modulation is well preserved also for finite frequency ratios. In addition we observed, in theory

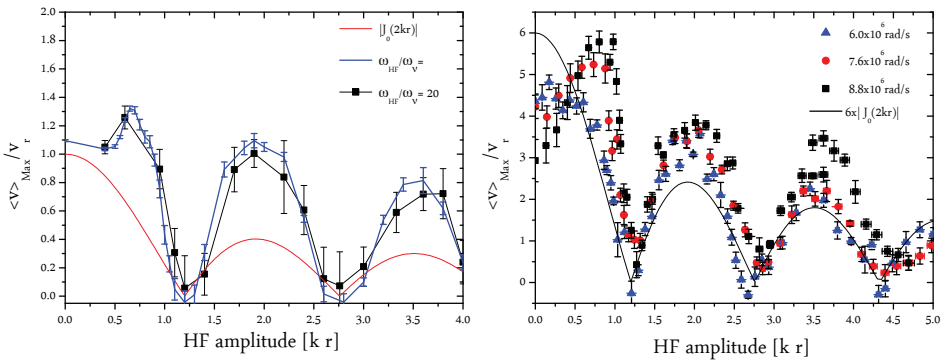

Figure 10.4: Theoretical and experimental results for the average atomic current $\langle v \rangle_{\max}$ through the optical lattice generated by a biharmonic drive. Both results follow the normalized potential indicated by the zeroth order Bessel function $|J_0(2kr)|$.
Left: The numerical results as obtained from Monte Carlo simulations by David Cubero, Seville. The average particle current $v_{\max}$ in units of the recoil velocity v_r as a function of the high frequency modulation amplitude $\beta/2$ in rad. The parameters of the biharmonic drive (equation (10.14)) are ratio $A_1 = A_2 = 1$, force amplitude $F_0 = 140\hbar k\omega_v$ and driving frequency $\omega = \omega_r$. The simulations were repeated in two different scenarios. First, in the limit $\omega_{\mathrm{HF}} \to \infty$ (blue) and then with a finite driving frequency of $\omega_{\mathrm{HF}} = 20\omega_v$. The scattering rate in both cases was $\Gamma' = 10\omega_r$.
Right: The experimental results. The maximum current as derived from fits of data (compare figure 10.4) displayed as a function of the applied modulation. The experiment was repeated for three different HF-frequencies $\omega_{\mathrm{HF}} = (6.0, 7.6, 8.8) \times 10^6\,\mathrm{rad/s}$ corresponding to $\omega_{\mathrm{HF}}/\omega_v = (6.7 \pm 0.7)$ with $\omega_v = (0.9 \pm 0.1) \times 10^5\,\mathrm{rad/s}$. The other biharmonic force parameters are $A_1 = 1, A_2 = 2$, driving frequency $\omega_D = 0.9 \times 10^4\,\mathrm{rad/s}$ and driving force amplitude $F_0 = 112\hbar k\omega_r$.
Both plots contain an amplitude adjusted Bessel function as a guide for the eye.

as well as in the experimental data, an atomic current maximum (around $\beta/2 \approx 0.75\mathrm{rad}$) before the first zero of the Bessel function. We attribute this to a superimposed resonance corresponding to frequency matching of the biharmonic drive frequency and the renormalized vibrational frequency of the lattice for this driving strength.

10.5 Periodic superdiffusion due to high frequency modulation

To analyze the effect of the high frequency modulation further, we investigated the diffusion properties in the optical lattice. The relevant

quantity would be the diffussion exponent α defined by:

$$\left\langle z^2(t)\right\rangle - \left\langle z(t)\right\rangle^2 \propto t^{\alpha} \tag{10.16}$$

in the limit of $t \to \infty$. According to this definition $\alpha = 1$ corresponds to normal diffusion, in a deep optical lattice for example, while $\alpha \neq 1$ characterises anomalous diffusion. We are especially interested in superdiffusion encountered when $\alpha > 1$. The appearance of superdiffusion in optical lattices below a critical potential depth $U_{0,\mathrm{crit}} \sim 100\, E_r$ is well established [41, 48, 58], with α depending on the potential depth explicitly. So when renormalizing the potential depth, we should expect superdiffusion for shallow potentials.

The experimental sequence is basically the same as that shown in table 10.1 except that the biharmonic drive is not applied (as indicated in the table). ^{87}Rb atoms were loaded into the lattice, then the high frequency modulation was ramped up and driven at full amplitude for a various amount of time within an interval of 1 to 16 ms. Then the width of the cloud was determined by taking a fluorescence image, subtracting the background picture and fitting a 2D Gaussian to the result. The temporal range of the experiment is limited due to atom loss from the optical lattice, most dramatically for those HF-modulations where the potential disappears. But the atom losses were also due to the lack of confinement perpendicular to the lattice beam propagation axis independent of the modulation depths, since these directions include the gravity axis. So for longer times atoms were simply falling out of the lattice. Such a short temporal range is not suitable to measure the exponent of the diffusion directly. In our investigation we determined the width of the cloud for different modulation times and fitted a straight line to it. An effective diffusion coefficient D was derived from fitting the data according to $\left\langle z^2(t)\right\rangle - \left\langle z(t)\right\rangle^2 = 2Dt$. Superdiffusion clearly leads to an increase of the effective diffusion coefficient. Latest when the renormalized potential depths goes below the critical value $U_{0,\mathrm{crit}}$ for the onset of superdiffusion the width of the cloud should increase much faster than without the modulation. Further modifications arise from the fact that the renormalized lattice differs from a conventional lattice in the sense that, normally, a reduction in potential depths for the same

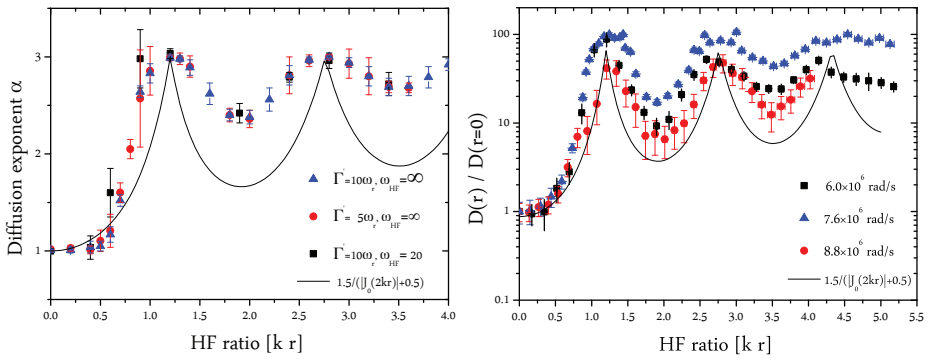

Figure 10.5: Theoretical and experimental results for the diffusion exponent and the effective diffusion coefficient. Both graphs show cleary the same periodicity as the Bessel function, with maxima in the respective diffusion measure corresponding to $J_0(2kr) = 0$.
Left: The numerical results. The diffusion exponent α as a function of the applied HF-driving for an optical lattice with an initial depth of $U_{0,\mathrm{crit}} = 200E_r$ as obtained by stochastic simulations. The results were repeated for two different scattering rates $\Gamma' = 5, 10\omega_r$ (with ω_r the recoil frequency) in the limit $\omega_{\mathrm{HF}} \to \infty$ and for one scattering rate $\Gamma' = 10\omega_r$ for a finite ratio $\omega_{\mathrm{HF}}/\omega_v = 20$. The black line is a function with the same periodicity as the Bessel function as orientation.
Right: The experimental results. The effective diffusion coefficient is displayed as function of the different driving strength in a log plot for three different values of the HF-driving frequency ω_{HF}. The data are rescaled by the effective diffusion coefficient of the undriven lattice which was between $1.5\lambda^2/\mu s$ and $7.5\lambda^2/\mu s$. The vibrational frequency was derived from beam-size and power measurements to $\omega_v = (9 \pm 1) \times 10^5 rad/s$, the ratio $\omega_{\mathrm{HF}}/\omega_v$ is therefore (6.7 ± 0.7), (8.4 ± 0.9) and (9.8 ± 1.1) respectively. The function plotted in black is again an inverted Bessel function as orientation (not in log scale).

detuning Δ always comes with a reduction in the photon scattering rate and therefore also in the quantities $\gamma_\pm(\hat{z})$, $D_\pm(\hat{z})$ and $L_\pm(\hat{z})$. This is in contrast to a renormalized potential. When it vanishes, the photon scattering rate just becomes spatially flat and stays constant with the same average. The potential disappears while scattering still takes place. The experimental results can be seen in figure 10.5 on the right. For the same HF-frequencies as in the directed transport study, the effective diffussion coefficient is displayed as a function of the applied HF-amplitude on the right. On the left are the numerical results produced by David Cubero. In contrast to our experiment he was not limited to an effective diffusion coefficient D and could investigate the diffussion exponent α directly. For values of the HF-drive where the Bessel function is zero,

the diffussion exponent is clearly above 1 indicating superdiffusion, but it is also clearly above the exponent for ballistic expansion $\alpha = 2$. The expansion of the cloud is accelerating due to the mentioned ongoing photon scattering. Both measures in theory and experiment reproduce the characteristic periodicity of the Bessel function in the respective diffusion constant, indicating the renormalization of the potential due to the application of the HF-modulation.

10.6 Summary

The work in this chapter demonstrated experimentally the phenomenon of vibrational resonance in a dissipative optical lattice with ^{87}Rb atoms. Numerical simulations supported and generalised our results. Applying a strong oscillating force, generated by phase modulating one of the laser beams with a frequency much larger than any other in the system (esp. the vibrational frequency ω_v), renormalizes the potential and all other spatially depending variables in the relevant Fokker-Planck equation. The process can be understood as an averaging effect of the atom, which explores different regions of the potential during an HF-cycle. Since by definition all the other frequencies are much smaller, the atom has no time to react and "sees" a renormalized potential. The disappearance and reappearance of the potential was shown in two different ways. Firstly using the ratchet effect as probe: current generation in a biharmonically driven lattice relies on a potential, so when the potential disappears the current ceases. Secondly by investigating an effective diffusion coefficient. Without confinement along the axis of the lattice but with a spatially "flat" scattering rate, the atom's expansion is superdiffusive, whenever the renormalized potential becomes shallow enough.

Chapter 11

Summary of the ^{87}Rb experiment

While this thesis is being written, the laser system of the ^{87}Rb experiment is being changed to provide more power. More power enables us to increase the beam size. And a bigger beam size means more atoms. The number of atoms in the science MOT was one of the main limiting factor so far not to reach the ulta cold regime at UCL. The new vacuum chamber constructed and build within this thesis provides an UHV system with a pressure enabling trapping times above 100s. This will enable future experiments with large atom numbers and dense atomic samples. But even before reaching the quantum regime, there are several interesting experiments to consider. But let us start with a brief summary of the experimental work. Two experiments were conducted on this machine. Both were, in good tradition of this group, related to transport phenomena in optical lattices. The ratchet effect describes directed transport in a system out of equilibrium without an obvious bias. This involves symmetry breaking. The probability for transport to the left needs to be larger than to the right or vice versa. Since the potential follows a sinusoid and is therefore symmetric, the symmetry breaking originates from either the temporal driving force or from spontaneous symmetry breaking mechanisms. Current reversals of the atomic transport with varying one of the parameters is at the heart of the understanding of the underlying processes. The first experiment investigated a current reversal which appears as a function of the biharmonic drive frequency in a

dissipative optical lattice. Supported by numerical simulations we could relate the appearance of the current reversal to a dissipation induced phase shift. This was done before for a similar but not identical current reversal, which appears when increasing the amplitude of the biharmonic force. Thus the class of current reversals due to dissipation induced symmetry breaking was extended.

The second experiment also investigated transport phenomena in optical lattices. But instead of the ratchet effect being at the center of interest, it was merely used as a probe. This work researched an effect termed *vibrational resonance*. The response of a nonlinear system can be optimized or controlled by applying a very high frequency force. This means for an optical potential, that the potential depth becomes a function of the applied HF-drive amplitude. With ^{87}Rb atoms loaded into an dissipative optical lattice and driven by a biharmonic force we first produced directed current and investigated then its behaviour as a function of the applied HF-amplitude. As predicted by the theory, the current follows the Bessel function of the drive amplitude. When the renormalized potential vanishes no directed current can be produced. Increasing the drive amplitude further revived the current and therefore the potential. As a second part of this experiment we investigated the atomic diffusion in the lattice with HF-drive. When the confinment along the beam axis dissappears, superdiffusion should become apparent. We observed this while studying the width of the atomic cloud as a function of the HF-drive time. For zeros of the Bessel function, the size of the cloud "exploded". Those results were again supported and extended by numerical calculations.

Chapter 12

Outlook

The next steps for the ^{87}Rb experiment certainly involve reaching the ultra-cold regime and producing the first BEC at UCL. The future of the ^{133}Cs experiment is less clear, though several interesting paths are open for exploration. The coupling increase due to the degenerate higher-order transverse modes might enable new cavity geometries, with coupling constants not realized so far with cold atoms. The super-strong coupling regime [64] is reached when the coupling constant becomes comparable to the FSR of the resonator. In this case the light of the cavity and the ensemble of atoms are already strongly coupled within one round trip of the cavity. This is a qualitatively new regime and to achieve it in a comparably large cavity by adding more and more transverse modes would be a new approach to get there. As mentioned in the introduction, the initial motivation for the ^{133}Cs machine was to research cavity cooling. In collaboration with Michal Hemmerling and Gordon Robb from the University of Strathclyde, Glasgow, we are currently simulating the dynamics of a cloud of cold atoms within the cavity as they are illuminated perpendicular to the cavity axis with a laser beam. This is the initial configuration where cavity-related cooling effects were observed [14]. Even though no temperature reduction was measured, we were able to observe super-radiant emission into the cavity at pump-atom detunings of $\Delta/(2\pi) < -1000\,\mathrm{MHz}$. The light scattered into the cavity by the ensemble increased non-linearly with the atom number in the cavity suggesting collective self-organization processes, which in itself would already be interesting to investigate. One aim would be to achieve

quantitative agreement between the numerical simulations and the observed scattering into the cavity, in terms of threshold behaviour and scaling with the atom number. For this, the measurement of the collective coupling constant, via normal mode splitting spectroscopy, provides a convenient way to calibrate the effective coupled atom number.

Bibliography

[1] Spontaneous emission probabilities at radio frequencies. *Proceedings of the American Physical Society*, 69:674–674, Jun 1946.

[2] A. M. Abdel-Hafez. Degenerate and nondegenerate two-mode normal squeezing in a two-level atom and two-mode system. *Phys. Rev. A*, 45:6610–6614, May 1992.

[3] G. S. Agarwal. Vacuum-field Rabi splittings in microwave absorption by Rydberg atoms in a cavity. *Phys. Rev. Lett.*, 53:1732–1734, Oct 1984.

[4] H. C. W. Beijerinck. Rigorous calculation of heating in alkali-metal traps by background gas collisions. *Phys. Rev. A*, 61:033606, Feb 2000.

[5] A. T. Black. *Collective Atom-Light Interactions applied to Laser Cooling and Optical Communication*. PhD thesis, Stanford University, 2005.

[6] E. D. Black. An introduction to pound–drever–hall laser frequency stabilization. *American Journal of Physics*, 69(1):79–87, 2001.

[7] M. Borromeo and F. Marchesoni. Mobility oscillations in high-frequency modulated devices. *EPL (Europhysics Letters)*, 72(3):362, 2005.

[8] M. Borromeo and F. Marchesoni. Vibrational ratchets. *Phys. Rev. E*, 73:016142, Jan 2006.

[9] F. Brennecke, T. Donner, S. R. T. Bourdel, M. Köhl, and Esslinger. Cavity QED with a Bose-Einstein condensate. *Nature*, 450(7167):268, 11 2007.

[10] M. Brown. *Monte Carlo simulations of cold atom ratchets*. PhD thesis, University College London, 2008.

[11] M. Brune, F. Schmidt-Kaler, A. Maali, J. Dreyer, E. Hagley, J. M. Raimond, and S. Haroche. Quantum Rabi oscillation: A direct test of field quantization in a cavity. *Phys. Rev. Lett.*, 76:1800–1803, Mar 1996.

[12] J. Casado-Pascual. Effect of a high-frequency magnetic field on the resonant behavior displayed by a spin-1/2 particle under the influence of a rotating magnetic field. *Chemical Physics*, 375(23):170 – 179, 2010. Stochastic processes in Physics and Chemistry.

[13] J. Casado-Pascual and J. P. Baltanás. Effects of additive noise on vibrational resonance in a bistable system. *Phys. Rev. E*, 69:046108, Apr 2004.

[14] H. W. Chan, A. T. Black, and V. Vuletić. Observation of collective-emission-induced cooling of atoms in an optical cavity. *Phys. Rev. Lett.*, 90:063003, Feb 2003.

[15] H. W. P. Chan. *Cavity Cooling of Cesium Atoms*. PhD thesis, Stanford University, 2003.

[16] S. Chu, L. Hollberg, J. E. Bjorkholm, A. Cable, and A. Ashkin. Three-dimensional viscous confinement and cooling of atoms by resonance radiation pressure. *Phys. Rev. Lett.*, 55:48–51, Jul 1985.

[17] D. Cubero, V. Lebedev, and F. Renzoni. Current reversals in a rocking ratchet: Dynamical versus symmetry-breaking mechanisms. *Phys. Rev. E*, 82:041116, Oct 2010.

[18] J. Dalibard and C. Cohen-Tannoudji. Laser cooling below the doppler limit by polarization gradients: simple theoretical models. *J. Opt. Soc. Am. B*, 6(11):2023–2045, Nov 1989.

[19] M. de Labachelerie and G. Passedat. Mode-hop suppression of littrow grating-tuned lasers. *Appl. Opt.*, 32(3):269–274, Jan 1993.

[20] R. H. Dicke. Coherence in spontaneous radiation processes. *Phys. Rev.*, 93:99–110, Jan 1954.

[21] P. Domokos and H. Ritsch. Mechanical effects of light in optical resonators. *J. Opt. Soc. Am. B*, 20(5):1098–1130, May 2003.

[22] P. J. Douglas. *Atomic dynamics in optical traps: experiments with caesium atoms*. PhD thesis, University College London, 2009.

[23] R. Feynman, R. Leighton, and M. Sands. *The Feynman Lectures on Physics: Mainly mechanics, radiation, and heat*. Addison-Wesley world student series. Addison-Wesley, 1963.

[24] S. Flach, O. Yevtushenko, and Y. Zolotaryuk. Directed current due to broken time-space symmetry. *Phys. Rev. Lett.*, 84:2358–2361, Mar 2000.

[25] C. J. Foot. *Atomic Physics*. Oxford University Press, Oxford, 2009.

[26] L. Gammaitoni, P. Hänggi, P. Jung, and F. Marchesoni. Stochastic resonance. *Rev. Mod. Phys.*, 70:223–287, Jan 1998.

[27] R. Gommers. *Symmetry and transport in cold atom ratchets*. PhD thesis, University College London, 2007.

[28] R. Gommers, S. Bergamini, and F. Renzoni. Dissipation-induced symmetry breaking in a driven optical lattice. *Phys. Rev. Lett.*, 95:073003, Aug 2005.

[29] R. Gommers, M. Brown, and F. Renzoni. Symmetry and transport in a cold atom ratchet with multifrequency driving. *Physical Review A*, 75(5):1–6, 2007.

[30] R. Gommers, S. Denisov, and F. Renzoni. Quasiperiodically driven ratchets for cold atoms. *Phys. Rev. Lett.*, 96:240604, Jun 2006.

[31] R. Gommers, P. Douglas, S. Bergamini, M. Goonasekera, P. H. Jones, and F. Renzoni. Resonant activation in a nonadiabatically driven optical lattice. *Phys. Rev. Lett.*, 94:143001, Apr 2005.

[32] R. Gommers, V. Lebedev, M. Brown, and F. Renzoni. Gating ratchet for cold atoms. *Phys. Rev. Lett.*, 100:040603, Jan 2008.

[33] S.-C. Gou. Quantum behavior of a two-level atom interacting with two modes of light in a cavity. *Phys. Rev. A*, 40:5116–5128, Nov 1989.

[34] J. Gripp and L. A. Orozco. Evolution of the vacuum Rabi peaks in a many-atom system. *Quantum and Semiclassical Optics: Journal of the European Optical Society Part B*, 8(4):823, 1996.

[35] P. Hänggi and F. Marchesoni. Artificial brownian motors: Controlling transport on the nanoscale. *Rev. Mod. Phys.*, 81:387–442, Mar 2009.

[36] G. Hechenblaikner, M. Gangl, P. Horak, and H. Ritsch. Cooling an atom in a weakly driven high-q cavity. *Phys. Rev. A*, 58:3030–3042, Oct 1998.

[37] E. Hecht. *Optics (4th Edition)*. Addison Wesley, 4 edition, August 2001.

[38] D. J. Heinzen, J. J. Childs, J. E. Thomas, and M. S. Feld. Enhanced and inhibited visible spontaneous emission by atoms in a confocal resonator. *Phys. Rev. Lett.*, 58:1320–1323, Mar 1987.

[39] M. Hemmerling. *Collective Dynamics of Cold Atoms in Optical Cavities*. PhD thesis, University of Strathclyde, 2010.

[40] T. Hänsch and A. Schawlow. Cooling of gases by laser radiation. *Optics Communications*, 13(1):68 – 69, 1975.

[41] T. W. Hodapp, C. Gerz, C. Furtlehner, C. I. Westbrook, W. D. Phillips, and J. Dalibard. Three-dimensional spatial diffusion in optical molasses. *Applied Physics B: Lasers and Optics*, 60:135–143, 1995. 10.1007/BF01135855.

[42] P. C. Holz. Renormalisation of an optical lattice by high frequency modulation. Master's thesis, University of Augsburg, 2012.

[43] R. G. Hulet, E. S. Hilfer, and D. Kleppner. Inhibited spontaneous emission by a rydberg atom. *Phys. Rev. Lett.*, 55(20):2137–2140, Nov 1985.

[44] E. T. Jaynes and F. W. Cummings. Comparison of quantum and semiclassical radiation theories with application to the beam maser. *Proceedings of the IEEE*, 51(1):89–109, June 2005.

[45] W. Jhe, A. Anderson, E. A. Hinds, D. Meschede, L. Moi, and S. Haroche. Suppression of spontaneous decay at optical frequencies: Test of vacuum-field anisotropy in confined space. *Phys. Rev. Lett.*, 58:666–669, Feb 1987.

[46] P. H. Jones, M. Goonasekera, and F. Renzoni. Rectifying fluctuations in an optical lattice. *Phys. Rev. Lett.*, 93:073904, Aug 2004.

[47] K. I. Petsas, G. Grynberg, and J.-Y. Courtois. Semiclassical monte carlo approaches for realistic atoms in optical lattices. *Eur. Phys. J. D*, 6(1):29–47, 1999.

[48] H. Katori, S. Schlipf, and H. Walther. Anomalous dynamics of a single ion in an optical lattice. *Phys. Rev. Lett.*, 79:2221–2224, Sep 1997.

[49] J. Klinner. *Experiments with Ultra-Cold Atomic Ensembles in Optical Resonators with Ultra-High Finesse and Narrow linewidth.* PhD thesis, University of Hamburg, 2009.

[50] W. K. Lai, V. Buek, and P. L. Knight. Dynamics of a three-level atom in a two-mode squeezed vacuum. *Phys. Rev. A*, 44:6043–6056, Nov 1991.

[51] P. S. Landa and P. V. E. McClintock. Vibrational resonance. *Journal of Physics A: Mathematical and General*, 33(45):L433, 2000.

[52] V. Lebedev. *AC driven ratchets for cold atoms: beyond 1D rocking ratchets.* PhD thesis, University College London, 2010.

[53] P. Lebedew. Untersuchungen über die Druckkräfte des Lichtes. *Annalen der Physik*, 311(11):433–458, 1901.

[54] S. Leslie, N. Shenvi, K. R. Brown, D. M. Stamper-Kurn, and K. B. Whaley. Transmission spectrum of an optical cavity containing n atoms. *Phys. Rev. A*, 69(4):043805, Apr 2004.

[55] B. L. Lev, A. Vukics, E. R. Hudson, B. C. Sawyer, P. Domokos, H. Ritsch, and J. Ye. Prospects for the cavity-assisted laser cooling of molecules. *Phys. Rev. A*, 77(2):023402, Feb 2008.

[56] M. Lewenstein and L. Roso. Cooling of atoms in colored vacua. *Phys. Rev. A*, 47:3385–3389, Apr 1993.

[57] D. Luchinsky, M. Greenall, and P. McClintock. Resonant rectification of fluctuations in a brownian ratchet. *Physics Letters A*, 273(56):316 – 321, 2000.

[58] S. Marksteiner, K. Ellinger, and P. Zoller. Anomalous diffusion and lévy walks in optical lattices. *Phys. Rev. A*, 53:3409–3430, May 1996.

[59] J. L. Mateos. Chaotic transport and current reversal in deterministic ratchets. *Phys. Rev. Lett.*, 84:258–261, Jan 2000.

[60] P. Maunz, T. Puppe, I. Schuster, N. Syassen, P. W. H. Pinkse, and G. Rempe. Cavity cooling of a single atom. *Nature*, 428:50, 3 2004.

[61] P. Maunz, T. Puppe, I. Schuster, N. Syassen, P. W. H. Pinkse, and G. Rempe. Normal-mode spectroscopy of a single-bound-atom-cavity system. *Phys. Rev. Lett.*, 94(3):033002, Jan 2005.

[62] P. L. W. Maunz. *Cavity cooling and spectroscopy of a bound atom-cavity system.* PhD thesis, Technische Universit¨at M¨unchen, MPQ, 2005.

[63] J. C. Maxwell. *A treatise on electricity and magnetism.* Clarendon Press, Oxford :, 1873.

[64] D. Meiser and P. Meystre. Superstrong coupling regime of cavity quantum electrodynamics. *Phys. Rev. A*, 74:065801, Dec 2006.

[65] H. J. Metcalf and P. van der Straten. *Laser cooling and trapping.* Springer Verlag, New York, 1999.

[66] P. Meystre. V cavity quantum optics and the quantum measurement process. volume 30 of *Progress in Optics*, pages 261 – 355. Elsevier, 1992.

[67] A. Millett-Sikking, I. G. Hughes, P. Tierney, and S. L. Cornish. Davll lineshapes in atomic rubidium. *Journal of Physics B: Atomic, Molecular and Optical Physics*, 40(1):187, 2007.

[68] T. W. Mossberg, M. Lewenstein, and D. J. Gauthier. Trapping and cooling of atoms in a vacuum perturbed in a frequency-dependent manner. *Phys. Rev. Lett.*, 67:1723–1726, Sep 1991.

[69] H. Müller. Fast high-voltage amplifiers for driving electro-optic modulators. *Review of Scientific Instruments*, 76(8):084701, 2005.

[70] B. Nagorny. *Dynamik kalter Atome in der Stehwellendipolfalle eines Ringresonators hoher Güte*. PhD thesis, Universität Hamburg, 2003.

[71] M. Notcutt, L.-S. Ma, J. Ye, and J. L. Hall. Simple and compact 1-hz laser system via an improved mounting configuration of a reference cavity. *Opt. Lett.*, 30(14):1815–1817, Jul 2005.

[72] Y. B. Ovchinnikov. Compact magneto-optical sources of slow atoms. *Optics Communications*, 249(46):473 – 481, 2005.

[73] A. S. Parkins. Resonance fluorescence of a two-level atom in a two-mode squeezed vacuum. *Phys. Rev. A*, 42:6873–6883, Dec 1990.

[74] T. Pellizzari, S. A. Gardiner, J. I. Cirac, and P. Zoller. Decoherence, continuous observation, and quantum computing: A cavity qed model. *Phys. Rev. Lett.*, 75:3788–3791, Nov 1995.

[75] W. D. Phillips. Nobel lecture: Laser cooling and trapping of neutral atoms. *Rev. Mod. Phys.*, 70:721–741, Jul 1998.

[76] W. D. Phillips, P. L. Gould, and P. D. Lett. Cooling, stopping, and trapping atoms. *Science*, 239(4842):877–883, 1988.

[77] P. Phoonthong. *State-Insensitive Traps for Caesium Atoms*. PhD thesis, University College London, 2011.

[78] N. R. Quintero, J. A. Cuesta, and R. Alvarez-Nodarse. Symmetries shape the current in ratchets induced by a biharmonic driving force. *Phys. Rev. E*, 81:030102, Mar 2010.

[79] E. L. Raab, M. Prentiss, A. Cable, S. Chu, and D. E. Pritchard. Trapping of neutral sodium atoms with radiation pressure. *Phys. Rev. Lett.*, 59:2631–2634, Dec 1987.

[80] M. G. Raizen, R. J. Thompson, R. J. Brecha, H. J. Kimble, and H. J. Carmichael. Normal-mode splitting and linewidth averaging for two-state atoms in an optical cavity. *Phys. Rev. Lett.*, 63(3):240–243, Jul 1989.

[81] P. Reimann. Brownian motors: noisy transport far from equilibrium. *Physics Reports*, 361(24):57 – 265, 2002.

[82] L. Ricci, M. Weidemüller, T. Esslinger, A. Hemmerich, C. Zimmermann, V. Vuletic, W. König, and T. Hänsch. A compact grating-stabilized diode laser system for atomic physics. *Optics Communications*, 117(56):541 – 549, 1995.

[83] G. Ritt, G. Cennini, C. Geckeler, and M. Weitz. Laser frequency offset locking using a side of filter technique. *Applied Physics B: Lasers and Optics*, 79:363–365, 2004. 10.1007/s00340-004-1559-6.

[84] T. Salger, S. Kling, T. Hecking, C. Geckeler, L. Morales-Molina, and M. Weitz. Directed transport of atoms in a hamiltonian quantum ratchet. *Science*, 326(5957):1241–1243, 2009.

[85] J. Seke. Extended Jaynes-Cummings model in a damped cavity. *J. Opt. Soc. Am. B*, 2(10):1687–1689, Oct 1985.

[86] B. Shore and P. Knight. The jaynes-cummings model. *Journal of Modern Optics*, 40(7):1195–1238, 1993.

[87] D. A. Steck. Cesium D line data. *available online at http://steck.us/alkalidata*, revision 2.0.1,, May 2008.

[88] D. A. Steck. Rubidium 87 D line data. *available online at http://steck.us/alkalidata*, revision 2.0.1,, May 2008.

[89] O. Svelto. *Principles of lasers / by Orazio Svelto ; translated by David C. Hanna.* Plenum Press, New York :, 1976.

[90] S. Swain. An exact solution of the multiatom, multimode model hamiltonian of quantum optics. *Journal of Physics A: General Physics*, 5(1):L3, 1972.

[91] T. Petelski, M. Fattori, G. Lamporesi, J. Stuhler, and G.M. Tino. Doppler-free spectroscopy using magnetically induced dichroism of atomic vapor: a new scheme for laser frequency locking. *Eur. Phys. J. D*, 22(2):279–283, 2003.

[92] M. Tavis and F. W. Cummings. Exact solution for an n-molecule—radiation-field hamiltonian. *Phys. Rev.*, 170(2):379–384, Jun 1968.

[93] R. J. Thompson, G. Rempe, and H. J. Kimble. Observation of normal-mode splitting for an atom in an optical cavity. *Phys. Rev. Lett.*, 68:1132–1135, Feb 1992.

[94] H. Tsuchida. Simple technique for improving the resolution of the delayed self-heterodyne method. *Opt. Lett.*, 15(11):640–642, Jun 1990.

[95] A. K. Tuchman, R. Long, G. Vrijsen, J. Boudet, J. Lee, and M. A. Kasevich. Normal-mode splitting with large collective cooperativity. *Phys. Rev. A*, 74(5):053821, Nov 2006.

[96] Q. A. Turchette, C. J. Hood, W. Lange, H. Mabuchi, and H. J. Kimble. Measurement of conditional phase shifts for quantum logic. *Phys. Rev. Lett.*, 75:4710–4713, Dec 1995.

[97] L. Turner, K. Weber, C. Hawthorn, and R. Scholten. Frequency noise characterisation of narrow linewidth diode lasers. *Optics Communications*, 201(46):391 – 397, 2002.

[98] S. J. van Enk, J. I. Cirac, and P. Zoller. Purifying two-bit quantum gates and joint measurements in cavity QED. *Phys. Rev. Lett.*, 79:5178–5181, Dec 1997.

[99] J. Vaughan. *The Fabry-Perot interferometer: history, theory, practice, and applications*. The Adam Hilger series on optics and optoelectronics. A. Hilger, 1989.

[100] V. Vuletić, H. W. Chan, and A. T. Black. Three-dimensional cavity doppler cooling and cavity sideband cooling by coherent scattering. *Phys. Rev. A*, 64:033405, Aug 2001.

[101] V. Vuletić and S. Chu. Laser cooling of atoms, ions, or molecules by coherent scattering. *Phys. Rev. Lett.*, 84:3787–3790, Apr 2000.

[102] A. Wickenbrock, D. Cubero, N. A. A. Wahab, P. Phoonthong, and F. Renzoni. Current reversals in a rocking ratchet: The frequency domain. *Phys. Rev. E*, 84:021127, Aug 2011.

[103] A. Wickenbrock, P. C. Holz, N. A. A. Wahab, P. Phoonthong, D. Cubero, and F. Renzoni. Vibrational mechanics in an optical lattice: Controlling transport via potential renormalization. *Phys. Rev. Lett.*, 108:020603, Jan 2012.

[104] A. Wickenbrock, P. Phoonthong, and F. Renzoni. Collective strong coupling in a lossy optical cavity. *Journal of Modern Optics*, 58(15):1310–1316, 2011.

[105] X. Xue, H. Wei, and A. G. Kirk. Intensity-based modal decomposition of optical beams in terms of hermite–gaussian functions. *J. Opt. Soc. Am. A*, 17(6):1086–1091, Jun 2000.

[106] J. Ye, D. W. Vernooy, and H. J. Kimble. Trapping of single atoms in cavity qed. *Phys. Rev. Lett.*, 83(24):4987–4990, Dec 1999.

[107] T. Zaugg, P. Meystre, G. Lenz, and M. Wilkens. Theory of adiabatic cooling in cavities. *Phys. Rev. A*, 49:3011–3021, Apr 1994.

[108] P. Zhou, Z. L. Hu, and J. S. Peng. Effect of atomic coherence on the collapses and revivals in some generalized jaynes-cummings models. *Journal of Modern Optics*, 39(1):49–62, 1992.